In Rhythm with the Wind

Synchronized Wake Mixing in Wind Farms

van Vondelen, A.A.W.

DOI
10.4233/uuid:9387d996-b8d3-4fdb-a255-d0e27430f78a

Publication date
2026

Document Version
Final published version

Citation (APA)
van Vondelen, A. A. W. (2026). *In Rhythm with the Wind: Synchronized Wake Mixing in Wind Farms*. [Dissertation (TU Delft), Delft University of Technology]. https://doi.org/10.4233/uuid:9387d996-b8d3-4fdb-a255-d0e27430f78a

In Rhythm with the Wind:

Synchronized Wake Mixing in Wind Farms

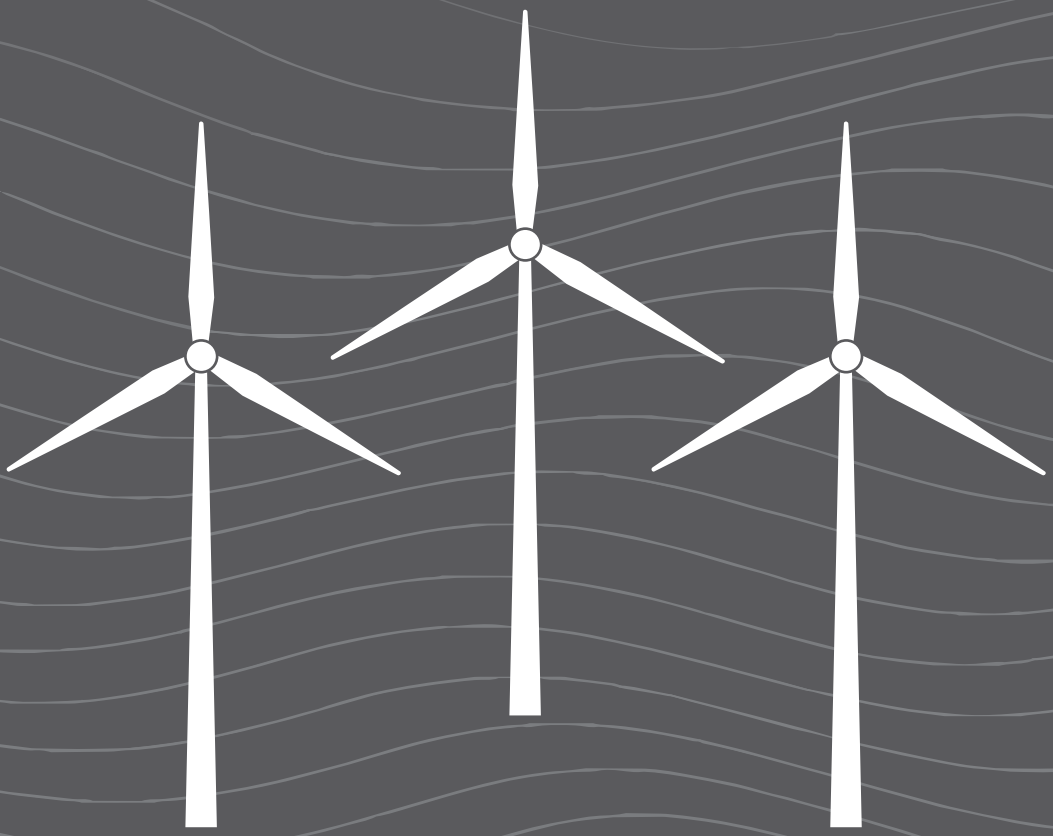

A.A.W. van Vondelen

In Rhythm with the Wind:

Synchronized Wake Mixing in Wind Farms

IN RHYTHM WITH THE WIND:

SYNCHRONIZED WAKE MIXING IN WIND FARMS

Proefschrift

ter verkrijging van de graad van doctor
aan de Technische Universiteit Delft,
op gezag van de Rector Magnificus prof. dr. ir. H. Bijl
voorzitter van het College voor Promoties,
in het openbaar te verdedigen op 28 januari 2026 om 17:30 uur

door

Aemilius Adrianus Wilhelmus VAN VONDELEN

Ingenieur in de systeem- en regeltechniek,
Technische Universiteit Delft, Nederland,
geboren te Zeist, Nederland.

Dit proefschrift is goedgekeurd door de promotoren.

Samenstelling promotiecommissie:

Rector Magnificus,	voorzitter
Prof. dr. ir. J.W. van Wingerden,	Technische Universiteit Delft, promotor
Dr. ir. S.P. Mulders,	Technische Universiteit Delft, copromotor
Onafhankelijke leden:	
Prof. dr. A.V. Metrikine,	Technische Universiteit Delft
Prof. Dr. -Ing. D. Schlipf,	Hochschule Flensburg, Duitsland
Dr. ir. M. Kok,	Technische Universiteit Delft
Dr. ir. D.-P. Molenaar,	Delft Offshore Turbine B.V.
Prof. dr. ir. B. De Schutter,	Technische Universiteit Delft, reservelid
Overige leden:	
Dr. ir. S.T. Navalkar,	Siemens Gamesa Renewable Energy B.V.

Dr. ir. S.T. Navalkar heeft in belangrijke mate aan de totstandkoming van het proefschrift bijgedragen.

Funding: This work is part of the Hollandse Kust Noord wind farm innovation program where CrossWind C.V., Shell, Eneco, Grow, and Siemens Gamesa are teaming up; funding for the PhDs was provided by CrossWind C.V. and Siemens Gamesa. SURF provided computational time on supercomputer Snellius (grant number: EINF-10024).

Keywords: synchronization, wind farm control, wind turbine, helix, phase estimation, Kalman filtering, wind tunnel, large-eddy simulation

Printed by: Ipskamp Printing

ISBN 978-94-6536-030-0

An electronic version of this dissertation is available at
`http://repository.tudelft.nl/`.

CONTENTS

SUMMARY

As the world moves toward a fossil-free future, offshore wind energy has become a major driver of the global energy transition. In particular, the Dutch North Sea, with its steady wind conditions and relatively shallow waters, offers ideal conditions for large-scale wind farm deployment. Yet, as turbines are placed close together to optimize space, new technical challenges arise. One of the most critical of these is *the wake effect*, where turbines operating upstream in the wind flow create turbulent, low-velocity wakes that significantly reduce the power production and increase the fatigue damage on downstream turbines.

This dissertation, titled “In Rhythm with the Wind: Synchronized Wake Mixing in Wind Farms”, addresses this challenge by exploring how dynamic, synchronized control strategies can mitigate wake-induced losses and improve overall wind farm performance. This work goes beyond the conventional approach of turbines operating independently and instead investigates how coordinated turbine control can create new opportunities.

A central theme throughout this dissertation is the use of *the Helix approach*, a dynamic control technique that employs periodic pitch actuation on turbine blades to create helical structures in their wakes. These structures promote faster mixing of the wake with surrounding, faster-moving air, accelerating wind speed recovery, and improving conditions for downstream turbines. Previous studies had demonstrated the potential of the Helix method in isolated scenarios, but its effectiveness in larger arrays and under turbulent, real-world conditions remained unproven.

This work begins by carefully examining the structural implications of applying the Helix method to full-scale turbines. Through simulations of the IEA-15MW offshore reference turbine, it is explored how varying the amplitude and frequency of pitch actuation influences structural loads and pitch bearing fatigue. The analysis reveals a clear trade-off: while stronger actuation can enhance wake mixing, it also increases fatigue damage, especially on pitch bearings, demonstrating the need for further optimization.

Building on this, the dissertation develops a novel output-feedback control architecture that enables downstream turbines to synchronize their own Helix actuation with the incoming wake generated by upstream turbines. Unlike previous methods relying on flow field assumptions, this strategy requires only local rotor-level sensing and allows for real-time, closed-loop synchronization. Importantly, it allows two distinct objectives: in-phase coordination to enhance power output, and “anti-phase" coordination to reject wake-induced structural loads. The ability to toggle between these modes offers a new degree of flexibility in wind farm operation.

While this method shows promising results, it only allows *in-phase* synchronization or load rejection, meaning that it could only increase or decrease the amplitude of the periodic content. The idea emerges that adjusting the alignment of the wakes by some optimal phase offset, through *out-of-phase* coordination, can create certain interference

mechanisms that could promote wake mixing even more. To accomplish this, a linear Kalman filter-based estimator is developed, capable of reconstructing the phase of wake-induced flow structures from local measurements. First tested in a wind tunnel with a three-turbine array, the method demonstrates that real-time phase estimation and out-of-phase coordinated Helix control can be accomplished experimentally. The results show tangible gains in downstream performance when turbines are optimally phase-aligned, confirming that out-of-phase synchronization improves the energy production of downstream turbines.

One major limitation of the Kalman filter-based method was that it used a linear model, which is only robust around a small operating range. As such, a new method is developed: an Extended Kalman filter with a dynamic Blade-element momentum model at its core, enabling robustness in the full nonlinear operating range of the turbine. This approach is then extensively validated in high-fidelity large-eddy simulations, which allow for detailed examination of how wake dynamics evolve under different synchronization settings. These simulations confirm that constructive interference between periodic wake structures, enforced through phase synchronization, can significantly enhance energy recovery downstream. Conversely, misaligned or unsynchronized actuation can negate these benefits or even degrade performance, stressing the importance of precise wake coordination.

The final part of the dissertation explores the flow physics behind these findings and reveals how the periodic structures in the synchronized wakes interact. These insights, combined with the development of several real-time estimation and control frameworks, establish a new subfield within wind farm flow control: *synchronization*. In this dissertation, this conceptual idea was brought from theory to a practical strategy for enhancing wind farm efficiency. By uniting system identification, model-based estimation, control theory, and both numerical and experimental validation, this dissertation provides a solid foundation for adopting synchronized wake mixing in future offshore wind farms. It supports a new vision for wind farms that operate not merely as individual machines, but as intelligent, coordinated flocks of birds — working in rhythm with the wind.

SAMENVATTING

Nu de wereld toewerkt naar een fossielvrije toekomst, is wind op zee een belangrijke aandrijver geworden van de wereldwijde energietransitie. Vooral de Nederlandse Noordzee, met stabiele windcondities en relatief ondiepe wateren, heeft ideale omstandigheden voor de grootschalige aanleg van windparken. Maar doordat turbines dicht op elkaar worden geplaatst om de beschikbare ruimte optimaal te benutten ontstaan er nieuwe technische uitdagingen. Een van de belangrijkste hiervan is het *wake-effect*: turbines die stroomopwaarts in de wind staan, creëren turbulente 'wakes' (zog, in het Nederlands) met lage windsnelheden, wat leidt tot verminderde energieopbrengst en verhoogde metaalmoeheid bij stroomafwaartse turbines.

Dit proefschrift, getiteld "In Ritme met de Wind: Gesynchroniseerd Zogmengen in Windparken", richt zich op deze uitdaging door te onderzoeken hoe dynamische, gesynchroniseerde regelstrategieën de negatieve effecten van het zog kunnen beperken en de algehele prestaties van windparken kunnen verbeteren. Deze studie gaat verder dan de conventionele aanpak waarbij turbines onafhankelijk opereren, en verkent hoe gecoördineerde turbine-aansturing nieuwe kansen kan creëren.

Een centraal thema in dit proefschrift is het gebruik van *de Helix-methode*, een dynamische regeltechniek waarbij periodieke pitch-actuatie op de turbinebladen wordt toegepast om spiraalvormige structuren in het zog te genereren. Deze structuren bevorderen een snellere menging van het zog met de omliggende, snellere lucht, wat de herstelsnelheid van het zog verhoogt en de omstandigheden voor stroomafwaartse turbines verbetert. Eerdere studies toonden al de potentie van de Helix-methode in enkelvoudige situaties aan, maar de effectiviteit ervan in grotere turbine configuraties en onder turbulente, realistische omstandigheden was nog niet eerder aangetoond.

Dit werk begint met een grondige analyse van de structurele implicaties van het toepassen van de Helix-methode op turbines van ware grootte. Via simulaties van de IEA-15MW referentieturbine wordt onderzocht hoe variaties in amplitude en frequentie van de pitch-actuatie de structurele belasting en vermoeiing van pitchlagers beïnvloeden. De analyse laat een duidelijke afweging zien: hoewel sterkere actuatie de zogmenging kan verbeteren, leidt dit ook tot hogere vermoeiingsschade, vooral op de pitchlagers, wat wijst op de noodzaak voor optimalisatie.

Vervolgens ontwikkelt dit proefschrift een nieuwe regelarchitectuur op basis van uitgangsgebaseerde gesloten-lus regeling, die het mogelijk maakt voor stroomafwaartse turbines om hun Helix-actuatie te synchroniseren met het inkomende zog van stroomopwaartse turbines. In tegenstelling tot eerdere methoden die gebaseerd zijn op aannames over het stromingsveld, maakt deze strategie uitsluitend gebruik van lokale metingen op rotorniveau en maakt ze real-time, gesloten-lus synchronisatie mogelijk. Belangrijk is dat er twee verschillende doelen nagestreefd kunnen worden: in-fase coördinatie om het energievermogen te verhogen, en "anti-fase" coördinatie om structurele

zog-belasting te onderdrukken. De mogelijkheid om tussen deze opties te schakelen biedt een nieuwe mate van flexibiliteit in windparkaansturing.

Hoewel deze methode veelbelovend is, beperkt ze zich tot *in-fase* synchronisatie of belastingreductie, wat betekent dat alleen de amplitude van de periodieke component vergroot of verkleind kan worden. Het idee ontstaat dat het afstemmen van wakes met een optimale faseverschuiving, via *faseverschoven* coördinatie, bepaalde interferentiemechanismen kan activeren die de zogmenging verder bevorderen. Om dit te realiseren wordt een lineaire Kalman-filter ontwikkelt, die de fase van stromingsstructuren veroorzaakt door het zog kan reconstrueren op basis van lokale metingen. Deze methode wordt eerst getest in een windtunnel met een opstelling van drie turbines. De resultaten tonen aan dat real-time fase-schatting en faseverschoven gesynchroniseerde Helix-aansturing experimenteel haalbaar zijn. Bovendien blijkt dat optimale fase-afstemming leidt tot een meetbare verbetering van de prestaties van stroomafwaartse turbines.

Een belangrijke beperking van de Kalman-filter gebaseerde methode is het gebruik van een lineair model, dat slechts robuust is binnen een beperkt werkingsgebied. Daarom wordt een nieuwe methode ontwikkeld: een extended Kalman-filter met een dynamisch blade-element momentum model als kern, die robuustheid biedt over het volledige niet-lineaire werkgebied van de turbine. Deze benadering wordt uitgebreid gevalideerd in hoge-resolutie large-eddy simulaties, waarmee nauwkeurig wordt onderzocht hoe zog-dynamiek zich ontwikkelt onder verschillende synchronisatie-instellingen. De simulaties bevestigen dat constructieve interferentie tussen periodieke zogstructuren, afgedwongen door fase-synchronisatie, de energieherwinning stroomafwaarts aanzienlijk kan verbeteren. Omgekeerd kan verkeerd afgestemde of onsynchrone actuatie deze voordelen tenietdoen of zelfs de prestaties verslechteren, wat het belang van nauwkeurige zog-coördinatie onderstreept.

Het laatste deel van het proefschrift onderzoekt de stromingsfysica achter deze bevindingen en laat zien hoe de periodieke structuren in gesynchroniseerde zoggen met elkaar reageren. Deze inzichten, gecombineerd met de ontwikkeling van meerdere real-time schattings- en regelkaders, vormen de basis voor een nieuw subveld binnen windparkregeling: *synchronisatie*. In dit proefschrift is dit conceptuele idee vertaald van theorie naar een praktische strategie om windparkefficiëntie te verbeteren. Door systeemidentificatie, modelgebaseerde schatting, regeltheorie, en zowel numerieke als experimentele validatie te combineren, biedt dit werk een solide basis voor de toepassing van gesynchroniseerde zog-menging in toekomstige windparken op zee. Het ondersteunt een nieuwe visie waarin windparken niet functioneren als losse machines, maar als intelligente, gecoördineerde zwermen vogels — in ritme met de wind.

ACKNOWLEDGEMENTS

People always seem a bit surprised when I tell them I am doing a PhD. Apparently, I am not what people imagine when they think of a typical scientist. And to be fair, when I was finishing my studies, doing a PhD was not something I wanted to do at all. In fact, it was firmly on the list of things I was absolutely not going to do. So what brought me here in the end?

Up until the final year of my MSc, studying had been a task that had to be completed, not something that I particularly enjoyed. This took a turn when I began my MSc thesis project with Siemens Gamesa, a wind turbine company. For the first time, I could apply theoretical knowledge to a real industry problem and make a direct impact. Thanks to an excellent supervisory team, I was able to thrive and share meaningful results every week. The lack of social distractions during COVID-19 probably helped too. It still came as a slight surprise when I received a short email from Jan-Willem after completing my literature studies:

> "Dear Mees, can you think whether you would find it interesting to do a PhD? JW."

And here I am, four years later, about to thank everyone who made this journey possible, starting with that email.

Jan-Willem, it has been an honor to be part of your team. You have been both a great mentor and a motivator. I enjoyed our scientific discussions just as much as the more informal moments at conferences. The academic freedom and autonomy you give your students is refreshing, sometimes challenging, but always valuable. It has pushed me to become more independent and more self-critical.

Sachin, I was very grateful that our collaboration could continue after my MSc thesis. I often brag about having you as a supervisor and co-author. Your eye for detail is unmatched. You spot the tiniest mistakes, especially in equations that most people take for granted. Thank you for your guidance, your patience, and your sharp insights over all these years.

Aside from Jan-Willem and Sachin, who have supervised me during the past four years and are part of my doctoral committee, I would also like to thank the other members of the committee. Sebastiaan Mulders, Andrei Metrikine, David Schlipf, Manon Kok, and David Molenaar, I am honored to have you as opponents at my defence. Thank you for taking the time to read, assess, and discuss my dissertation at the defence.

When I started my PhD four years ago, we were still in the small offices: four desks cramped into one room, shared with Daan, Marcus, and Daniel. Daan, many thanks for being my MSc supervisor and for writing so many papers together. Thanks also for helping me out in the Wind AI lab and the Open Jet Facility. I was lucky that you had already done the difficult preparation work in your earlier research, so that I could simply press

the button and start experimenting. Daniel and Marcus, thank you for being my office-mates in the first part of my PhD, for the interesting discussions we had over coffee, and for the many events we attended together.

Then there was the other room, which even had five desks, occupied by Atin, Amr, Maarten, Unai, and David. Amr, I still cannot get over attending your wedding in Rabat, Morocco. It was probably one of the most unforgettable experiences I have ever had, dancing until 07:30, no alcohol involved. Thank you for Disco Arabesquo in Paradiso and for sharing the best Syrian shawarma places. Atin, I never thought I would become colleagues with a former student from Institut Teknologi Bandung in Indonesia, where I had my exchange semester. Thanks for being an amazing co-author and my go-to control wizard of the group. Unai, thank you for many great moments teaching students how to build wind turbines and writing a paper together that applied theory from my MSc thesis. Thanks also to Maarten, always a tricky foosball opponent, and to David, who I hope will always remember to put sunscreen *also* in the Netherlands after our fun boat trip.

Some of us were scattered in mixed offices along the hallway. Rogier, we started almost at the same time. I remember an online meeting when we were still MSc students in the group, where you kept asking questions. I will admit that I was getting a little impatient with you because I just wanted the meeting to end. It turns out you were not so bad after all. From the Atlas Mountains in Morocco to yakiniku in Japan to hiking the 150-kilometer West Highland Way in Scotland right before a conference (still recovering from the midges and the blisters), we have had some unforgettable trips.

Livia, thank you for your endless enthusiasm and for being a too strong competitor for the best paper awards. Sebas, for the academic discussions and the fun moments teaching the control BSc course. Emanuel and Jonas, my go-to fluids experts, for teaching me about LES and for sharing the highs and lows of the Hollandse Kust Noord project.

I also want to acknowledge the other groups at DCSC, but especially those who stubbornly played foosball every day after lunch. Coen, Sander, Jacques, Roger, Max, and Pascal, thank you for all the games when the foosball table was still next to the bathroom. The acoustics were much better when someone scored a *klinker*. Those daily matches were small moments (although sometimes they could extend well into the afternoon), but they made work much more enjoyable.

A new phase started when we had to relocate our office to the *Kraaiennest*. It was quite a gloomy period for our group, literally, because there was no direct daylight in those rooms, and there were manufacturing machines operating continuously around us. What was supposed to be a temporary three-month relocation due to office renovation stretched into six months during the winter.

Upon returning to DCSC after the renovation, we were welcomed with shiny state-of-the-art sit-stand desks and colorful meeting rooms. This new office environment was a significant improvement, and with this new phase, new colleagues arrived. Marion, I remember being really impressed by the quality of your first presentation. I am sorry that I scared you a bit at first, but I am glad we became friends and that I could learn so many things from you. Thank you for being an amazing co-author and for all the travels we made together, and of course, for the legendary gasoline drink, thank you, Felix.

Guido, thank you for sharing your southern Italian hospitality and for teaching me

about Italy and Naples. I still stand by my opinion about butter in Amatriciana. Matteo, thank you for the travels and the parties. Your work-hard-play-hard approach was inspiring to be around for all of us. Tim, thank you for all the unforgettable moments, like at Macadam and Sissi's. Thanks also to the other foosball legends, Sam, Salim, and thanks to the new people in the data-driven control group, Robin, Alexandra, Sachin, Leendert, Tristan, Faegheh, and Fritz.

The Hollandse Kust Noord project started with a great group of talented people from Siemens Gamesa, Eneco, Shell, CrossWind, GROW, and TU Delft. Even though many members changed over time, the project continued at a steady and productive pace. From Siemens Gamesa, I want to thank David, Pieter, Juanjo, Mauk, Hendri, Thomas, and Juliette. Also, special thanks to Alex, my former MSc supervisor. From Eneco, René and Maarten. From Shell, Jasper, and Bart. From CrossWind, Maria. From GROW, Anouk and David. And from TU Delft, Dunja, Remco, and Maxim.

Thank you for the excellent discussions and for allowing me to learn from industry leaders. I will never forget the enthusiasm and competitive spirit I saw in this group during the escape room we did for our social event. Thank you also to Joeri and Paul from NREL for their involvement in the project.

Throughout my PhD, I was lucky to have supervised four excellent MSc students. Daan, Joris, Sjors, and David, thank you for your dedication and your enthusiasm for this field of research. The MSc projects always felt like a collaboration where we learned a lot from each other. Aside from superb theses, we were able to produce several excellent papers and a patent.

From the DCSC staff, thanks go out to all, but specifically to Will and Ralph for assisting with the experiments. Special thanks go to Wim for his enormous commitment to the project. I lost count of how many times you assembled and disassembled those nasty MoWiTo model turbines and somehow always managed to get them working again. Thank you for making sure the experiments could continue and for hosting me for many long hours in the lab.

These four years were made much easier thanks to my friends, especially from Triple Z, Mortier, and my former housemates, whose puzzled faces I will never forget when trying to explain my activities at TU Delft. Aside from the usual jokes, they showed real interest in my work and were usually quite jealous of my conference travels. Thank you for allowing me to sharpen my elevator pitch about my project, which usually involved a few beer bottles representing wind turbines. Explaining a complex topic with simple words is never easy, and those moments helped me realize how important that skill is.

Finally, I want to thank the people who have been there long before my PhD started. My parents, Hanny and Boudewijn, who supported me from the beginning to the end and always trusted me to make the right decisions. And my sisters and their partners, Ella, Alex, Britt, Julian, and my grandfather Wim, for their support. Everyone in our family does something completely different, which sometimes makes it difficult to understand what everyone is doing. However, it is refreshing to see such variety. It reminds me that there are many ways to live your life. Thank you for giving me the freedom to choose my own path.

Mees van Vondelen
Amsterdam, September 2025

PREFACE

The Netherlands has a long-standing relationship with wind. For centuries, it was leveraged to mill grain and reclaim land; even today, though long retired, these iconic windmills continue to attract large numbers of visitors, still admired as symbols of Dutch ingenuity. The modern age brought offshore wind turbines, just visible from the coast on a clear day, that provide electricity for millions of Dutch households. Wind energy is an integral part of the Dutch identity, and now, as the world faces escalating challenges, the Netherlands once again embraces wind. This preface walks through historical, industrial, and political developments, providing context for the work presented in this dissertation.

A BRIEF HISTORICAL NOTE ON DUTCH WIND ENERGY

Already in the 13th century, windmills played an important role in the Netherlands (de Kraker 2020). Initially, primarily for water management, wetlands were drained for agriculture, and low-lying areas were shaped into canals and rivers. Later, by the 19th century, windmills reached the peak of their technological development and were used for many different industrial applications, ranging from sawmills used in shipbuilding (Fig. 1) to tobacco mills, spice mills, and the list goes on. However, the discovery of the steam engine and the rise of fossil fuels led to a sharp decline in wind energy utilization, initiating the Industrial Revolution. Although that period brought immense economic growth and technological advancements, the negative effects of fossil fuels resulted in one of the world's major challenges in this era: climate change (IPCC 2021).

Figure 1: Houtzaagmolen De Rat in IJlst, Friesland, a functioning example of a traditional Dutch wind-powered sawmill. Built in the 17th century and reconstructed in the 19th century, it showcases the industrial applications of wind energy before the fossil fuel era (Friesland.nl 2025).

THE FOSSIL FUEL ERA AND THE GRONINGEN GAS FIELD

The discovery of the Groningen gas field in 1959 transformed the Dutch energy landscape. As one of the world's largest natural gas reserves, it provided a reliable and inexpensive domestic energy source, and helped shape a nationwide infrastructure centered around natural gas. At its peak, Groningen supplied over 80% of Dutch households. But its long-term consequences became increasingly apparent: decades of gas extraction led to increasing seismic activity, damaging homes and public trust. After years of struggle, the Dutch government committed to phasing out production entirely by 2024 (Ministerie van Economische Zaken en Klimaat 2023).

While this political decision mitigated seismic risks and restored some of the public trust, the closure of the field brought a new reality to the energy landscape in the Netherlands. Suddenly, the country is vulnerable to market volatility and dependent on other countries for a significant part of its energy supply. Recent geopolitical shocks, as seen during the 2022 energy crisis caused by the war in Ukraine, emphasized the need to not only decarbonize but also become energy-independent.

The revival of wind energy and its challenges

Interest in wind energy regained after the oil crisis in the 1970s (Gipe 1995). Poul la Cour's experimental work in the late 19th century is often regarded as the foundation of modern wind power (la Cour 1900), but Denmark's policy-driven innovation in the 1970s and 80s, led by engineers like Henrik Stiesdal, pioneered the commercial technologies (Stiesdal 2020) that define the global wind energy sector today.

Now, after increasing global recognition of the detrimental effects of fossil fuels, formalized by agreements such as Paris (UNFCCC 2015), wind energy serves as one of the largest drivers towards a renewable society. The Netherlands aims to install 21 GW of offshore wind capacity by 2030, enough to supply the majority of domestic electricity demand (Rijksoverheid 2022). Turbines are rapidly growing in size and number, and offshore wind zones are expanding further into the North Sea.

Yet this transformation comes with spatial, technical, and financial challenges. The North Sea is a shared and increasingly congested space, home to shipping lanes, fisheries, military zones, and protected wildlife. As a result, the available area for offshore wind is limited, forcing planners and operators to optimize energy density within existing zones (REN21 2023).

At the same time, the business case for offshore wind is under pressure. While turbine technology has improved and costs have fallen in past decades, allowing the first subsidy-free farms to be commissioned (Durakovic 2022), current market conditions, rising material costs, inflation, and interest rates have led to project delays and cancellations (McKinsey & Company 2024; Reuters 2025b). Several major offshore developers across Europe have reported financing difficulties (Rystad Energy 2023), emphasizing the need for not only technological innovation but also economic efficiency in how wind farms are operated.

Grid and system-Level challenges

The Netherlands also faces critical system-level challenges to scaling renewable energy. Grid congestion has emerged as a major bottleneck due to the sudden electrification of many systems and new buildings. In several provinces, solar and wind projects cannot even be connected due to limited transmission capacity (Regulatory Assistance Project 2024). Despite massive planned investments by TenneT (€200 billion by 2034) (Reuters 2025a), resolving these issues will take time.

Other challenges became apparent during the large-scale power outage across the Iberian Peninsula in April 2025. Though investigations are still ongoing, the event sparked renewed focus on grid resilience, particularly in systems with a high share of

renewable sources (Reuters 2025c). These challenges make clear that a reliable energy transition will require not just new infrastructure, but also smarter operation of existing assets.

FROM WINDMILLS TO WAKE MIXING

As this work returns from the societal and historical challenges to the present moment, it focuses on one particular part of the energy transition: the quest to make wind farms more efficient, more intelligent, and more coordinated.

While the challenges of today differ significantly from those of the 13th century, the essence of innovation remains the same. From sawmills powered by wooden sails to offshore wind farms operated by control algorithms, the underlying question persists: how can we harness the wind more effectively? This dissertation explores a new technology to achieve this: synchronized wake mixing control.

1

INTRODUCTION

This chapter introduces synchronized wake mixing as a novel wind farm control strategy to improve power output and reduce loading by aligning periodic wake structures across turbines. While wake mixing methods like the Helix approach have shown promise, their application has been limited to isolated, open-loop setups. Inspired by natural synchronization phenomena, this dissertation proposes a closed-loop control framework based on real-time wake phase estimation. The chapter reviews existing strategies, identifies key research gaps in estimation and coordination, and outlines the dissertation's goal: to enable effective synchronized wake mixing in multi-turbine arrays through integrated estimation, control, and experimental validation.

1

Contents

1.1. CHALLENGES IN WIND ENERGY

Wind energy is one of the cleanest and most sustainable sources of power available today. Already after seven months, a wind turbine's production breaks even with the energy that it required for its manufacturing, transport, installation, and eventual decommissioning (Guezuraga, Zauner, and Pölz 2012). After that, around 20 more years of emission-free electricity follow, sometimes even longer, depending on the turbine's fatigue life (Hau 2013).

Next to being clean, wind energy is also highly scalable through wind farms. Wind farms offshore are growing rapidly thanks to steady wind conditions and shallow waters, for example, in the North Sea (European Commission 2023). Grouping turbines allows for shared infrastructure, such as foundations, cables, and maintenance vessels, which significantly reduces the levelized cost of energy (LCoE) (International Energy Agency 2023). Offshore locations also avoid many of the common objections raised near residential areas, such as noise pollution, shadow flicker, or visual impact (Firestone, Kempton, and Krueger 2012).

However, the availability of suitable offshore sites is decreasing. Many of the most favorable locations have already been developed, and new sites often involve greater technical and logistical challenges (International Energy Agency 2023). This pushes developers to do more with less space. The common approach is to increase the energy density of a wind farm, which has led to the rapid scaling of turbine sizes in recent years. Larger turbines generate more power due to their increased swept area and reduce the number of units needed, further lowering costs (Ashuri, Zaaijer, and van Bussel 2014).

Still, the trend toward larger turbines is reaching its limits. The wind industry has recently faced significant challenges with turbine models becoming obsolete after only a few installations, rising inflation, and COVID-related disruptions (Staff 2024). Entire supply chains had to adapt to each new turbine generation, including the construction of new factories and even larger installation vessels. In some cases, vessels ordered for the current generation of turbines were too small by the time they were delivered. As a result, the industry is now turning its attention away from size alone and toward other innovations that can drive down LCoE (NedZero 2024).

A major opportunity for technological innovation may lie in optimizing the aerodynamic interaction between turbines (Meyers, C. Bottasso, *et al.* 2022). As each turbine extracts energy from the wind, it leaves behind a slow and turbulent wake. Downstream turbines operating in this wake experience reduced wind speed and increased turbulence, leading to lower power output and higher fatigue loading (Meyers and Meneveau 2012; R. J. Stevens and Meneveau 2017). Even with layout optimization, these situations occur relatively often under real-world wind conditions. Depending on the site, wake-induced power losses of 10–20% are not uncommon (Barthelmie *et al.* 2009). Optimizing wind farms to recover this 'lost' energy is therefore one of the major topics in current wind energy research Meyers, C. Bottasso, *et al.* 2022, and the aerial photograph of Vattenfall's Horns Rev 1 offshore wind farm has become iconic in this field. This picture captures this phenomenon, usually not visible to the naked eye, where certain atmospheric conditions made it possible to observe it (Fig. 1.1).

In this image, wind turbines are controlled to maximize their own local power output, without accounting for the effects on other turbines in the farm. This leads to suboptimal

Figure 1.1: Aerial photograph of the Horns Rev 1 offshore wind farm showing turbine wake effects made visible by condensation in humid, stable atmospheric conditions. The image clearly illustrates the persistence of turbine wakes. Photo credit: Christian Steiness / Vattenfall.

performance at the farm level, but it is how traditional wind farm operation works. Over the past decade, the concept of *wind farm control* (WFC) has emerged to address this issue by coordinating turbine behavior to optimize farm-wide objectives such as total power output or structural load reduction, which implies that some turbines operate suboptimally to benefit the farm (Knudsen, Bak, and Svenstrup 2015).

Several WFC strategies have been developed, which can roughly be subdivided into the following categories:

- **Wake steering via yaw control**, where upstream turbines are intentionally misaligned to deflect their wakes away from downstream turbines (e.g., Gebraad *et al.* 2016).
- **Axial induction control**, where upstream turbines are derated to allow higher wind speed to pass through to downstream machines (e.g., Annoni, Fleming, *et al.* 2018).
- **Wake mixing control**, where dynamic actuation, typically via blade pitch, is used to introduce periodic structures in the wake that promote faster mixing with the surrounding flow (e.g., Frederik, Doekemeijer, *et al.* 2020; Munters and Meyers 2018a).

While these strategies have shown potential in simulation and field experiments, several challenges remain before they can be broadly applied in commercial wind farms (although wake steering has seen its first commercial applications, e.g., Siemens Gamesa

2019). Many current turbines were not designed for such coordinated or dynamic control, and increased imbalanced and unsteady loading remains a concern. Furthermore, most dynamic control approaches are applied in open loop or assume perfect wake overlap. Without real-time coordination, dynamic wake control may yield inconsistent or even counterproductive results.

Recent research suggests that applying dynamic control strategies such as wake mixing in a coordinated fashion across multiple turbines may amplify beneficial flow interactions (Korb, Asmuth, and Ivanell 2023). Synchronization allows for constructive interference of wake-induced structures, leading to improved wake recovery and downstream performance. However, this approach requires real-time estimation of wake phase and control coordination, which are both challenging in turbulent, time-varying flow environments.

Ultimately, improving wind farm efficiency through advanced control strategies not only reduces energy costs, but also increases the reliability and flexibility of wind power as additional control handles allow better balancing of power production with demand. This is especially relevant as wind takes on a larger share of grid responsibility in our future decarbonized energy system (Veers *et al.* 2019).

This dissertation addresses a central challenge in wind farm control: how to dynamically and intelligently synchronize turbine control actions to manipulate wake flows for improved power output and reduced loading across the farm.

1.2. CONTROL IN WIND ENERGY

This section reviews the technical background underlying these challenges, beginning at the individual turbine level and progressing toward coordinated farm-wide control.

1.2.1. TURBINE-LEVEL CONTROL

A modern three-bladed wind turbine is a nonlinear dynamical system, controlled to extract energy from varying wind conditions while maintaining structural integrity. Its operation is typically divided into four control regions, based on wind speed, which is schematically displayed in Fig. 1.2 and described below:

- **Region 1 (cut-in)**: At very low wind speeds, the turbine is not generating power. The blades are often feathered (pitched out of the wind) or held in a stalled state to avoid rotation.

- **Region 2 (variable power)**: As wind speeds increase beyond the cut-in threshold (typically around 3–4 m/s), the blades are pitched into the wind. In this region, the turbine operates below rated power and uses torque control to maintain optimal tip-speed ratio, maximizing aerodynamic efficiency. This is known as the greedy control regime, as it seeks to locally maximize power capture. The theoretical upper bound of energy extraction is the Betz limit, which states that no more than 59.3% of the kinetic energy in the wind can be converted to mechanical energy. Modern turbines typically achieve 40–50% efficiency in practice (Hau 2013).

- **Region 3 (constant power)**: At higher wind speeds, approaching rated conditions (typically 11–15 m/s), the aerodynamic torque can exceed the rated capacity of the generator and drivetrain. To limit mechanical stress, collective blade pitch is used to reduce aerodynamic loading and regulate power output. The pitch controller ensures constant power (or torque) is delivered while keeping structural loads within safe limits.
- **Region 4 (cut-out)**: If wind speed exceeds a shutdown threshold (e.g., 25 m/s), the turbine is stopped entirely to avoid damage.

This control strategy effectively maximizes the energy yield of an individual turbine. However, it does so in isolation, neglecting aerodynamic interactions between turbines in a wind farm. In a farm setting, this greedy control leads to wake interactions, which reduce downstream performance and increase fatigue loading.

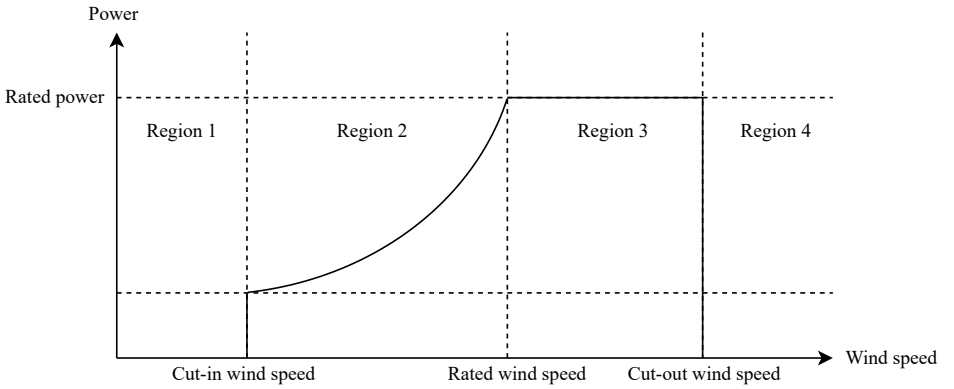

Figure 1.2: Schematic of conventional turbine-level control regimes.

1.2.2. WIND FARM CONTROL

Wind farm control seeks to overcome the limitations of individual turbine control by coordinating the behavior of multiple turbines to optimize farm-level performance. In this framework, individual turbines may operate suboptimally to improve overall energy capture, reduce structural loading, or meet grid-level power demands. Objectives can include maximizing total power production, minimizing the LCoE, or distributing fatigue loads more evenly across the farm (Knudsen, Bak, and Svenstrup 2015).

Several control strategies have been proposed, each manipulating different aspects of turbine behavior to alter wake characteristics and flow recovery.

WAKE STEERING

Wake steering is one of the most established and widely studied wind farm control strategies (see Fig. 1.3b for a schematic representation). The approach purposefully introduces a yaw misalignment in upstream turbines to laterally deflect their wakes away

from downstream turbines. Since the wake deficit region is concentrated along the rotor axis, even moderate yaw angles (e.g., 20–30°) can steer the wake by one or more rotor diameters at typical turbine spacings (Gebraad *et al.* 2016; Jiménez, Crespo, and Migoya 2010).

When a rotor is misaligned with the incoming flow, the inflow velocity varies across the rotor disk. This results in an asymmetric distribution of bound vorticity on the blades, which in turn leads to asymmetric shedding of vorticity into the wake. The resulting vorticity imbalance is the primary mechanism behind the observed wake deflection and unsteady aerodynamic effects. This results in a skewed wake that can bypass downstream rotors, improving their inflow velocity and thereby power output.

Wake steering has been validated in several settings:

- **Numerical**: Large-eddy simulations (LES) studies show farm-wide power gains of up to 10–15% under aligned wind conditions (Fleming, Gebraad, *et al.* 2014; Gebraad *et al.* 2016).
- **Experimental**: Wind tunnel tests confirm the wake deflection trends and support model validation (Bastankhah and Porté-Agel 2016).
- **Field measurements**: Several campaigns demonstrated power gains and successful closed-loop yaw control (Doekemeijer, Kern, *et al.* 2021; Fleming, King, *et al.* 2019; Howland, Lele, and Dabiri 2022).

However, wake steering has several practical limitations:

- The yaw actuator bandwidth is slow (order of tens of seconds), limiting responsiveness to fast-changing wind conditions.
- Yaw misalignment reduces the power output of the upstream turbine and introduces asymmetrical loads.
- Optimal yaw setpoints depend on ambient conditions, which are often uncertain.

Advanced strategies now combine data-driven surrogate models (e.g., FLORIS) with optimization algorithms to compute optimal yaw angles in real time (Annoni, Fleming, *et al.* 2018; Doekemeijer, Hoek, and Wingerden 2019). Further investigations are also done in the joint optimization of wind farm layouts with wake steering control to further improve farm-level performance (Baricchio, Gebraad, and van Wingerden 2024; Stanley, Bay, and Fleming 2023).

AXIAL INDUCTION CONTROL

Axial induction control (AIC) aims to manipulate the thrust force of an upstream turbine to reduce the velocity deficit in its wake. In contrast to wake steering, AIC operates along the axial (streamwise) direction by adjusting how much energy the turbine extracts from the wind.

The main idea is that by derating the upstream turbine (i.e., reducing torque or pitch to operate below the rated power production), more kinetic energy is preserved in the flow,

which can benefit downstream turbines (Annoni, Gebraad, *et al.* 2016; Marden, Ruben, and Pao 2013).

AIC works as follows: it applies a constant thrust coefficient (or torque setpoint) below the greedy optimum. It is straightforward to implement but results in a steady loss of upstream power and limited wake recovery. Van der Hoek, Kanev, *et al.* 2019 have not been able to demonstrate robust power increases in an experimental setting. Nevertheless, the method may prove useful for farm-level load balancing.

WAKE MIXING CONTROL

Wake mixing control refers to a class of dynamic control strategies designed to enhance turbulent entrainment and mixing in the wake of a turbine.

A dynamic variation of AIC is called Dynamic AIC or DIC, which periodically manipulates thrust, e.g., using sinusoidal pitch variation, at a frequency that excites wake instabilities (see Fig. 1.3c for a schematic representation). This promotes enhanced wake mixing and faster recovery (Munters and Meyers 2018a). DIC has been shown in LES to trigger large-scale coherent structures in the wake (e.g., vortex shedding or pulsation modes), improving recovery by entraining higher-momentum freestream air. Later experimental studies indeed confirm the method improves wake recovery (Frederik, Weber, *et al.* 2020; van der Hoek, Frederik, *et al.* 2022). Although promising in simulations and wind tunnel experiments, DIC has yet to be widely demonstrated in the field due to concerns about actuator capability, grid fluctuations, and load impacts.

While DIC is one example, more recent efforts focus on exploiting specific wake modes through periodic excitation. A prominent method in this domain is the Helix approach (Frederik, Doekemeijer, *et al.* 2020), which uses dynamic pitch control to impose a helical velocity mode on the wake (see Fig. 1.3d for a schematic representation). The result is a periodic, corkscrew-like wake that rapidly entrains ambient air and recovers momentum more quickly.

The benefits of wake mixing control include:

- Implementation via existing turbine actuators (e.g., collective or individual pitch).
- No need for yaw misalignment or permanent power derating.
- Creation of controllable wake dynamics.

However, some technical challenges include:

- Requirement for high-bandwidth pitch actuation, impacting fatigue life, especially the pitch bearing (Chapter 2 in this dissertation).
- Most effective during full wake overlap, which requires supervisory control and toggling between different WFC methods like wake steering (Taschner, Becker, *et al.* 2024).
- No formal farm-level implementation available yet, currently limited to only the upstream row of wind turbines.

The final point of these technical challenges is the main topic of this dissertation, where the concept of *synchronization* is studied. In this idea, the wakes of up- and downstream turbines align to exploit certain interference mechanisms, thereby promoting wake mixing further downstream: the next step towards farm-level implementation of wake mixing methods.

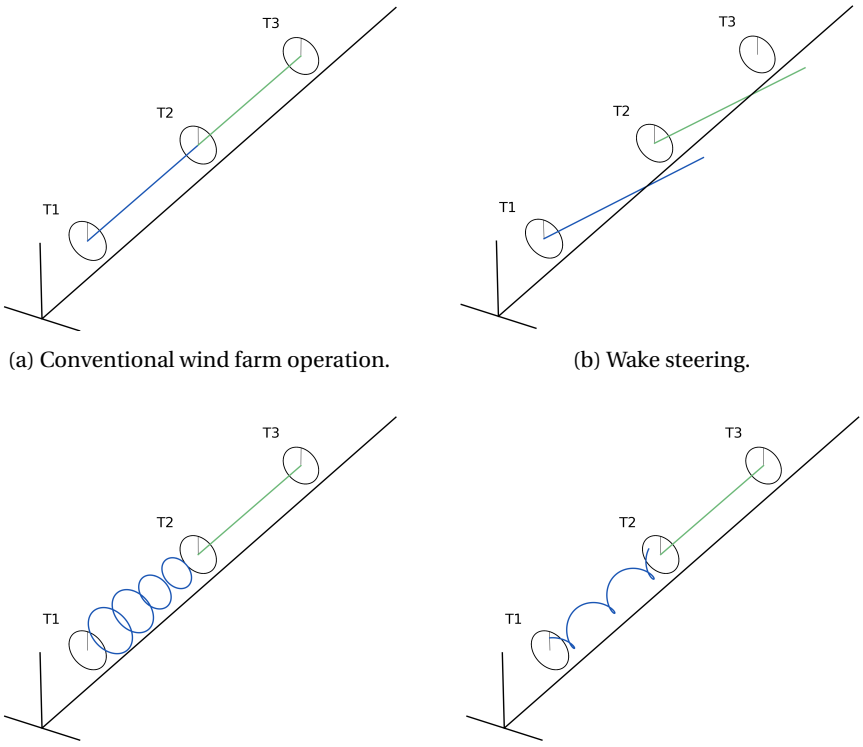

(a) Conventional wind farm operation.

(b) Wake steering.

(c) Dynamic induction on T1.

(d) Helix on T1.

Figure 1.3: Schematic representations of different wind farm control methods.

1.3. RESEARCH GAP IN WAKE MIXING CONTROL

While wake mixing control strategies such as dynamic induction and Helix control have demonstrated promising results in simulations and controlled experiments, most studies have been limited to simple configurations, often involving only one or two turbines (see Fig. 1.4 for an example of such a setup) (Frederik, Doekemeijer, *et al.* 2020; Taschner, van Vondelen, *et al.* 2023; van der Hoek, Frederik, *et al.* 2022; van der Hoek, Van den Abbeele, *et al.* 2024). In these simplified setups, dynamic actuation is applied in an open-loop manner with a fixed phase and frequency, assuming idealized and repeatable wake behavior. However, when implementing wake mixing methods in larger wind farms operating under realistic and turbulent flow conditions, the effectiveness of these control

strategies becomes more uncertain as the periodic wakes interact and influence their respective wake dynamics.

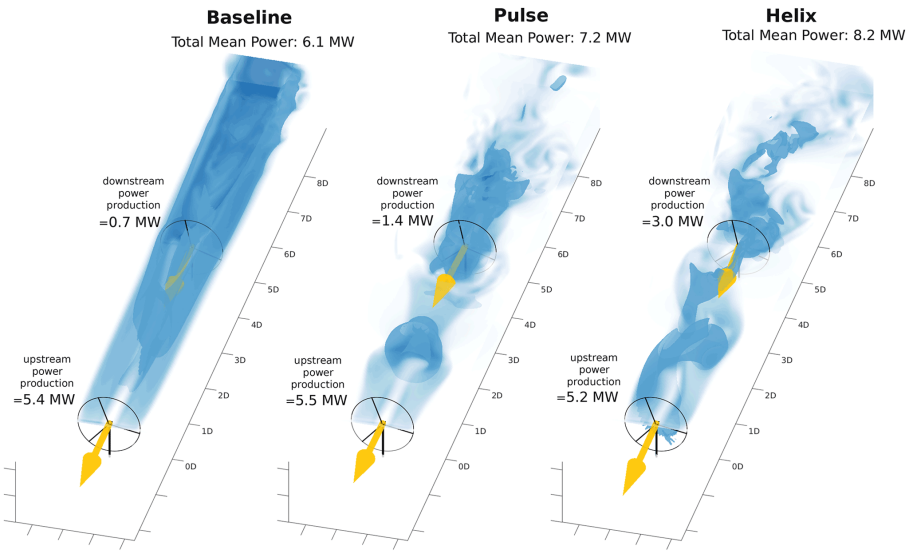

Figure 1.4: LES visualization of turbine wakes in simple two-turbine setups under different control strategies, adapted from Meyers, C. Bottasso, *et al.* 2022. Left: baseline operation; middle: periodic dynamic induction control Munters and Meyers 2018b; right: helix approach Frederik, Doekemeijer, *et al.* 2020. Dark blue shows a velocity isosurface; light blue indicates velocity magnitude in the horizontal plane.

Korb, Asmuth, and Ivanell 2023 showed that the coordination of up- and downstream Helix wakes has a strong effect on performance, where certain alignments even negate the positive effects of a single Helix wake, while others can further enhance the farm-wide power production. However, they study the concept from a controlled environment, while initiating the Helix at different time instances and comparing the results, and do not propose a robust synchronization method.

Specifically, there is a lack of estimation and control frameworks capable of reconstructing the phase of wake-induced flow structures from local measurements at downstream turbines. Without such estimators, synchronized control remains infeasible in practical wind farms. Moreover, while dynamic wake mixing has been shown to improve downstream flow recovery, its impact on and possible management of structural loading, particularly under synchronized operation, remains underexplored.

In summary, the current body of literature lacks:

- Real-time estimators capable of phase reconstruction from local turbine data.
- Closed-loop control strategies that adapt dynamically to wake evolution and turbine interactions.

- Quantitative assessments of load implications of the Helix approach, both with and without synchronized actuation.
- Experimental demonstrations of synchronized wake mixing control in multi-turbine arrays.

Addressing these gaps is essential to achieve the full potential of wake mixing in a full wind farm and to enable its application in real-world wind farms.

1.4. THE IDEA OF SYNCHRONIZATION

Synchronization is not a new concept; nature has practiced it for millions of years. Birds, in particular, are perhaps the most well-known coordinators of optimized aerodynamic flow. Their organized formation is not a matter of coincidence, in fact, flying in close proximity serves an important aerodynamic purpose. Studies on northern bald ibises revealed that the trailing bird, when flying in V-formation, flaps nearly in phase with the leader to remain in regions of induced upwash (see Figure 1.5), benefiting from reduced aerodynamic drag. However, when a bird flies directly behind another in line, it tends to flap in anti-phase, avoiding the energetic cost of downwash from the leader's wingtip vortices (Portugal *et al.* 2014).

Wake mixing control techniques generate periodic wake structures that enhance entrainment and flow recovery. When applied to multiple turbines in an array, these periodic wake motions can interact in complex ways. The concept of synchronization refers to the deliberate coordination of such wake-induced motions between turbines, aligning the phase of actuation on the downstream turbine with the phase of incoming flow structures, just as birds do when flying in formation.

Thus, we take inspiration from these natural synchronization phenomena in this work. Rather than applying periodic control signals independently at each turbine, synchronization aims to phase-align downstream actuation with the upstream-induced wake dynamics. This phase alignment can lead to dynamic wake interactions, in which the periodic structures from different turbines either reinforce or alter each other in certain ways.

Figure 1.6 illustrates three scenarios. The first is the baseline scenario, currently industry practice, with no active wake control. The second is the Helix scenario, primarily studied with only the upstream turbine activated. The third is the proposed scenario, where the Helix is implemented on both the up- and downstream turbines, potentially enhancing performance for turbines further downstream.

In the scenario where T1 and T2 both employ the Helix, two distinct scenarios can be found, where, depending on the alignment, constructive or destructive interference between the two wakes may be created, analogous to how birds adjust their relative flapping phase depending on whether they fly in V-formation or directly behind one another. This is illustrated in Fig. 1.7.

Implementing synchronization in practice and creating either constructive or destructive interference requires real-time knowledge of the incoming wake phase at downstream turbines. This dissertation presents a framework for estimating this phase from local turbine measurements and adapting actuation accordingly. The overarching goal

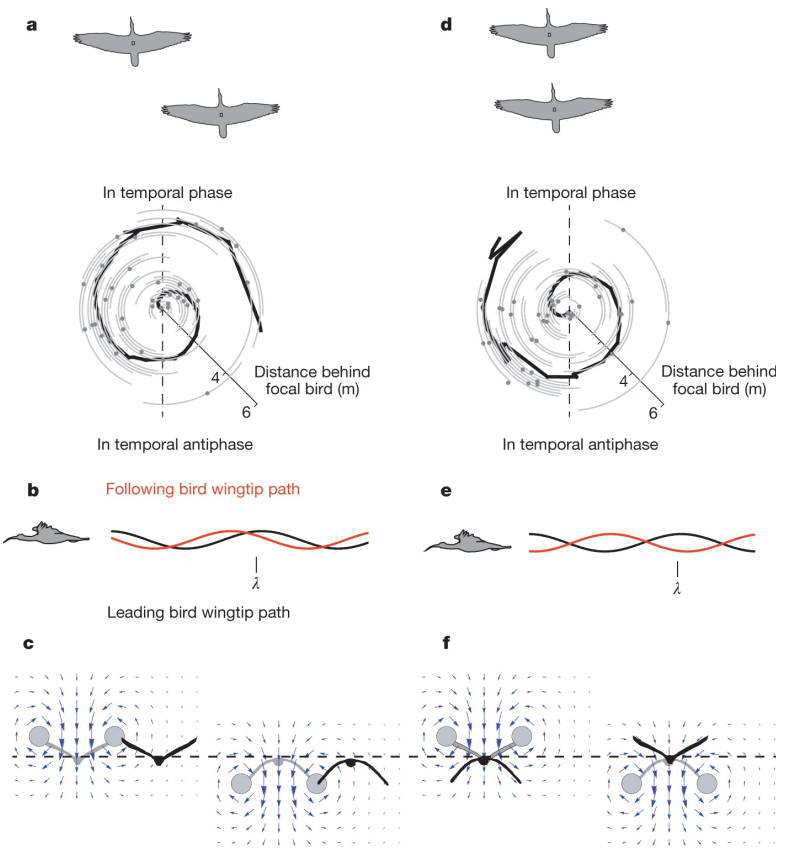

Figure 1.5: Observed phase relationships between birds in formation flight. Trailing ibises flap in phase with the leader when flying in V-formation and in anti-phase when flying directly behind. Adapted with permission from Portugal et al. (2014), *Nature*, © Springer Nature Limited.

is to move from isolated, open-loop wake control toward coordinated, dynamic control strategies that account for wake interactions.

Synchronization, therefore, enables scaling wake mixing control to multi-turbine and full wind farm configurations, opening a path toward more integrated wind farm flow control strategies.

1.5. DISSERTATION GOAL AND RESEARCH OBJECTIVES

Building on the gaps identified in the literature, the overarching goal of this dissertation is:

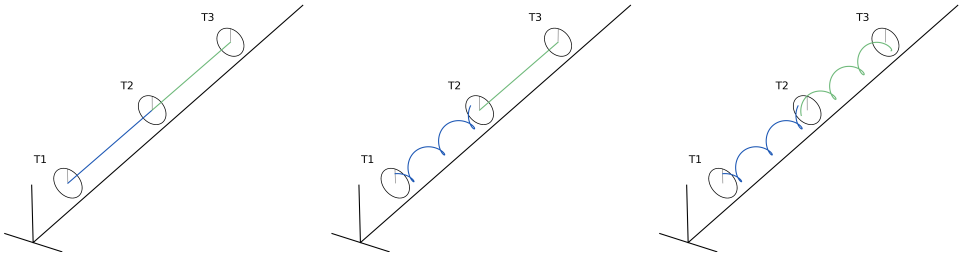

(a) Helix off on all turbines. (b) Helix on T1 only. (c) Helix on T1 and T2.

Figure 1.6: Schematic representation of different helix actuation setups.

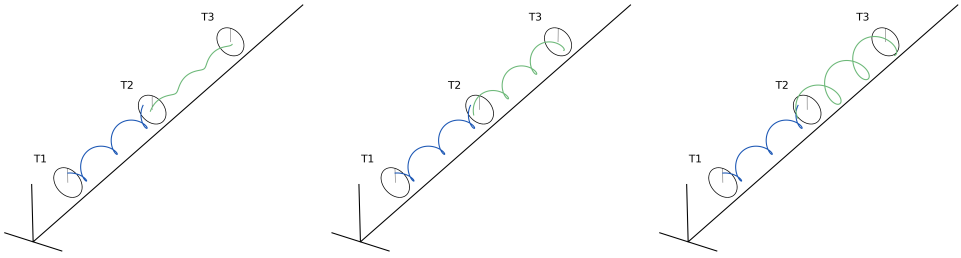

(a) Destructive interference (b) No interference (c) Constructive interference

Figure 1.7: Schematic representation of wake flow interferences during synchronization.

> **Dissertation goal:** *To extend dynamic wake mixing strategies such as the Helix approach beyond isolated turbine applications, and to develop methods that enable their effective use in deeper wind farm arrays through synchronized control.*

Achieving this goal requires a systematic approach to mature the technology from early conceptual development to experimental demonstration, corresponding to an advancement across Technology Readiness Levels (TRLs) (Rijksdienst voor Ondernemend Nederland (RVO) 2022). In particular, this dissertation aims to advance TRL 1 to TRL 4: from establishing the fundamental principles and load trade-offs (TRL 1-2), to developing control and estimation algorithms (TRL 3), and validating these in high-fidelity and wind tunnel experiments (TRL 4-5). As such, the research is structured around four interrelated themes examined through six specific research objectives (ROs):

LOAD IMPLICATIONS OF DYNAMIC WAKE MIXING

Before synchronization control can be attempted, it is important to understand the structural implications of wake mixing control. This theme investigates the feasibility of the Helix approach from a loads perspective, providing fundamental insights for conceptual synchronization controller development.

RO1: Quantify the structural impact of the Helix approach on the actuating (upstream) turbine. Particular attention must be given to pitch bearing damage, which is critical for assessing the long-term feasibility of dynamic pitching strategies in wind turbines.

REAL-TIME ESTIMATION AND FEEDBACK CONTROL

With the feasibility and constraints of dynamic wake mixing established, the next step is to enable real-time synchronization across turbines. This involves designing feedback and estimation strategies that operate under realistic information constraints, advancing the TRL towards conceptual algorithm design (TRL 3).

RO2: Develop and evaluate an output-feedback control strategy for synchronized wake mixing that enables downstream turbines to exploit upstream wake structures using only local rotor-level measurements, while allowing for a toggling between power optimization and load rejection.

RO3: Design and implement an estimator-based framework to reconstruct the phase of periodic wake-induced flow structures in real time. The estimator must be designed to enable out-of-phase synchronization across the turbine array.

VALIDATION IN SIMULATION AND EXPERIMENT

To transition from theoretical development to demonstrable capability (from TRL 3 to TRL 4–5), the proposed methods must be validated in both simulation and controlled physical environments. This validation provides confidence in the scalability and practical relevance of the control strategies.

RO4: Validate the effectiveness of synchronized wake mixing control in realistic high-fidelity LES using modern reference wind turbines, assessing both power and load implications across different synchronization settings.

RO5: Demonstrate the feasibility of synchronized control experimentally in a wind tunnel setup using a scaled turbine array. This includes real-time phase estimation, closed-loop synchronization, and downstream performance evaluation.

INSIGHT INTO WAKE SYNCHRONIZATION MECHANISMS

To support ongoing development around and beyond TRL 5, a deeper understanding of the underlying fluid dynamics is required. This theme focuses on explaining the mechanisms behind performance improvements under synchronized control.

> **RO6:** Investigate the physical mechanisms responsible for performance changes under synchronized control. Flow analyses must be used to identify how phase alignment, coherent structures, and turbulence interactions contribute to wake recovery and downstream performance gains.

This dissertation is, to the author's knowledge, the first to numerically and experimentally demonstrate synchronized Helix wake mixing control in a multi-turbine array using real-time phase estimation. The integration of model-based estimation, closed-loop control, and numerical and experimental validation represents an important step toward the practical deployment of dynamic wind farm control methods, advancing the synchronization technology towards TRL 5.

1.6. DISSERTATION OUTLINE

The remainder of this dissertation is structured around four core research chapters, each covering one or more specific objectives within the overall goal of enabling synchronized dynamic wake mixing control in wind farms. Note that this dissertation is paper-based. Each chapter can be read as a stand-alone scientific article, which results in some repetition of concepts, especially in the chapter introductions.

Chapter 2 (RO1) quantifies the structural impact of the Helix control strategy on the actuating turbine. A sensitivity study on Helix settings is performed, providing context for the decision between clockwise and counterclockwise Helix.

Chapter 3 (RO2 & RO4) develops and evaluates an output-feedback control strategy for synchronized wake mixing and load rejection. The controller uses local measurements to synchronize downstream actuation with upstream wake dynamics, enabling *in-phase* coordination without explicit flow field measurements or estimation.

Chapter 4 (RO3 & RO5) presents a linear Kalman filter for real-time wake phase estimation and evaluates its implementation in a wind tunnel experiment. The chapter demonstrates synchronized Helix control in a three-turbine setup and analyzes the sensitivity of performance to phase alignment between upstream and downstream wakes.

Chapter 5 (RO3, RO4, & RO6) proposes an extended Kalman filter for improved phase estimation in turbulent flow and evaluates its performance in high-fidelity LES. Flow field analyses are performed to uncover the physical mechanisms that govern synchronization performance, including the influence of applied phase shifts.

Chapter 6 provides an overarching concluding chapter to this dissertation, integrating findings across individual chapters to address the dissertation goal and research objectives. Building on these insights, recommendations are made that provide guidance to future research in this field.

2

EFFECTS OF HELIX SETTINGS ON LOADS AND PITCH BEARING DAMAGE

The Helix approach is a control technology that reduces the wake effect in wind farms by accelerating wake mixing through individual pitch control, resulting in significant AEP gain. However, this study found that depending on its settings, the controller may increase pitch bearing damage and loads on some turbine components. Using a modified version of NREL's Reference OpenSource Controller in OpenFAST, this study analysed the sensitivity of loads and pitch bearing damage to different Helix controller settings on the IEA-15MW reference offshore wind turbine. Results showed that loads increased with the excitation signal amplitude but were less affected by its frequency. Additionally, more pitch bearing damage was observed in the counterclockwise Helix direction, while slightly higher loads were observed in the clockwise direction when using the same excitation signal amplitude and frequency for both directions.

This chapter is based on previously published work:
van Vondelen, A. A. W., Navalkar, S. T., Kerssemakers, D. R. H., and Van Wingerden, J. W. (2023). "Enhanced wake mixing in wind farms using the Helix approach: A loads sensitivity study". In: *2023 American Control Conference (ACC)*, pp. 831–836. DOI: 10.23919/ACC55779.2023.10155965.

Contents

2.1. INTRODUCTION

The Netherlands committed to obtaining all of its energy from renewable sources by 2050 (Ministerie van Algemene Zaken 2022). Due to shallow waters and strong winds in the Dutch North Sea, offshore wind will play a large role in this transition. Recently, this was confirmed by doubling the desired capacity for 2030 to 21 GW (Ministerie van Algemene Zaken 2021). Even though the cost per kWh of offshore wind energy is already on par with fossil fuels, lowering the cost further will expedite the transition. Technological innovation in wind engineering is expected to contribute significantly to this, and one important open challenge that demands innovation is a disturbing phenomenon called the wake effect.

The wake is a low-velocity flow region downwind of a turbine, which propagates further downwind until it becomes unstable and mixes again with the surrounding ambient wind flow (Burton *et al.* 2011). If a downstream wind turbine is (partly) aligned with the wake of an upstream wind turbine, it experiences a lower wind velocity and yields a lower power output (Adaramola and Krogstad 2011). Moreover, due to increased turbulence and partial wake overlap, the downstream turbine also experiences higher loads (Thomsen and P. Sørensen 1999). For that reason, mitigating the wake effect plays a large role in wind farm layout optimization (Manwell, McGowan, and Rogers 2010; Yang *et al.* 2019). In spite of that, the power losses due to the wake effect can be as high as 20% for some wind farms (Barthelmie *et al.* 2009).

The field that attempts to mitigate this effect using control is called wind farm control (WFC). A recent study investigated the main motivations for wind farm control where a survey was passed amongst stakeholders from academia, industry, and other fields (van Wingerden *et al.* 2020). The most important benefit of WFC was found to be the increase in energy production, whereas load reduction came second. Traditionally, these two objectives contradict, as higher production generally involves higher wind speeds and thus higher loads. However, WFC aims at optimizing both objectives on a farm level.

One popular technique in WFC that received much attention is wake steering (Fleming, Gebraad, *et al.* 2014; Wagenaar, Machielse, and Schepers 2012). This approach employs a farm-wide super controller that intentionally misaligns upstream turbines with respect to the dominant wind direction such that their wakes are steered to pass on one side of the downstream turbine. Another technique involves derating upstream turbines such that more energy can be drawn by downstream turbines. However, the effectiveness of this method is still a topic of discussion as some studies haven't found significant increases in performance (Annoni, Gebraad, *et al.* 2016; van der Hoek, Kanev, *et al.* 2019).

The above-mentioned techniques aim to find a steady-state optimum for a given environmental condition. Other techniques were proposed that introduce dynamics to initiate earlier mixing of the wake with the ambient wind flow. One method called Dynamic Induction Control (DIC) imposes a low-frequent sinusoidal signal on the collective pitch actuators causing a periodically varying thrust force improving wake mixing significantly (Frederik, Weber, *et al.* 2020; Goit and Meyers 2015; van der Hoek, Frederik, *et al.* 2022). The parameter that governs the frequency of this signal is the dimensionless Strouhal number, whose optimal setting was found experimentally (Munters and Meyers 2018b). These results show great potential for this technique. However, a notable disadvantage is that the pulsing thrust causes significant loads on the blades and tower

base, reducing fatigue life substantially (Frederik and van Wingerden 2022).

Recently, the Helix approach was proposed which uses individual pitch control (IPC) to initiate early wake mixing (Frederik, Doekemeijer, *et al.* 2020). Similar to DIC, the Helix method imposes sinusoids on the blade pitch actuators and is governed by the Strouhal number. However, by imposing out-of-phase pitch actuation signals on the individual blades, a helix-shaped wake is created behind the turbine which enhances wake mixing. Initial simulations demonstrated that, as the wake breaks down earlier, the power production of a two-turbine wind farm was increased by up to 7.5%, and thrust fluctuations (and loads resulting from this) are significantly lower when using this method compared to DIC (Frederik, Doekemeijer, *et al.* 2020; Frederik and van Wingerden 2022).

Being a relatively new approach, no quantitative investigation has been done in the optimal settings of the Helix control method balancing fatigue stress with energy gain. This study aims to complete the first part.

The main contribution of this chapter is a loads sensitivity analysis for the Strouhal number and signal amplitude which can be used as a precursor for high-fidelity large-eddy simulation (LES) farm studies where the power production of the downstream turbine can be measured. At this stage, only fatigue loads during normal power production (IEC-6100-3, DLC 1.2 (International Electrotechnical Commission 2019)) are considered, as, under Helix control, turbine operation is largely within its normal operational envelope, and the response to extreme events is not expected to be significantly different.

The remainder of this chapter is organized as follows. Section 2.2 describes the theoretical background of the Helix approach and loads analysis. Section 2.3 presents the simulation setup. The results are presented in Section 2.4 and the chapter is concluded in Section 2.5.

2.2. THEORETICAL BACKGROUND

This section introduces the underlying principle of the Helix. Next, the fatigue analysis methodology is described, followed by the pitch bearing damage quantification.

2.2.1. THE HELIX APPROACH

The Helix approach is an open-loop wake mixing control method that uses the individual pitch actuators of the blades of a wind turbine. Similar to IPC for load reduction (Bossanyi 2003; Selvam *et al.* 2009), it uses the Multi-Blade Coordinate (MBC) transform (Bir 2008). This coordinate transformation maps the rotating coordinate system of the individual blades to the non-rotating coordinate system. Thereby, this transformation decouples the blade root bending moments, $M_i(t)$ for $i = 1,2,3$, to a collective moment M_0, a moment around the tilting axis M_{tilt} and a moment around the yawing axis M_{yaw} using the azimuth ψ_i of each blade $i = 1,2,3$:

$$\begin{bmatrix} M_0(t) \\ M_{\text{tilt}}(t) \\ M_{\text{yaw}}(t) \end{bmatrix} = \frac{2}{3} \begin{bmatrix} 0.5 & 0.5 & 0.5 \\ \cos(\psi_1) & \cos(\psi_2) & \cos(\psi_3) \\ \sin(\psi_1) & \sin(\psi_2) & \sin(\psi_3) \end{bmatrix} \begin{bmatrix} M_1(t) \\ M_2(t) \\ M_3(t) \end{bmatrix}. \tag{2.1}$$

Traditionally speaking, straightforward SISO PID control can then be used for load reduction, while collective pitch can be controlled using the baseline pitch controller. Note

that in practice, actuator delays might prevent full decoupling, and an additional correction is required (Mulders *et al.* 2019).

The Helix approach, being open-loop, only imposes a signal on the tilt and yaw inputs, θ_{tilt} and θ_{yaw}, which are translated to inputs for the pitch actuators in the rotating frame using the following 'reverse' MBC transform:

$$\begin{bmatrix} \theta_1(t) \\ \theta_2(t) \\ \theta_3(t) \end{bmatrix} = \begin{bmatrix} 1 & \cos(\psi_1) & \sin(\psi_1) \\ 1 & \cos(\psi_2) & \sin(\psi_2) \\ 1 & \cos(\psi_3) & \sin(\psi_3) \end{bmatrix} \begin{bmatrix} \theta_0(t) \\ \theta_{\text{tilt}}(t) \\ \theta_{\text{yaw}}(t) \end{bmatrix}. \tag{2.2}$$

The signals imposed through the MBC by the Helix approach are given as follows:

$$\begin{aligned} \theta_{\text{tilt}} &= \alpha \sin(\omega_{\text{e}} t), \\ \theta_{\text{yaw}} &= \alpha \sin(\omega_{\text{e}} t + \tau), \end{aligned} \tag{2.3}$$

where α is the pitch amplitude in degrees, τ is the time delay in radians per second and $\omega_{\text{e}} = 2\pi f_{\text{e}}$ is the excitation frequency in radians per second. Applying these signals induces a yaw and tilt moment on the non-rotating coordinate frame, misaligning the direction of the thrust force from the rotor center in a dynamic fashion. Generally, a time delay of $\pi/2$ or $3\pi/2$ is selected, which generates a counterclockwise and a clockwise rotating wake, respectively (see Fig. 2.1 for a schematic overview of the Helix approach). The amplitude is usually selected between 0.5 and 4 degrees. As the pitch angle oscillates with this amplitude around the optimal pitch value for a specific wind speed, an upper bound will likely be imposed in practice by the dynamic stall region. A lower bound might be set by the pitch bearing specifications, mitigating the risk for surface-induced damage on the bearing caused by small oscillations (Stammler, Reuter, and Poll 2018).

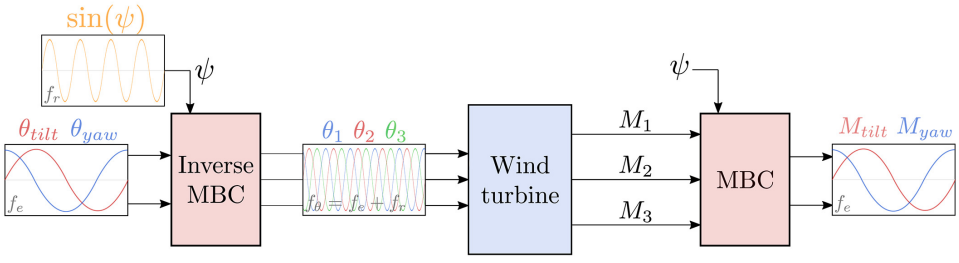

Figure 2.1: Schematic of the MBC transform and the Helix approach (Frederik, Doekemeijer, *et al.* 2020).

When the turbine is operating below rated at constant speed ω_{r}, the collective pitch $\theta_0 = 0$ and the azimuth ψ_i can be taken as $\omega_{\text{r}} t$. Then, if choosing $\tau = \pi/2$ and substituting

Eq. (2.3) in Eq. (2.2) for a blade $\theta_i(t)$ for $i = 1,2,3$, yields:

$$\begin{aligned}\theta_b(t) &= \begin{bmatrix}1 & \cos(\psi_i) & \sin(\psi_i)\end{bmatrix}\begin{bmatrix}0\\ \alpha\sin(\omega_e t)\\ \alpha\cos(\omega_e t)\end{bmatrix}, \\ &= \cos(\omega_r t+\psi_{0,i})\sin(\omega_e t)+\sin(\omega_r t+\psi_{0,i})\cos(\omega_e t), \\ &= \sin((\omega_r+\omega_e)t+\psi_{0,i}),\end{aligned} \tag{2.4}$$

from which it can be derived that the resulting pitch command has a frequency of $\omega_\theta = \omega_r + \omega_e$, with $\omega_e \ll \omega_r$. A similar derivation for clockwise Helix ($\tau = 3\pi/2$) can be performed, yielding a frequency of $\omega_\theta = \omega_r - \omega_e$.

The excitation frequency f_e is governed by the dimensionless Strouhal number St and scales with turbine rotor size D and ambient wind speed U_∞:

$$\mathrm{St} = \frac{f_e D}{U_\infty}. \tag{2.5}$$

The Strouhal is generally taken between 0.1 and 1. Unlike for DIC, the Strouhal value yielding the highest power production for has not been formally determined yet. However, one study analysed a small number of cases and found 0.4 a suitable value (Muscari *et al.* 2022).

2.2.2. FATIGUE ANALYSIS

Fatigue is the damage that builds up in structures over time due to cyclic loading. This damage consists of small cracks that propagate gradually until reaching a point of failure. Structural parameters, such as the damping and natural frequencies, govern the magnitude of the responses to this cyclic loading. Therefore, having adequate knowledge of these parameters is important, as wind turbines are generally designed to withstand cyclic loading from their environment for at least 20 years (van Vondelen, Navalkar, Iliopoulos, *et al.* 2022).

The damaging effect of cyclic loading on a structure can be modelled using the S-N (or Wöhler) curve, which indicates the number of cycles a structure can endure until failure for the given stress through which it is cycled (Burton *et al.* 2011). Its slope is used in the calculation of the damage equivalent load (DEL), which encapsulates the total fatigue damage experienced by a structure in one single load, equivalent to the total damage of different load cycles experienced by that structure over time. Additionally, the DEL requires the ranges and frequencies of different load cycles, which can be extracted from a load signal using rainflow counting. To use these cycles in the DEL, the means need to be corrected to a single mean value. This is accomplished using the Goodman correction:

$$A_i^{\mathrm{RF}} = A_i\left(\frac{A^{\mathrm{u}} - |A^{\mathrm{fm}}|}{A^{\mathrm{u}} - |A_i^{\mathrm{m}}|}\right), \tag{2.6}$$

where A_i^{RF} is the Goodman-corrected range, A_i is the range and A^{m} is the mean of the i^{th} cycle, A^{u} is the ultimate load, and A^{m} is the chosen fixed mean load, set here as the mean of the entire signal.

The DEL is then calculated as follows:

$$\mathrm{DEL} = \left(\frac{\sum_{i=1}^{N} (A_i^{\mathrm{RF}})^m n_i}{n_{\mathrm{eq}}} \right)^{\frac{1}{m}}, \tag{2.7}$$

where N is the total number of cycles, m is the inverse Wöhler slope taken conventionally as 5 for the tower and 10 for the blades, n_i is the number of cycles with range A_i, and n_{eq} the equivalent cycle, set here as 1. NREL's MLife toolbox was used to perform these calculations (Hayman 2012).

Observing the equation for DEL in Eq. (2.7), and considering that the Helix approach actuates the wind with oscillating pitch action Eq. (2.3), it is expected that Helix pitch action generates additional vibrations in the turbine which increase in magnitude with increasing Helix amplitude, thus contributing to the DEL. Moreover, as the DEL equation sums all cycles, it is also expected that the DEL increases with increasing Strouhal. In this study, the DELs are calculated for the following components:

- Blade Root Moment: Edgewise, Flapwise, and Torsional direction
- Tower Top Moment: Fore-aft, Side-side, and Torsional direction
- Tower Base Moment: Fore-aft and Side-side direction

2.2.3. PITCH BEARING DAMAGE

Pitch bearing damage (PBD) is not quantified using rainflow counting. The standard used in this study is one prescribed by bearing manufacturers and given by the following equation:

$$\mathrm{PBD}(\phi) = \sum_{k=1}^{N} \delta\theta(k) (\max(\cos(\phi) M_{\mathrm{flap}}(k) + \sin(\phi) M_{\mathrm{edge}}(k), 0))^m, \tag{2.8}$$

where $\delta\theta$ is the pitch difference, ϕ is the radial position of the bearing, M_{flap} is the flapwise blade root bending moment, M_{edge} is the edgewise blade root bending moment, and m is the inverse Wöhler slope. In our analysis, the radial position with the largest damage is considered.

Analysing Eq. (2.8), PBD is expected to increase for higher frequent pitch action as pitch travel increases. This is the case for increasing Strouhal for CCW Helix and for decreasing Strouhal for CW Helix (See Eq. (2.4)).

2.3. SIMULATION SETUP

In this section, the simulation software and tools are presented. First, the analysed turbine, then the turbine controller, and ultimately a description of the simulation environment is given, along with the simulated controller parameters.

2.3.1. IEA-15MW OFFSHORE WIND TURBINE

The turbine considered here is the fixed-bottom IEA-15MW reference offshore turbine with a radius of 120 m and a hub height of 150 m. The turbine is a direct-drive offshore wind turbine with a cut-in wind speed of 4 m/s, a rated wind speed of 10.59 m/s, and a rated RPM of 7.55. For a more elaborate description, the reader is referred to the technical report (Gaertner *et al.* 2020).

2.3.2. CONTROLLER

The IEA-15MW turbine is equipped with the reference open-source controller (ROSCO). This controller has state-of-the-art control capabilities, such as peak-shaving and individual pitch control (Abbas, D. S. Zalkind, *et al.* 2022).

Note that enhanced wake mixing is not expected to be economical in the above-rated regime as added loads increase and added power decreases due to the abundance of wind (Frederik and van Wingerden 2022). Practical implementation of the Helix approach will therefore most likely be confined to the below-rated region. Hence, the ROSCO controller is modified such that the Helix signal can be superimposed in region 2.

2.3.3. SIMULATION ENVIRONMENT

The IEA-15MW turbine with ROSCO + Helix controller is simulated in OpenFAST v3.1.0 (J. M. Jonkman 2013), a well-established medium-fidelity aero-elastic wind turbine simulation tool.

The simulation sampling frequency is chosen as 200 Hz and lasts 900 seconds, where the first 300 s are discarded to remove transient effects. Furthermore, each simulation is run with 6 different turbulent wind seeds, whose calculated DELs are averaged to reduce variance. Simulations are conducted for the entire wind speed range in region 2 (3–10 m/s) using inflow with IEC normal turbulence model level C based on the IEC Kaimal spectral model. The Helix amplitude is varied between 0.25 and 4 degrees, and the Strouhal is varied between 0.1 and 1 for both clockwise and counterclockwise directions. Besides simulations with Helix control, baseline simulations are conducted to provide a comparison. Altogether, this totals 15,408 simulations that were computed on the Delft Blue high-performance computer using 1200 CPU cores (Delft High Performance Computing Centre 2022). A summary of the parameters is given in Table 2.1.

Table 2.1: Overview of the parameter settings used in the simulations.

Parameter	**Values**	**Steps**
Wind speed	3 - 10 m/s	1
Strouhal	0.1 - 1	0.1
Amplitude	0.25 - 4 deg	0.25

2.4. RESULTS

The DELs and PBD for the CW and CCW direction are presented in 3D surface plots in Fig. 2.2. The x- and y-axis represent the amplitude and Strouhal value used in the simulation. The z-axis shows the Helix DEL relative to the baseline DEL. For PBD, the z-axis shows the absolute value as a relative comparison would not be informative: almost no PBD builds up at below-rated wind speeds due to little pitch action. All results were averaged over 6 seeds and Weibull weighted across wind speeds. The CW surface plot has a red grid, the CCW surface plot has a black grid, and a colorbar indicates the magnitude of each DEL.

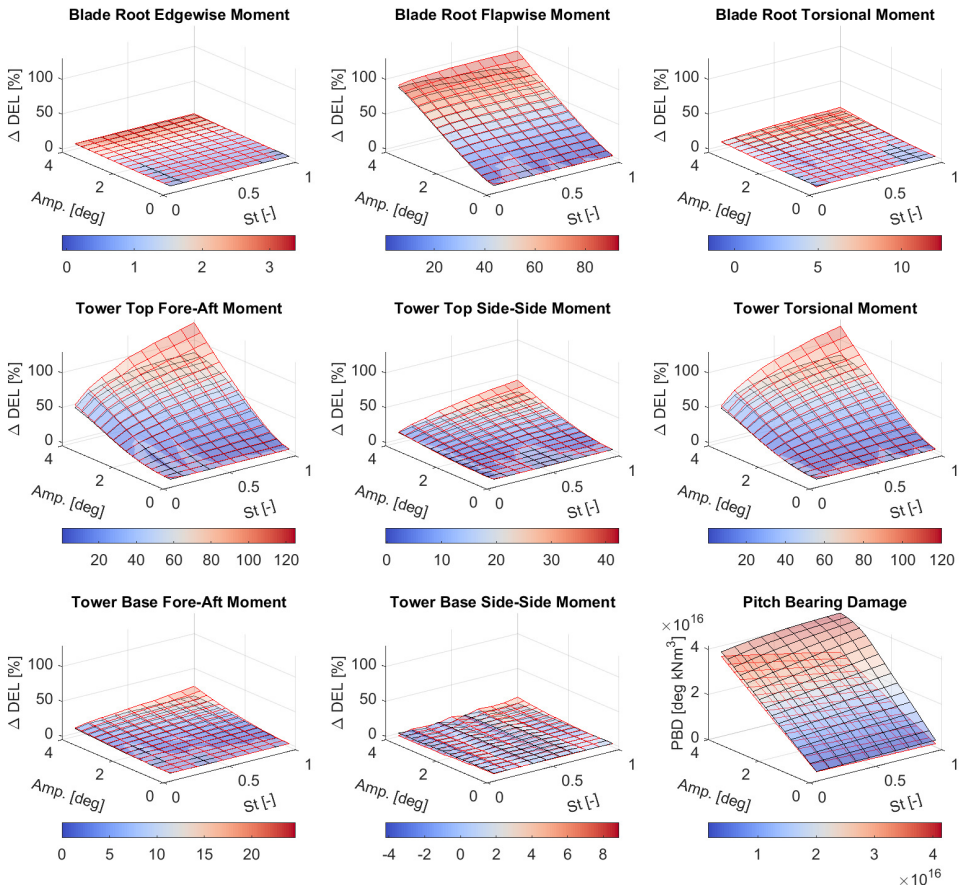

Figure 2.2: 3D surface plots of all parameters simulated for Helix. Each plot presents the DEL relative to the baseline case for CW (red grid) and CCW (black grid) Helix. The x-axis and y-axis describe the different Helix settings, amplitude and Strouhal, respectively. The z-axis describes the relative DEL. Generally, the DELs are higher for CW.

Each channel is qualitatively analysed in Table 2.2. The sensitivity is rated ↑ - ↑↑↑↑,

where ↑ is very low positive sensitivity (↓ for negative sensitivity) and ↑↑↑↑ is very high positive sensitivity; a '–' indicates negligible sensitivity.

Table 2.2: Sensitivity of the DELs to the Helix parameters.

Channel		**Sens. to ↑ Amp.**	**Sens. to ↑ St**
Blade Root Edgewise	CW	↑	–
	CCW	↑	–
Blade Root Flapwise	CW	↑↑↑↑	–
	CCW	↑↑↑↑	↓
Blade Root Torsional	CW	↑	↑
	CCW	↑	–
Tower Top Fore-Aft	CW	↑↑↑	↑↑↑
	CCW	↑↑↑	↑↑
Tower Top Side-Side	CW	↑↑	↑↑
	CCW	↑↑	↑
Tower Torsional	CW	↑↑↑	↑↑↑
	CCW	↑↑↑	↑↑
Tower Base Fore-Aft	CW	↑	↑
	CCW	↑	–
Tower Base Side-Side	CW	↑	–
	CCW	–	–
Pitch Bearing Damage	CW	↑↑↑↑	↓↓
	CCW	↑↑↑↑	↑

From the results, it can be derived that the blade root flapwise, tower top fore-aft, tower torsional and PBD are very sensitive to Helix amplitude. This can be explained by the way Helix operates, which steers the thrust force to follow a circular pattern around the axis instead of being directed upwind. This enforcement increases blade vibrations, especially in the flapwise direction, and creates a fluctuating tilt and yaw moment due to deliberate misalignment with the wind direction, resulting in higher torsional and fore-aft loads in the top part of the tower.

The channels with the largest sensitivity to Strouhal can be found on the tower. This could stem from the fact that a relative increase in Strouhal results in the same relative increase in load cycles on the tower due to Helix control, whereas the resultant frequency on the blades is $\omega_\theta = \omega_\mathrm{r} \pm \omega_\mathrm{e}$ due to the MBC transformation Eq. (2.4) resulting in a lower relative cycle increase for CCW and a cycle decrease for CW. This effect can be observed in greater detail in Fig. 2.3, where several power spectra, averaged over 6 seeds, are presented for different Strouhal settings. In the blade root flapwise channel for CW Helix, the Strouhal peak starts around the 0.1 Hz 1P frequency and decreases for higher Strouhal, while for CCW Helix, the opposite effect is observed. Higher harmonics can also be seen. The Helix peak in the tower top fore-aft channel starts around 0 Hz and increases linearly with Strouhal irrespective of the Helix direction.

Although the number of cycles decreases for CW Helix with increasing Strouhal, the

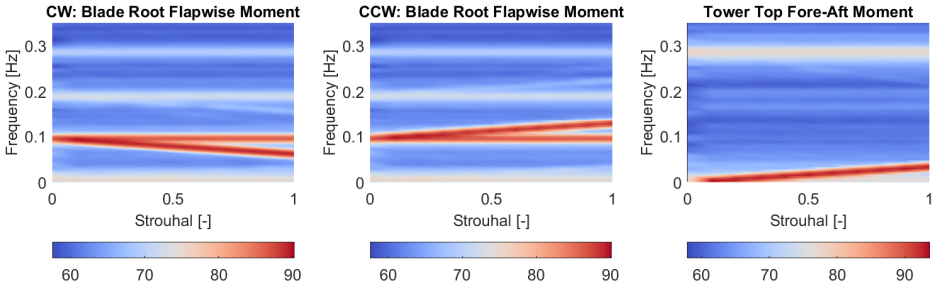

Figure 2.3: Power spectra of several relevant load channels for increasing Strouhal. The resultant Helix excitation frequency decreases in the blade coordinate frame for CW Helix, whereas it increases for CCW Helix. In the tower coordinate frame, the frequencies are identical.

tower DELs increase more compared to CCW Helix. It is difficult to see from power spectra, but it was found that the CW Helix peak has a stronger magnitude compared to CCW Helix: 93.3 versus 92.8 dB, indicating a higher amplitude of the resulting vibrations. For PBD, this is the opposite and can be derived from the fact that the pitch frequency (and hence the pitch difference $\delta\theta$, Eq. (2.8)) increases for CCW Helix and decreases for CW Helix with higher Strouhal.

Note that, although the load increases presented here seem significant, the Helix is expected to be active only 10-20% of the time in practice, as the main performance gain is achieved when the wake effect takes place, i.e. when the turbines are (partly) aligned with the wind direction. Therefore, the added loads should be discounted by this factor, meaning that a load increase of e.g. 30% with Helix activated results in an annual load increase of only 3-6%.

2.5. CONCLUSIONS

The Helix approach is a control strategy that increases wind farm performance by mitigating the wake effect through individual pitch control. This study found that increasing the amplitude of the excitation signal leads to notable increases in pitch bearing damage and turbine loads, particularly in the blade root flapwise, tower top fore-aft, and tower torsional direction. While higher amplitude may result in better wake mixing, further LES studies are needed to determine the trade-off with the loads increase. Loads were less affected by Strouhal, allowing more tuning freedom. The counterclockwise Helix direction was found to cause lower loads, while also performing better in terms of AEP gain. The clockwise Helix direction requires less pitch action, which may be beneficial for turbines with pitch bearing actuation restrictions.

3

OUTPUT FEEDBACK CONTROL FOR SYNCHRONIZED WAKE MIXING

Periodic wakes are created on upstream wind turbines by pitching strategies such as the Helix approach to enhance wake mixing and thereby increase power production for wind turbines directly in their wake. Consequently, a cyclic load is generated on the actuating turbine's blades, but also on the waked wind turbine. While the upstream load is the result of the pitching required for wake mixing, the downstream load originates from interaction with the periodic wake and only causes fatigue damage. This study proposes two novel individual pitch control schemes in which such a periodic load on the downstream turbine can be treated: by attenuation or amplification. The former method improves the fatigue life of the downstream turbine, whereas the latter enhances wake mixing further downstream by exploiting the already-present periodic content in the wake; both validated on a three-turbine wind farm in high-fidelity large-eddy simulations. Fatigue damage reductions of around 10% were found in the load mitigation case, while an additional power enhancement of 6% was generated on the third turbine when implementing the amplification strategy. Both objectives can easily be toggled depending on a wind farm operator's demands and the desired loads/energy capture trade-off.

This chapter is based on previously published work:
van Vondelen, A. A. W., Pamososuryo, A. K., Navalkar, S. T., and van Wingerden, J. W. (2025). "Control of Periodically Waked Wind Turbines". In: *IEEE Transactions on Control Systems Technology* 33.2, pp. 700–713. DOI: 10.1109/TCST.2024.3508577.

Contents

3.1. INTRODUCTION

Reducing the cost of wind energy motivates the establishment of wind farms that profit from shared infrastructure, installation, and maintenance costs. Typically, a minimum spacing of 4-5 rotor diameters is maintained, balancing the benefits of shared costs against reduced farm-level energy production as a result of the wake effect. This event—a phenomenon occurring when up- and downstream wind turbines align with the wind direction—causes reduced production due to lower wind speed and increased loading from wake impingement (González-Longatt, Wall, and Terzija 2012).

The wake effect can lead to substantial power loss, estimated at up to 20%, or an equivalent increase in loads depending on the wind farm layout (Barthelmie *et al.* 2009). Several solutions for the wake effect have been proposed in the past, such as the axial induction control method (Annoni, Gebraad, *et al.* 2016), which derates upstream turbines to leave more energy in the wake for downstream turbines. Studies, however, have shown that the production increase is negligible, making them more suitable for load balancing within wind farms rather than overall production optimization (van der Hoek, Kanev, *et al.* 2019).

A more promising remedy is wake steering, which commands a yaw misalignment in the upstream wind turbine to reposition its wake (Fleming, Gebraad, *et al.* 2014). In this approach, a steady-state optimum is found, balancing the performance loss as a result of the misalignment with the performance gain obtained by alleviating turbines downstream of the wake. Since the wake is only repositioned, it might still affect other turbines further downstream.

A different approach is suggested by (Goit and Meyers 2015), where the wake is reduced by promoting wake mixing through dynamic variation of the induction, a method known as Dynamic Induction Control. One implementation of this method is done by pitching periodically, hence creating a periodic structure in the wake (Frederik, Weber, *et al.* 2020). Significant power gains are found in a two-turbine case; however, significant load increases due to thrust force variations are also shown (Frederik and van Wingerden 2022).

Frederik, Doekemeijer, *et al.* 2020 propose a similar periodic actuation method that, instead of varying the thrust force's magnitude, rotates the direction around its nominal direction, significantly reducing the strong tower loads and varying power production while achieving even better performance. The Helix approach, as it is colloquially called, has since garnered attention in the literature, as extensive large-eddy simulations (LES) (Taschner, van Vondelen, *et al.* 2023) and wind tunnel studies (van der Hoek, Van den Abbeele, *et al.* 2024) have been performed, with multi-sine variations to the baseline Helix also proposed (Huang *et al.* 2023); all with promising results in terms of power gains.

Up until recently, little attention was given to control of the turbine in the Helix wake downstream, while it poses interesting questions. First, the periodic loading as a result of the Helix actuation on the upstream turbine can similarly be found on the downstream turbine. Korb, Asmuth, and Ivanell 2023 show that applying the Helix with a specific phase shift on the downstream turbine yields an additional power gain on the third turbine. They, however, do not propose a method for attaining this phase difference in control action. van Vondelen, Ottenheym, Pamososuryo, *et al.* 2023 suggest a phase syn-

chronization method, which can track the phase of the Helix wake while similarly applying a control action downstream. However, in this method, the quality of the phase estimate depends strongly on the quality of the linear model, which changes for each operating case. It may, therefore, be challenging to obtain exact phase estimates.

The above studies investigate the control of a downstream turbine from a power optimization perspective, while the periodic load could also be mitigated to improve fatigue life. A wind farm developer's objective is often to minimize the levelized cost of energy (LCOE) over the lifetime of the system. This is a particularly useful metric as it considers both operation and maintenance costs (which are directly related to fatigue damage) and the average power generation of the system. In our work, load mitigation and power amplification are considered as separate objectives to provide flexibility in addressing different operational goals. Load mitigation is essential for reducing fatigue damage and maintenance costs, thereby extending the turbine's lifespan. On the other hand, power amplification focuses on maximizing immediate energy capture, which is crucial for improving the overall efficiency of the wind farm. By separating these objectives, operators can tailor the control strategy to the specific needs and conditions of the wind farm, optimizing for either long-term durability or short-term performance as required. This study proposes a controller that can achieve both while relieving the control engineer from deriving a linear model for each operating case. The contributions are hence as follows:

1. Derivation of a novel control scheme for control of periodically-waked wind turbines which can achieve:
   a) Load rejection through regulation;
   b) Power enhancement through synchronization by reference tracking;
2. Evaluation of 1) in a three-turbine large-eddy simulation.

The remainder of this chapter is organized as follows. Section 3.2 introduces the conventional individual pitch control and the Helix, after which Section 3.3 presents the main contributions: the derivation of the novel control schemes. The controllers corresponding to these schemes are tuned based on an identified model in Section 3.4. Section 3.5 presents the simulation setup and test cases. The results of each control objective are treated in separate sections. Section 3.6 presents the results obtained after evaluating the proposed control scheme in LES for the load mitigation objectives, while Section 3.7 analyzes results for the synchronized wake mixing objective. Lastly, conclusions are drawn in Section 3.8.

3.2. INDIVIDUAL PITCH CONTROL AND THE HELIX

In this section, a brief introduction is given to individual pitch control for load reduction and the Helix approach for wake mixing (i.e., power enhancement), which is essential background information for understanding the proposed methods. These approaches both leverage the so-called Multi-Blade Coordinate (MBC) transformation, which is used to map the pitch control system from the *rotating coordinate frame* to the *fixed coordinate frame*. This methodology is exploited in this work to derive a novel coordinate

transformation, which is used to map the pitch control system from the rotating coordinate frame to the *Helix coordinate frame*. As such, a considerable simplification of the pitch control system is obtained, allowing for the derivation of a novel feedback controller for 1) load regulation and 2) phase synchronization for power enhancement, both in this section.

3.2.1. CONVENTIONAL INDIVIDUAL PITCH CONTROL

Significant challenges arise when larger rotors are used for wind turbines, which originate primarily from the increasing asymmetric loads caused by the spatiotemporal variability of the wind. Turbulence, wind shear, and tower shadow are amongst several phenomena that contribute to asymmetric loading, which acts on blades as they traverse through this varying wind field at the rotational frequency (once-per-revolution/1P), and its higher harmonics (2P, 3P, etc.). On the fixed structure, this loading propagates from the rotating system as a steady-state load at 0P and periodic loading at 3P, 6P, and higher in the case of a three-bladed turbine, as considered in this study.

As these loadings shorten fatigue life, and structural reinforcements are costly, individual pitch control for load reduction was proposed as a solution (Bossanyi 2003). This feedback controller exploits the MBC transformation, which maps the blade root out-of-plane moment signals M_i, $i = 1,2,3$, for a three-bladed wind turbine in the rotating blade coordinate frame to the fixed (nonrotating) coordinate frame, where they are collective, tilt, and yaw moments ($M_{\text{col}}, M_{\text{tilt}}$, and M_{yaw}, respectively), a process known as *demodulation* (e.g. Oppenheim, Willsky, and Nawab 1997):

$$\begin{bmatrix} M_{\text{col}} \\ M_{\text{tilt}} \\ M_{\text{yaw}} \end{bmatrix} = \underbrace{\frac{2}{3}\begin{bmatrix} 1/2 & 1/2 & 1/2 \\ \cos(\psi_1) & \cos(\psi_2) & \cos(\psi_3) \\ \sin(\psi_1) & \sin(\psi_2) & \sin(\psi_3) \end{bmatrix}}_{T_{\text{cm}}(\psi(t)=\omega_{\text{r}} t)} \begin{bmatrix} M_1 \\ M_2 \\ M_3 \end{bmatrix}, \tag{3.1}$$

where ψ_i is the azimuthal position of the blades and ω_r is the rotor velocity. Note that ω_r is taken constant here and through the remainder of this chapter for ease of implementation and analyses. Although this is valid for low wind speed variations, the final formulation of the derivations of the main contributions will all depend on the time-dependent azimuth and can therefore be used with time-varying rotor speeds.

In this fixed coordinate frame, the individual pitch commands β_i can now be computed as decoupled collective, tilt, and yaw pitch commands ($\beta_{\text{col}}, \beta_{\text{tilt}}$, and β_{yaw}, respectively), allowing simple single-input single-output (SISO) control loops instead of more complex multiple-input multiple-output (MIMO) control. The 1P blade loading is demodulated here to the DC gain, or 0P frequency, where it is a simple bias that can easily be driven towards zero using integrator control, simplifying the pitch coordinate system significantly. In case of load imbalance, i.e., $M_1 \neq M_2 \neq M_3$, the 1P load is also demodulated to the 2P frequency (van Solingen and van Wingerden 2015).

Ultimately, the determined tilt and yaw commands are then mapped back to the individual blade rotating coordinate frame into pitch commands using the reverse transfor-

mation to *remodulate* the signal back into the original coordinate frame:

$$\begin{bmatrix}\beta_1\\ \beta_2\\ \beta_3\end{bmatrix} = \underbrace{\begin{bmatrix}1 & \cos(\psi_1+\psi_{\text{off}}) & \sin(\psi_1+\psi_{\text{off}})\\ 1 & \cos(\psi_2+\psi_{\text{off}}) & \sin(\psi_2+\psi_{\text{off}})\\ 1 & \cos(\psi_3+\psi_{\text{off}}) & \sin(\psi_3+\psi_{\text{off}})\end{bmatrix}}_{T_{\text{cm}}^{-1}(\psi(t)+\psi_{\text{off}})} \begin{bmatrix}\beta_{\text{col}}\\ \beta_{\text{tilt}}\\ \beta_{\text{yaw}}\end{bmatrix}, \tag{3.2}$$

where ψ_{off} is an azimuth offset accounting for unmodeled actuator delays and blade flexibility, which is required to fully decouple the tilt and yaw channels (Mulders *et al.* 2019).

The principle of modulation-demodulation is well-studied for communication networks but also sees several implementations in wind turbine control, of which individual pitch control using the MBC transform is the most famous example. Other implementations include tower side-side damping control (Pamososuryo *et al.* 2024), and in this work, the same principle will be applied in Section 3.3 to the frequency of the periodic load of the Helix.

3.2.2. THE HELIX APPROACH

The Helix approach is an open-loop control strategy for power enhancement utilizing the MBC transformation to excite the blades with periodic tilt and yaw signals. These signals are determined by setting an amplitude and a frequency, where the latter parameter is governed by the dimensionless Strouhal number:

$$\text{St} = \frac{f_e D}{U_\infty}, \tag{3.3}$$

where f_e is the excitation frequency of the tilt and yaw commands, D is the rotor diameter, and U_∞ is the free stream wind velocity. Strouhal values are generally selected between 0.2 and 0.4 as recommended by previous work (Frederik, Doekemeijer, *et al.* 2020; Goit and Meyers 2015). This leads to the following tilt and yaw pitch commands for Helix wake mixing:

$$\begin{bmatrix}\beta_{\text{tilt}}\\ \beta_{\text{yaw}}\end{bmatrix} = \begin{bmatrix}A\sin(\omega_e t)\\ A\sin(\omega_e t \pm \pi/2)\end{bmatrix}, \tag{3.4}$$

where A is the amplitude, usually no larger than 6 degrees due to practical constraints such as pitch rate limitations, and $\omega_e = f_e 2\pi$. Note that the collective pitch β_{col} is omitted in (3.4) since it is controlled by the collective pitch controller. Collective pitch control optimizes wind turbine performance by simultaneously adjusting the pitch angle of all blades based on rotor speed feedback to maintain consistent power output and rotor speed. This strategy effectively adapts to changing wind conditions, ensuring stability and protection from excessive loads.

Two Helix variants exist, where setting $+\pi/2$ in β_{yaw} yields a clockwise (CW) and $-\pi/2$ a counter-clockwise (CCW) rotating Helix. The actuation frequency in the fixed frame remains the same for both variants. However, the actual frequency applied by the pitch actuator differs once these tilt and yaw control commands are mapped to the rotating frame:

$$\beta_i = \beta_{\text{col}} + \cos(\psi_i)\beta_{\text{tilt}} + \sin(\psi_i)\beta_{\text{yaw}}, \tag{3.5}$$

which yields that the Helix frequency in the rotating frame is at the rotation frequency ω_r plus or minus the excitation frequency ω_e (or $1P \pm f_e$), depending on CW or CCW:

$$\begin{aligned}\beta_i &= \beta_{\text{col}} + A\cos(\omega_r t + \psi_i^0)\beta_{\text{tilt}} + A\sin(\omega_r t + \psi_i^0)\beta_{\text{yaw}},\\ &= A\cos(\omega_r t + \psi_i^0)\sin(\omega_e t) + A\sin(\omega_r t + \psi_i^0)\sin(\omega_e t \pm \pi/2),\\ &= A\sin[(\omega_r \pm \omega_e)t + \psi_i^0],\end{aligned} \tag{3.6}$$

where ψ_i^0 is the phase shift originating from the azimuthal position of blade $i = 1,2,3$ at time $t = 0$. Generally, the CCW Helix results in higher farm-level energy gains (Frederik, Doekemeijer, *et al.* 2020; Taschner, van Vondelen, *et al.* 2023), while the CW Helix is favored for lower damage to the pitch bearing (van Vondelen, Navalkar, Kerssemakers, *et al.* 2023), which can be explained by the lower effective actuation frequency of $1P - f_e$.

A consequence of employing the Helix approach is the generation of periodic loading, which impacts the fatigue life of the actuating turbine (van Vondelen, Navalkar, Kerssemakers, *et al.* 2023). This loading, however, is also found on the downstream turbine, as reported by (Frederik and van Wingerden 2022). As such, it negatively impacts the fatigue life of the downstream turbine as well but could potentially be attenuated using a downstream Helix load regulator. A different solution to this periodic loading would be to exploit the gain at this frequency to enforce wake mixing further downstream by amplifying the load slightly while preserving its phase. Both these ideas are developed in the next section.

3.3. NOVEL DOWNSTREAM CONTROLLERS

This section presents the main contributions of this work, the derivation of a downstream Helix load regulator, and a phase synchronization control scheme.

3.3.1. DOWNSTREAM HELIX LOAD REGULATOR

Now, the derivation of the novel downstream Helix load regulator is performed. The principle of modulation-demodulation is applied to transform the rotating coordinate frame of the pitch control system to the Helix coordinate frame, which demodulates the to-be-attenuated $1P + f_e$ load[1] to the DC gain. This diverges from the conventional MBC transformation, which maps to the fixed coordinate frame (1P frequency to DC gain). In the Helix coordinate frame, the Helix load can be regulated using two simple integrator control loops. An overview of the loads and their demodulated frequencies in different coordinate frames is given in Table 3.1.

Let the MBC transformation (3.1) now include the excitation frequency ω_{e} to map to the Helix coordinate frame, we have:

$$\begin{bmatrix} M_{\text{col,e}} \\ M_{\text{tilt,e}} \\ M_{\text{yaw,e}} \end{bmatrix} = T_{\text{cm}}(\omega_{\text{t}} t) \begin{bmatrix} M_1 \\ M_2 \\ M_3 \end{bmatrix}, \tag{3.7}$$

[1] In the remainder of this chapter, the CCW Helix load of $1P + f_e$ is assumed, but note that this value can be substituted for CW Helix or any desired frequency that acts on the turbine rotor.

Table 3.1: Demodulated loads in each reference frame.

	Coordinate frame		
Load	**Rotating**	**Fixed**	**Helix**
Wind-induced rotor asymmetry	$1P$	DC	f_e
Helix	$1P \pm f_e$	f_e	DC

where,

$$T_{\text{cm}}(\omega_{\text{t}} t) = \frac{2}{3}\begin{bmatrix} 1/2 & 1/2 & 1/2 \\ \cos(\psi_1 + \omega_{\text{e}} t) & \cos\left(\psi_2 + \omega_{\text{e}} t\right) & \cos\left(\psi_3 + \omega_{\text{e}} t\right) \\ \sin(\psi_1 + \omega_{\text{e}} t) & \sin\left(\psi_2 + \omega_{\text{e}} t\right) & \sin\left(\psi_3 + \omega_{\text{e}} t\right) \end{bmatrix},$$

where $M_{\text{col,e}}, M_{\text{tilt,e}}, M_{\text{yaw,e}}$ are the orthogonal moment axes in the Helix coordinate frame and $\omega_{\text{t}} = \omega_{\text{r}} + \omega_{\text{e}}$.

For ease of implementation, it is useful to decompose $T_{\text{cm}}(\omega_{\text{t}} t)$; thus, the angle sum identity is used:

$$\begin{bmatrix} \cos(\omega_{\text{r}} t + \omega_{\text{e}} t) \\ \sin(\omega_{\text{r}} t + \omega_{\text{e}} t) \end{bmatrix} = \begin{bmatrix} \cos(\omega_{\text{e}} t) & -\sin(\omega_{\text{e}} t) \\ \sin(\omega_{\text{e}} t) & \cos(\omega_{\text{e}} t) \end{bmatrix} \begin{bmatrix} \cos(\omega_{\text{r}} t) \\ \sin(\omega_{\text{r}} t) \end{bmatrix} \tag{3.8}$$

This allows the decomposition of (3.7) into:

$$\begin{bmatrix} M_{\text{col,e}} \\ M_{\text{tilt,e}} \\ M_{\text{yaw,e}} \end{bmatrix} = \underbrace{\begin{bmatrix} 1 & 0 & 0 \\ 0 & \cos(\omega_{\text{e}} t) & -\sin(\omega_{\text{e}} t) \\ 0 & \sin(\omega_{\text{e}} t) & \cos(\omega_{\text{e}} t) \end{bmatrix}}_{R(\omega_{\text{e}} t)} \times \underbrace{\frac{2}{3}\begin{bmatrix} 1/2 & 1/2 & 1/2 \\ \cos(\psi_1) & \cos\left(\psi_2\right) & \cos\left(\psi_3\right) \\ \sin(\psi_1) & \sin\left(\psi_2\right) & \sin\left(\psi_3\right) \end{bmatrix}}_{T_{\text{cm}}(\psi(t))} \begin{bmatrix} M_1 \\ M_2 \\ M_3 \end{bmatrix}, \tag{3.9}$$

with $R(\omega_{\text{e}} t)$ as a rotation matrix. Following a similar methodology, the reverse transformation is found as follows:

$$\begin{bmatrix} \beta_1 \\ \beta_2 \\ \beta_3 \end{bmatrix} = \underbrace{\begin{bmatrix} 1 & \cos(\psi_1) & \sin(\psi_1) \\ 1 & \cos\left(\psi_2\right) & \sin\left(\psi_2\right) \\ 1 & \cos\left(\psi_3\right) & \sin\left(\psi_3\right) \end{bmatrix}}_{T_{\text{cm}}^{-1}(\psi(t))} \times \underbrace{\begin{bmatrix} 1 & 0 & 0 \\ 0 & \cos(\omega_{\text{e}} t) & \sin(\omega_{\text{e}} t) \\ 0 & -\sin(\omega_{\text{e}} t) & \cos(\omega_{\text{e}} t) \end{bmatrix}}_{R^{-1}(\omega_{\text{e}} t)} \begin{bmatrix} \beta_{\text{col,e}} \\ \beta_{\text{tilt,e}} \\ \beta_{\text{yaw,e}} \end{bmatrix}. \tag{3.10}$$

The above derivation shows that mapping to the Helix coordinate frame is, in fact, a time-varying rotation applied to the system in the fixed coordinate frame. A schematic overview of the proposed control scheme in the Helix coordinate frame is shown in Fig. 3.1. Here, $M_{\text{tilt,e}}$ and $M_{\text{yaw,e}}$ are regulated using two SISO loops, which are schematically depicted in Fig. 3.2. Note that low-level controllers convert the commanded blade pitch setpoints to hydraulic actuation. Since their dynamics are fast compared to the upper-level controller, they are unmodeled. Section 3.4 will elaborate on the synthesis of these SISO controllers.

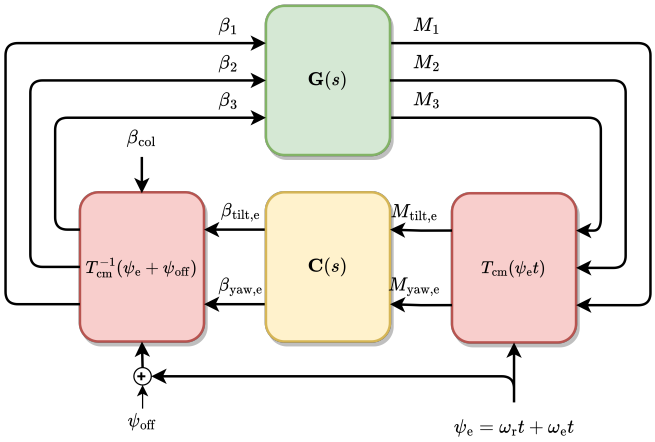

Figure 3.1: Proposed control scheme in closed-loop.

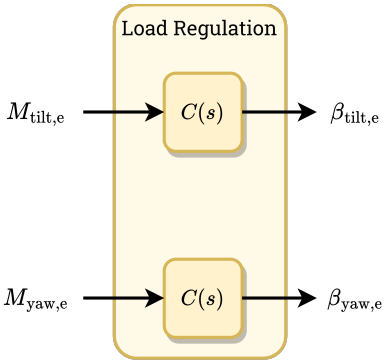

Figure 3.2: Controller architecture 1: load regulation scheme.

The next section will show that, instead of attenuating the load caused by the actuating upstream turbine as derived above, the downstream turbine could also amplify this load, potentially leveraging the periodic content wake to extend the wake mixing further downstream.

3.3.2. DOWNSTREAM HELIX PHASE SYNCHRONIZATION

The control architecture of the Downstream Helix load regulator may be extended to obtain a reference tracking controller, which can achieve phase synchronization with the load generated by the incoming wake. This is achieved by setting a reference to the $M_{\text{tilt,e}}$ and $M_{\text{yaw,e}}$ signals. Since the objective is phase synchronization, the phase should be preserved. Therefore, it is first extracted from the measured signals as follows:

$$\phi_{\text{e}} = \text{atan2}\left(M_{\text{tilt,e}}, M_{\text{yaw,e}}\right). \tag{3.11}$$

Subsequently, an amplitude reference $\mathbf{M}_\mathbf{e}^{\text{ref}}$ is defined, which, for amplification, and thus the propagation of the wake mixing strategy, should be set larger than the amplitude of the measured signals:

$$\mathbf{M}_\mathbf{e}^{\text{ref}} > \mathbf{M}_\text{e} = \left\| \begin{bmatrix} M_{\text{tilt,e}} \\ M_{\text{yaw,e}} \end{bmatrix} \right\|_2 . \tag{3.12}$$

The error is then obtained as follows:

$$\mathbf{M}_\text{e}^{\text{err}} = \mathbf{M}_\text{e} - \mathbf{M}_\mathbf{e}^{\text{ref}} \tag{3.13}$$

Finally, the error signals are constructed as:

$$\begin{bmatrix} M_{\text{tilt,e}}^{\text{err}} \\ M_{\text{yaw,e}}^{\text{err}} \end{bmatrix} = \mathbf{M}_\mathbf{e}^{\text{err}} \begin{bmatrix} \sin(\phi_e) \\ \cos(\phi_e) \end{bmatrix}, \tag{3.14}$$

which preserves the phase of the periodic load. The control architecture of the phase synchronization method is schematically displayed in Fig. 3.3.

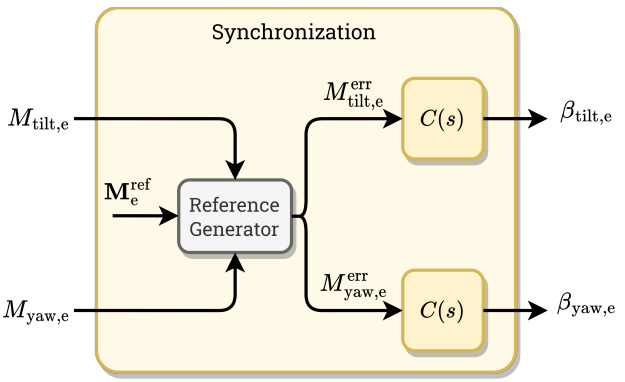

Figure 3.3: Controller architecture 2: Helix synchronization scheme.

3.4. CONTROLLER SYNTHESIS

After deriving the novel coordinate transformation in the previous section, this section aims to synthesize suitable proportional-integral-derivative (PID) controllers for the system in this framework through loop shaping. First, a linear model of the system (described in Section 3.5) in Helix coordinates is identified by means of black box system identification. Then, using the identified model, PID controllers are tuned by using classical loop shaping techniques.

To identify a model, the optimized predictor-based subspace identification ($\text{PBSID}_{\text{opt}}$) (Van der Veen *et al.* 2013) method is used—an algorithm based on the well-known stochastic subspace identification method. This approach uses input/output data to

estimate a linear model, which is obtained by persistently exciting the system with an input signal containing a broad spectrum of frequencies. As an excitation signal, pseudo-random binary noise is chosen, which is bandpass-filtered between 1e-3 and 1e2 rad/s to accommodate the actuator bandwidth. A high-fidelity LES, using the simulation settings specified in Section 3.5, is run to obtain the input/output data. Since a linear identification method is used, the obtained model is linear-time invariant and, therefore, only valid for a specific operating range.

The singular values yielded by the $\text{PBSID}_{\text{opt}}$ method assist in determining an optimal identification order, where an order of 10 was found to correspond best to the spectral average of the input-output data, as can be observed in Fig. 3.4. Note the difference in steady-state magnitude between the diagonal and off-diagonal transfers, denoting the degree of coupling the system has. A low coupling is desired, which simplifies controller synthesis as a SISO control loop can be used on each diagonal transfer. In this work, an azimuth offset of $\psi_{\text{off}} = 8$ degrees is used to facilitate further decoupling (Mulders *et al.* 2019). However, the identified model is based on standalone OpenFAST, while further decoupling may be required if coupled to LES (van Vondelen, Pamososuryo, *et al.* 2024). Further optimization of the optimal azimuth offset, however, is out of the current scope.

To control the loads at the ω_{t} frequency, the following diagonal SISO control structure is designed, as shown in Fig. 3.2 and 3.3:

$$\begin{bmatrix} \beta_{\text{tilt,e}}(s) \\ \beta_{\text{yaw,e}}(s) \end{bmatrix} = \underbrace{\begin{bmatrix} C(s) & 0 \\ 0 & C(s) \end{bmatrix}}_{\mathbf{C}(s)} \begin{bmatrix} M_{\text{tilt,e}}(s) \\ M_{\text{yaw,e}}(s) \end{bmatrix}, \tag{3.15}$$

where $\mathbf{C}(s)$ is shown in Fig. 3.2.

The tuning of PID controllers is done by frequency-domain loop shaping the transfer of the identified model and controller to achieve a certain crossover frequency ω_c:

$$L(s) = G(s)C(s), \tag{3.16}$$

where $L(s)$ is the loop transfer and $G(s)$ is the plant of the system in the Helix coordinate frame. A crossover frequency of $\omega_c = 0.115$ rad/s provided a good trade-off between transient response and sensitivity to noise for the initial controller design. Further adjustments in other controller concepts either increased or decreased this value. Two different types of controllers are implemented in (3.15); an integrator controller and a proportional-integral with low-pass filter (PI-LPF) controller:

$$C_{\text{I}}(s) = \frac{K_{\text{I}}}{s}, \tag{3.17}$$

$$C_{\text{PI-LPF}}(s) = \frac{K_{\text{P}}\omega_{\text{lpf}}(s + K_{\text{I}}/K_{\text{P}})}{s(s + \omega_{\text{lpf}})}, \tag{3.18}$$

where the chosen tuning parameters are provided in Table 3.2 and the resulting Bode plots of the controllers are given in Fig. 3.5.

Since only a bias is corrected, an integral controller (3.17) may already be sufficient as it corrects the steady-state error. Two different gains are examined here to compare different levels of aggressiveness. However, if the error signal contains too rapid changes,

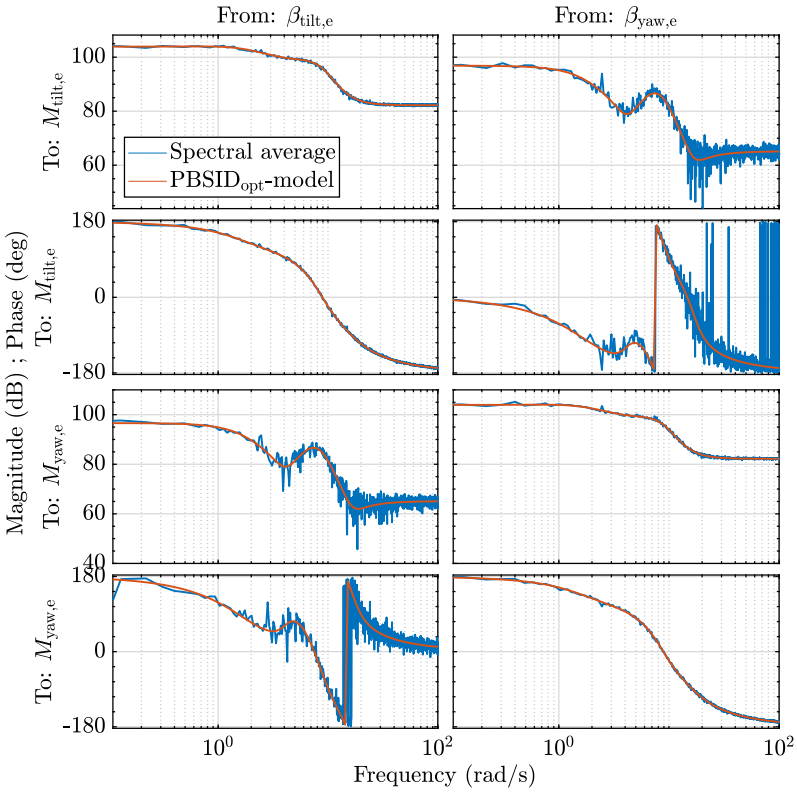

Figure 3.4: Comparison of the PBSID$_{\text{opt}}$-identified model against the spectral averaged input/output data.

Table 3.2: Controller parameters.

Controller	K_{P} [rad/Nm]	K_{I} [rad^2/(Nms)]	ω_{lpf} [rad/s]
C_{I_1}	-	7.9e-10	-
$C_{\text{PI-LPF}_1}$	1.1e-8	1.34e-11	1
$C_{\text{PI-LPF}_2}$	1.1e-8	1.32e-11	0.0718
C_{I_2}	-	1.34e-11	-

possibly due to non-ideal conditions such as turbulence or gusts, a PI controller may respond better to the immediate error. Nevertheless, this may increase actuator costs due to the high-frequency content included in the control action. Thus, a trade-off between smooth control performance and actuator activity may be accommodated by the PI-LPF controller (3.18), which is evaluated here for different combinations between the K_{I}, K_{P}, and ω_{lpf} parameters. The resulting Helix frame loop transfers in the discrete-time domain with zero-order hold discretization method where sampling time $dt = 0.005\,\text{s}$ is

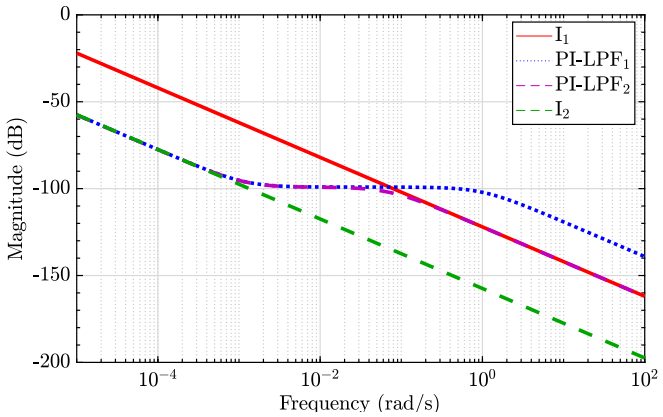

Figure 3.5: Comparison of the Bode plots of the different controller types.

used, is shown in Fig. 3.6.

Note that these controllers are not fully optimized and are selected to study the effect of different controller concepts. More advanced controller synthesis may yield better performance and is the subject of future work. Additionally, no form of anti-windup is present in the PID controllers. However, the integrator term is saturated to prevent it from growing too large.

3.5. SIMULATION SETUP

The effectiveness of the controllers is studied in a high-fidelity simulation environment, where the aero-hydro-servo-elastic wind turbine tool OpenFAST (Fatigue, Aerodynamics, Structures, and Turbulence) (B. Jonkman, Mudafort, *et al.* 2023) is coupled to the high-fidelity fluids solver Adaptive Mesh Refinement (AMR)-Wind to perform coupled LES. This section introduces these codes and presents the simulation settings used in this study.

3.5.1. OPENFAST SIMULATION SETUP

OpenFAST is a multi-fidelity wind turbine simulation tool coupling several standalone modules relating to different aspects of wind turbine simulation, including the structural dynamics, control system, hydrodynamic, and aerodynamics loads. The aerodynamic loads can be computed through computationally efficient engineering models such as the blade element momentum (BEM) theory model or higher-fidelity models such as free-vortex methods or flow solvers like AMR-Wind.

The current work evaluates the proposed controllers on the International Energy Agency's (IEA) 15 MW fixed-bottom reference wind turbine (Gaertner *et al.* 2020). This turbine is controlled using the reference open-source controller (ROSCO) (Abbas, D. Za-

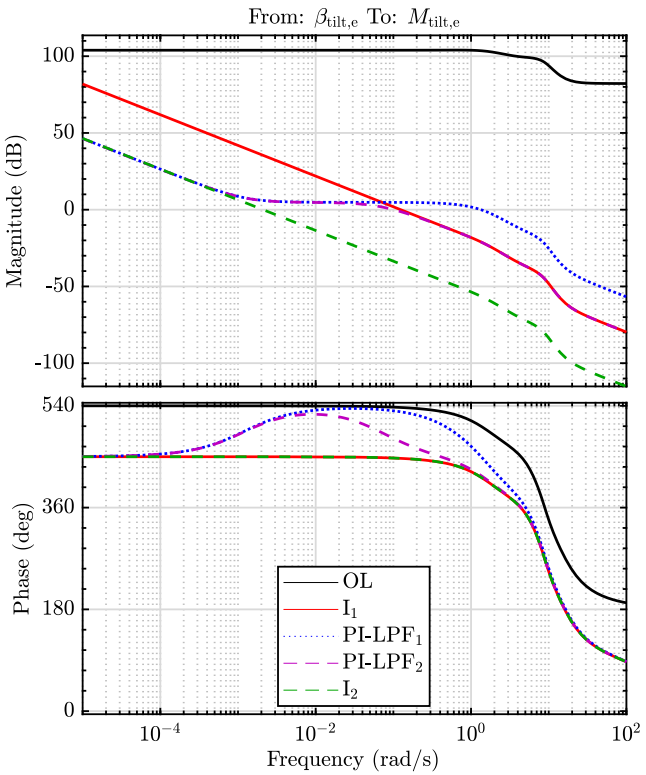

Figure 3.6: Comparison of the different loop transfers, including different controller types. OL denotes the open-loop system.

lkind, *et al.* 2022), which is modified to include the proposed control scheme[2]. Some specifications of this turbine are given in Table 3.3. The OpenFAST model of this turbine is used in this work, whose specifications are consistent with those listed in Table 3.3.

The OpenFAST simulation is coupled to the LES through the actuator line method (ALM) (J. N. Sørensen and Shen 2002), where the turbine blades are represented as lines composed of discrete segments along their span. Each segment is associated with an 'actuator,' which is a mathematical representation of the forces applied by that part of the blade on the fluid. These forces influence the local flow conditions, such as velocity, pressure, and turbulence.

Even though the actuator line method allows more computationally efficient LES, the simulation requires significant resources and runs at a time step of 0.05 seconds, while the OpenFAST simulation runs at a smaller time step of 0.005 seconds where interpolation is performed to facilitate the data exchange. Note that the interpolation in coupled LES introduces phase lags to the controller, which increase the optimal azimuth offset. An additional phase correction may be necessary to fully decouple the pitch control sys-

[2] https://github.com/mvanv/ROSCO/tree/WakeMixingLoadIPC

tem, ensuring optimal controller performance (van Vondelen, Pamososuryo, *et al.* 2024).

Table 3.3: Specifications of the IEA 15 MW reference turbine.

Characteristic	**Value**
Hub height	150 m
Rotor diameter	240 m
Rated power	15 MW
Rated wind speed	10.59 m/s
Cut-in wind speed	3 m/s
Cut-out wind speed	25 m/s
Min. rotor speed	5 rpm
Max. rotor speed	7.56 rpm

3.5.2. AMR-WIND SIMULATION SETUP

AMR-Wind is a parallel adaptive-mesh solver for incompressible flow built on the AMReX library and specifically targeted for wind energy (Brazell *et al.* 2021). The software enables LES of atmospheric boundary layer flows, wind farm turbine-wake interactions, and blade-resolved simulations of multiple turbines within a wind farm and is, therefore, very suited for evaluating controllers that rely on the interaction between wind turbines, such as the controller proposed in this chapter. For details regarding the governing equations and wall models of AMR-Wind, the reader is referred to (Cheung *et al.* 2021).

In this work, and similar to previous work (Taschner, van Vondelen, *et al.* 2023), a Convective Boundary Layer (CNBL) precursor, including Coriolis force effects, is investigated, where the Atmospheric Boundary Layer (ABL) interacts with a stable stratified free atmosphere characterized by a lapse rate of 1 K/km. As recommended in (Allaerts and Meyers 2015), a capping inversion is employed to control the growth and height, where the boundary layer height (h) is set at 1000 m, with a surface roughness (z_0) of 0.0002 m based on offshore measurements in the Netherlands (Taylor and Yelland 2001). The LES used for system identification does not leverage the CNBL but instead uses laminar flow with a wind speed similar to the mean wind speed acting on the downstream turbine in the CNBL simulation, which ensures a cleaner identified model.

For the precursor simulation, the domain size is $x = 5360$ m, $y = 3200$ m, $z = 1600$ m, accommodating three turbines. The isotropic grid size is 10 m, meeting CNBL requirements (Wurps, Steinfeld, and Heinz 2020). Using periodic boundary conditions, the flow evolves for 16 hours, establishing a quasi-stationary turbulent ABL state (Zilitinkevich, Esau, and Baklanov 2007).

Subsequently, during the next 45 minutes, y-z planes are sampled at the inflow ($x = 0$ m) as inflow boundary conditions for turbine simulations. These simulations are enabled through the ALM coupling with OpenFAST.

In the domain, the three turbines are placed at ($x = 1200$ m, $y = 1600$ m), ($x = 2400$ m, $y = 1600$ m), and ($x = 3600$ m, $y = 1600$ m), for turbine 1 (T1), T2, and T3, respectively, accommodating a 5D spacing from the inflow and a 5D spacing between the turbines,

while leaving sufficient space for the wake behind the third turbine to develop. A spacing of 5D corresponds to the distance between the turbines of the Hollandse Kust Noord wind farm in the Netherlands (*Crosswind Hollandse Kust Noord* n.d.), but the spacing of a wind farm can be as small as 3.3-4.3D for the Lillgrund wind farm, resulting in much higher wake losses (Dahlberg 2009). A large spacing is more beneficial for wake recovery but requires more surface area, decreasing energy density. A spacing between 3-7D is usually a trade-off in farm layout design between costs due to wake losses and costs for larger spacing such as cabling and land use. Wake mixing techniques such as the Helix approach could facilitate closer spacings in the future due to faster wake recovery, thereby increasing energy density.

A mesh refinement to 5 m is set surrounding the three turbines in a static box with size $x_m = 5040$ m, $y_m = 960$ m, $z_m = 600$ m starting 4.5D upstream of the first turbine to enable higher resolution flow surrounding the wind turbines. A snapshot for illustration of one LES is given in Fig. 3.7. Note the highly resolved flow showing wake characteristics such as meandering due to the Helix actuation strategy.

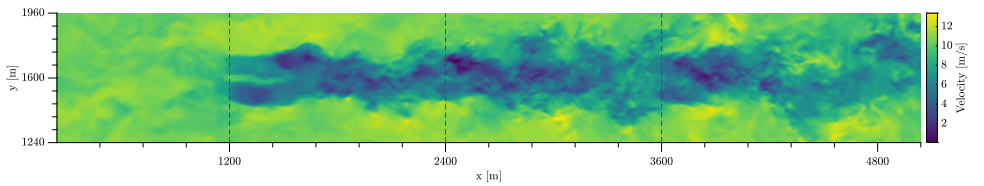

Figure 3.7: Vertical slice of the static box refinement at $t = 59800$ s showing velocity in the x direction for Test Case 6. The turbines are placed at the dashed lines.

Each LES is run on the supercomputer DelftBlue (Delft High Performance Computing Centre 2022) and is run parallelized on 528 processors with 4GB of memory each. The total real-time duration of each simulation is approximately 48 hours.

3.5.3. TEST CASES

To study the effect of the proposed control scheme on the loads and power production, ten coupled LES are performed (Table 3.4). A baseline Helix case is performed where a CCW Helix with 4-degree amplitude and $S_t = 0.25$ is initiated on the first turbine, while the second and third operate with their baseline 'greedy' control strategy. The greedy wind turbine control strategy aims to maximize the immediate power output of a single wind turbine by dynamically adjusting the blade pitch angle and generator torque in real-time. Below the rated wind speed, it increases rotor speed by keeping the blade pitch constant and adjusting the torque, while above the rated wind speed, it maintains optimal rotor speed by increasing the blade pitch to reduce aerodynamic load. This straightforward approach is advantageous for its simplicity and standard in most wind farms. The Helix settings were to match the original settings from (Frederik, Doekemeijer, *et al.* 2020) but may be further optimized as desired. The first four test cases evaluate the rejection control strategy to drive the Helix load to zero using the controllers described in Table 3.2. The next four test cases evaluate the tracking control strategy using the same

controller types, where a reference $\mathbf{M_e^{ref}}$ = 1e4 kNm is set, which is double the value it attains during the baseline case. Note that this reference value is not optimized here to maximize a power/loads trade-off due to the computational cost of LES. However, a single test case with an increased amplitude reference $\mathbf{M_e^{ref}}$ = 1.2e4 kNm is run, which is analyzed in terms of power and loads.

Table 3.4: Overview of the controllers used in each test case.

Case	T1	T2	T3	Ref. [kNm]
BL Helix	CCW Helix	Greedy	Greedy	n.a.
TC1	CCW Helix	I_1-Rej.	Greedy	n.a.
TC2	CCW Helix	PI-LPF$_1$-Rej.	Greedy	n.a.
TC3	CCW Helix	PI-LPF$_2$-Rej.	Greedy	n.a.
TC4	CCW Helix	I_2-Rej.	Greedy	n.a.
TC5	CCW Helix	I_1-Track.	Greedy	1e4
TC6	CCW Helix	PI-LPF$_1$-Track.	Greedy	1e4
TC7	CCW Helix	PI-LPF$_2$-Track.	Greedy	1e4
TC8	CCW Helix	I_2-Track.	Greedy	1e4
TC9	CCW Helix	PI-LPF$_1^+$-Track.	Greedy	1.2e4

3.6. RESULTS: REJECTION SCHEME

This section presents the findings of the investigation into the rejection scheme's performance by evaluation of TC1-TC4, which employ different PID controllers. The analysis encompasses evaluating the controller's rejection performance, assessment of the required pitch actuator actions, and analysis of the damage-equivalent loads (DELs) per industry practice.

3.6.1. ANALYSIS OF CONTROLLER PERFORMANCE

Here, the controller performance is evaluated by investigating the system response in both the frequency and time domain.

Figure 3.8 displays the rotor loads in different reference frames, with M_1 in the rotating frame, M_{tilt} in the fixed frame, and $M_{\text{tilt,e}}$ in the Helix frame[3]. The left column shows the frequency-domain representation of these signals in the form of a power spectrum, while the right column presents low-pass filtered time series data.

The objective of the rejection controller is to drive the Helix load towards zero. In the frequency domain plots, this can be observed by inspecting the Helix load in the different reference frames. Note that the Helix and wind-induced rotor-asymmetric load appear at different locations in the different frames (see Table 3.1). A clear difference is notable between the aggressiveness of the controllers, where the I_2 controller shows

[3]As the conclusions drawn from the results of the orthogonal channels (yaw, yaw$_e$) and blade 2 and 3 are similar, they are omitted in the remainder of this chapter for conciseness but available upon request.

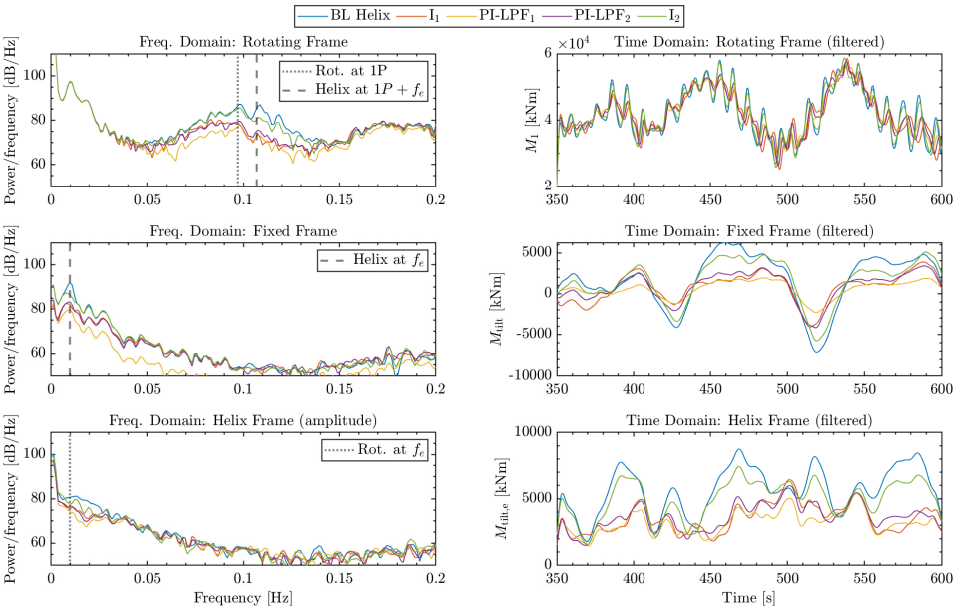

Figure 3.8: Comparison of the blade loads of T2 in different reference frames in the frequency and time domains. The left column shows the frequency-domain representation of these signals, highlighting the reduction in Helix load and wind-induced rotor asymmetric load in the Helix frame due to the rejection controllers. The right column presents low-pass filtered time series data, indicating the successful driving of the bias in $M_{\text{tilt,e}}$ towards zero for most controllers.

much less attenuation compared to, e.g., the I_1 controller. However, all controllers are able to reduce the Helix load significantly compared to the baseline case.

In the time domain, this difference in aggressiveness becomes clear as well, where it can be seen that most controllers successfully drive the bias in $M_{\text{tilt,e}}$, which is present in the baseline case, towards zero. In contrast, the I_2 controller only appears to do so to a slight extent.

Interestingly, the wind-induced rotor asymmetric load, which is present in the baseline case, appears to be reduced by the proposed controllers as well, benefiting the fatigue life even more. Note that the less aggressive I_2 controller does not attenuate this load. This observation is also clearly visible in the rotating frame, where this load appears at the $1P$ frequency.

To further understand the reason why some controllers correct the wind-induced rotor asymmetric load as well, the sensitivity function of the $\beta_{\text{tilt,e}}$ to $M_{\text{tilt,e}}$ transfer in the Helix frame is studied in Fig. 3.9. The sensitivity function is given by:

$$\frac{1}{1+G(s)C(s)}, \tag{3.19}$$

This function provides insights into the controller's effectiveness across various frequencies. The objective is to maintain a consistent gain of 0dB across all frequencies while attenuating the DC gain, where the Helix load acts in the Helix coordinate frame. In this figure, it becomes evident that the controllers adeptly mitigate lower frequencies, aligning with the desired behavior. However, a closer observation reveals that the I_1-, PI-LPF_1, and PI-LPF_2-controllers introduce some attenuation to f_e, which explains the behavior of these controllers in reducing the wind-induced rotor asymmetric load.

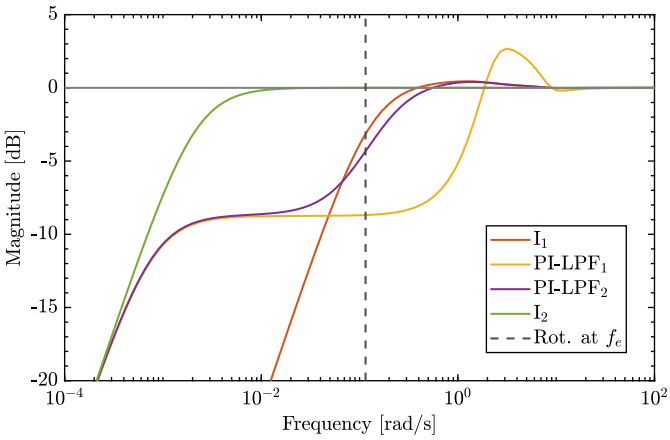

Figure 3.9: Sensitivity function of the rejection controller.

It should be noted that the control settings and tuning significantly impact the controller's performance. For example, if a large Strouhal number is selected, the wind-induced rotor asymmetric load is at a significantly higher frequency in the Helix frame, which might not be attenuated by any of the current controllers. Or, if different gains are chosen, the region of attenuation may become smaller or larger. Therefore, if the objective is to reduce both the wind-induced rotor asymmetric load and Helix load, a careful methodology should be followed to ensure both are mitigated as desired. Possibly more advanced H_2- or H_∞-control could provide more effective solutions (see e.g. (Skogestad and Postlethwaite 2005)).

In summary, the load rejection scheme effectively mitigates the Helix load present in the baseline case in most control setups while also attenuating the wind-induced rotor asymmetric load in the most aggressive controllers, as demonstrated by both time and frequency domain analyses. These results show promising indications for enhancing the fatigue life of the downstream turbine, which is further analyzed in the next section by quantifying the DELs and pitch bearing damage (PBD).

3.6.2. IMPACT ON POWER PRODUCTION, DELS, AND PBD

This section quantifies the improvement of the fatigue life of T2 and T3 due to the proposed controller by computation of the DELs and comparison against the baseline Helix case. This metric allows a comparison of the degree of loading a turbine encounters

during the simulation and complies with the industry convention according to the IEC-61400 standard (International Electrotechnical Commission 2019). It further relies on the rainflow counting algorithm and is computed through the following formula:

$$\mathrm{DEL} = \left(\frac{\sum_{i=1}^{N} (A_i)^m n_i}{n_{eq}} \right)^{\frac{1}{m}}, \tag{3.20}$$

where N is the total count of cycles, m is the inverse Wöhler slope, conventionally taken as 5 for steel tower components and 10 for composite blade structures. Moreover, n_i indicates the number of cycles represented by a range of A_i, and n_{eq} denotes the equivalent cycle, set to 1 here.

The first 350 seconds of the dataset are discarded to account for the propagation of the wake from the upstream to the downstream turbine and other transient effects in the simulation. A total of 2150 seconds of simulation time are used in the DEL calculations.

Figures 3.10b and 3.10c show the results of the DEL calculations, where the DEL of the controllers is displayed relative to the baseline Helix case. It is evident from the bar graph that there are significant disparities in the reduction in loads between the different controllers. All controllers show a substantial decrease in DEL. However, this reduction does not come without costs, as the I_1-controller causes a notable reduction in power, and others also see a slight power decrease (Fig. 3.10a and Table 3.5). The I_2 and PI-LPF$_1$ appear to strike the best balance between load reduction and power production preservation.

Table 3.5: Overview of the power gains under the different controllers.

Controller	**T2 [MW]**	**T3 [MW]**	**T2+T3 [MW]**
I_1-rejection	6.93 (-1.83%)	6.77 (-1.27%)	13.71 (-1.56%)
PI-LPF$_1$-rejection	6.99 (-1.06%)	6.88 (+0.23%)	13.86 (-0.42%)
PI-LPF$_2$-rejection	6.97 (-1.30%)	6.84 (-0.28%)	13.81 (-0.80%)
I_2-rejection	7.03 (-0.54%)	6.85 (-0.20%)	13.87 (-0.37%)

Interestingly, also the third turbine experiences substantial load reductions for most controllers. Even for the case where the third turbine experiences a small power gain, with the PI-LPF$_1$ controller, there is a load reduction visible on the third turbine, while usually, an increase in power is associated with a DEL increase.

Another metric used to study fatigue is pitch bearing damage (PBD). This is damage that builds up in the pitch actuators over time and can be understood as the cost of the control action that is required to achieve the control objective. The formula is given by (van Vondelen, Navalkar, Kerssemakers, *et al.* 2023):

$$\mathrm{PBD}(\gamma) = \sum_{k=1}^{N} \delta\theta(k) (\max(\cos(\gamma) M_{\mathrm{flap}}(k) + \sin(\gamma) M_{\mathrm{edge}}(k), 0))^m, \tag{3.21}$$

where γ is the radial position of the bearing, $\delta\theta$ is the pitch difference, M_{flap} is the flapwise blade root moment, M_{edge} is the edgewise blade root moment, and m is the inverse Wöhler slope. Here, only the radial position with the largest damage is examined.

The computed PBDs are displayed in Table 3.6, which are compared against the PBD of T1. It can be observed that the PBD of T1 is very high compared to the PBD of T2, employing the rejection controllers while actuating with similar pitch amplitude and frequency. The strong difference in wind speed increasing the blade root moment on T1 plays a role here, but another important cause is the reduction in the blade root moment on T2 as a result of the I_1-rejection controller. Observe in (3.21) that it is a function of the blade root moments. Even though significant pitch action is required, a reduction of blade root moment prevents a substantial increase in PBD on T2, significantly alleviating PBD concerns regarding the implementation of this method.

Table 3.6: Overview of the PBDs under the different controllers.

Turbine	**Controller**	**PBD** ($\times 1e^{17}$) **[kNm^3 deg]**
T1	BL Helix	20.17
T2	I_1-rejection	0.78
	PI-LPF$_1$-rejection	1.76
	PI-LPF$_2$-rejection	0.63
	I_2-rejection	0.52

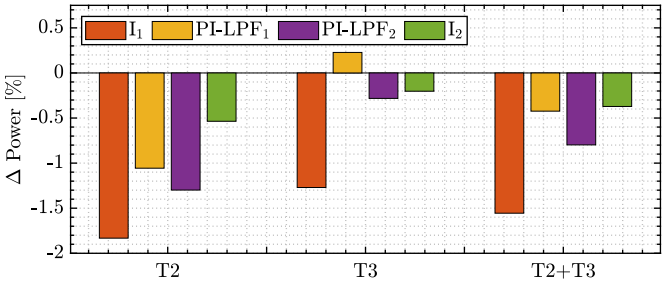

(a) Bar chart of the power difference relative to the baseline Helix case for both T2, T3, and combined.

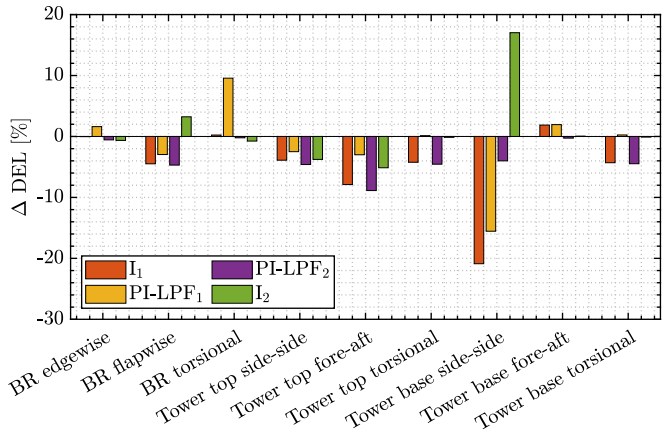

(b) Bar chart of the damage-equivalent loads of the rejection controllers relative to the baseline Helix case for T2. 'BR' denotes blade root.

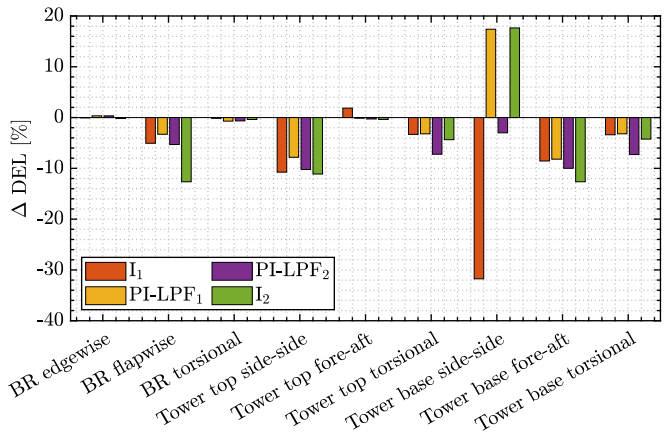

(c) Bar chart of the damage-equivalent loads of the rejection controllers relative to the baseline Helix case for T3. 'BR' denotes blade root.

Figure 3.10: Performance plots of the rejection controllers.

3.6.3. A NOTE ON LIFETIME FATIGUE

While the above analyses allow comparison between the different control approaches, they do not provide a complete picture of the impact on turbine fatigue life. To properly assess this, a comprehensive loads study is required, evaluating all load cases as specified in IEC-61400-1. Only the manufacturer possesses the necessary detailed knowledge, including design specifics, material properties, and operational data, to accurately evaluate the impact on fatigue life.

Moreover, since these controllers are active only in specific scenarios (i.e., in a periodic wake), they can only be evaluated accurately using high-fidelity codes such as LES. These simulations are costly compared to conventional BEM codes used for load calculations. Hence, this study refrains from quantitatively assessing the impact on turbine fatigue lifetime.

A qualitative assessment for the baseline Helix case shows that, assuming 17% activation time (based on a study on the Hollandse Kust Noord wind farm (Kerssemakers 2022)), the impact on lifetime fatigue for various load channels is shown in Table 3.7. This assumes Design Load Case (DLC) 1.2 accounts for 75% of operational time, with other DLCs (2.1, 2.4, 3.1, 4.1, 6.4) covering the remaining 8% (Fig. 3.11).

Table 3.7: Overview of the impact on lifetime fatigue for baseline Helix.

Channel	**Lifetime fatigue increase**
Blade root edgewise	+0.6%
Blade root flapwise	+1.3%
Tower top side-side	+0%
Tower top fore-aft	+9.4%
Tower top torsional	+4.7%
Tower base side-side	+0.1%
Tower base fore-aft	+0.8%
Pitch bearing	+92.9%

Note the relatively strong increase in pitch bearing lifetime fatigue. This implies the pitch bearing must be replaced twice as often during the turbine lifetime compared to the baseline. Eventually, pitch bearings should be designed, taking fatigue due to wake mixing control into account, which is currently not the case.

Comparing pitch bearing damages between the upstream turbine and proposed downstream controllers (Table 3.6), the downstream approach shows significantly lower pitch bearing damage, implying only a slight overall increase compared to the upstream-only method.

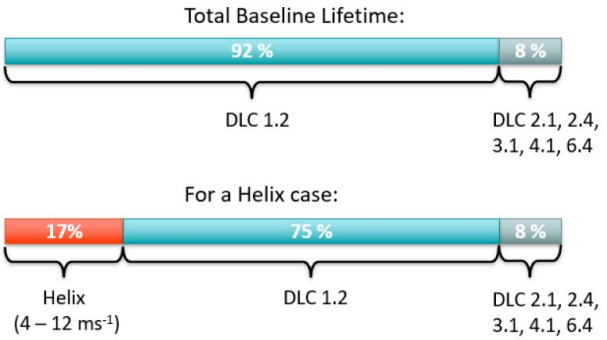

Figure 3.11: Comparison between the division of DLCs of the baseline greedy versus baseline Helix case in Kerssemakers 2022.

3.7. RESULTS: TRACKING SCHEME

After discussion of the results of the rejection scheme, this section now presents the results obtained when toggling the other objective—synchronized wake mixing for power enhancement, which is achieved by tracking a reference. Here, TC5 - TC9 are evaluated and compared, where the tracking performance of the controller, DELs, and PBD are analyzed. Also, some flow analysis is presented and reviewed.

3.7.1. ANALYSIS OF CONTROLLER PERFORMANCE

This section examines the controller performance by performing time and frequency domain investigations of the system's response and control commands.

Figure 3.12 displays the rotor loads in different reference frames, with M_1 in the rotating frame, M_{tilt} in the fixed frame, and $\mathbf{M}_\text{e}$ in the Helix frame. Rather than analyzing $M_{\text{tilt,e}}$ and $M_{\text{yaw,e}}$, the control performance is better understood when inspecting the amplitude $\mathbf{M}_\text{e}$ since the phase ϕ_e of $M_{\text{tilt,e}}$ and $M_{\text{yaw,e}}$ might change over time. This influences the resulting reference to $M_{\text{tilt,e}}$ and $M_{\text{yaw,e}}$ and makes drawing conclusions in the time domain more challenging. The left column shows the frequency domain representation of these signals in the form of a power spectrum, while the right column presents low-pass filtered time series data.

The objective of the tracking controller is to correct the bias to the reference $\mathbf{M}_\text{e}^\text{ref}$, essentially amplifying the Helix frequency. This amplification can be observed in the frequency domain, where the characteristic peak has increased in the rotating and fixed coordinate frame. In the time domain, an interesting observation of the phase synchronization capabilities can be made, where it appears in the fixed frame in Fig. 3.12 that the aggressive I_1 controller is not able to match the phase with the baseline Helix case's phase. This implies it does not fully leverage the already present content and needs to compensate to force a different phase in the response, requiring more pitch action.

The PI-LPF$_1$-controller, while synchronizing the phase, has a rather noisy pitch signal, which can be seen from Fig. 3.13, which depicts the pitch rate. A noisy pitch signal impacts loads on the structure and damages the pitch bearing. Ultimately, the PI-LPF$_2$-

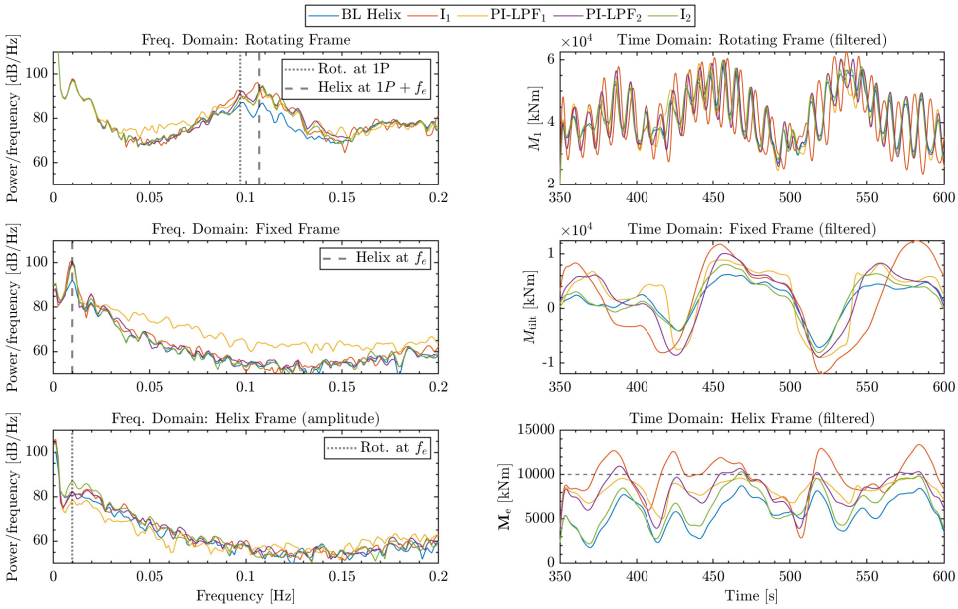

Figure 3.12: Comparison of the blade loads of T2 in different reference frames in the frequency and time domains. The left column shows the frequency-domain representation of these signals, illustrating the amplification of the Helix frequency due to the tracking controllers. The right column presents low-pass filtered time series data, indicating the phase synchronization capabilities of the controllers. The reference in the lower right plot is indicated by the horizontal dashed line.

controller may be considered to show a compromise between the aggressiveness of the I_1-controller and the desired control behavior, as shown by the PI-LPF$_1$-controller. Akin to the PI-LPF$_1$-controller, it can synchronize but does not exercise a high-frequent pitch signal, making it a suitable candidate for the phase-synchronization objective. A target sensitivity Bode plot could be established, demonstrating the suitability of this approach for H_2/H_∞ controller synthesis. The next section quantifies the DELs and PBDs and studies the power production of the test cases.

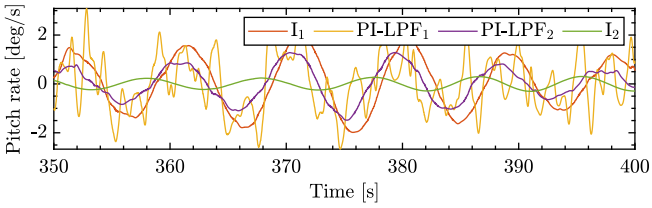

Figure 3.13: Comparison of the pitch rate.

3.7.2. IMPACT ON POWER PRODUCTION, DELS, AND PBD

Here, the impact on the fatigue life, pitch bearing, and power production is studied. Also, an additional test case, namely PI-LPF$_1^+$, is examined, in which an increased reference $\mathbf{M}_\mathbf{e}^{\text{ref}}$ is used. Since the objective is phase synchronization for power enhancement, first, the power production of each control case is investigated in Fig. 3.14a. The I_1-tracking controller appears to cause a significant power loss on T2, which may be caused by the inability to fully exploit the periodic wake such that phase synchronization could not always be attained. However, a power increase is observable at T3 as a result of the tracking controller on T2, although it is insufficient to increase the aggregate power capture of both turbines.

Interestingly, a slight power gain can be observed on T2 when employing the other controllers, which suggests that baseline greedy control is potentially not optimal for power extraction when a turbine is in a Helix wake, however, more investigation is required to confirm this. Even more striking is the fact that, due to phase synchronization, the wake mixing is continued further downstream and significantly benefits T3 as a significant power gain of 4.39% could be attained for the PI-LPF$_1$-controller, resulting in a 2.3% overall power gain underlining the potential of phase synchronized wake mixing. Similarly, the PI-LPF$_2$ controller shows a power increase, with a considerable power gain of 3.98% on T3, while increasing the total power with 2.01%. The best-performing controller PI-LPF$_1$ was tested with an extended reference referred to as the case PI-LPF$_1^+$, where an even more prominent power increase of 5.96% could be observed on T3 and a collective increase of 2.96%. An overview of the power production for each controller is given in Table 3.8.

Table 3.8: Overview of the power gains under the different controllers.

Controller	**T2 [MW]**	**T3 [MW]**	**T2+T3 [MW]**
I_1-tracking	6.81 (-3.58%)	6.89 (+0.50%)	13.70 (-1.57%)
PI-LPF$_1$-tracking	7.08 (+0.26%)	7.16 (+4.39%)	14.24 (+2.30%)
PI-LPF$_2$-tracking	7.07 (+0.09%)	7.13 (+3.98%)	14.20 (+2.01%)
I_2-tracking	7.07 (+0.17%)	6.96 (+1.43%)	14.03 (+0.79%)
PI-LPF$_1^+$-tracking	7.07 (+0.05%)	7.27 (+5.96%)	14.34 (+2.96%)

Next, an analysis is made of the DEL increase for all cases relative to baseline in Fig. 3.14b for T2 and Fig. 3.14c for T3. From Fig. 3.14b, it can be concluded that all cases increase the DELs on T2, while the strongest increase is in the I_1-tracking case. For example, the strong increase in DEL on the blade root flapwise moment for the I_1-tracking controller is due to the stronger amplification, while the increases of the PI-LPF$_1$-controller are due to the large variations in the pitch actuation, where higher frequent noise propagates to the turbine structure and increases the fatigue damage. In the case of T3, there are no clear trends visible. Generally, when the wind speed is higher due to wake mixing, a slight load increase may be expected on T3, this is, however, not yet conclusive and would require more extensive load studies, e.g. by averaging results from various turbulence realizations (International Electrotechnical Commission 2019). In summary, the PI-LPF$_1$-, PI-LPF$_2$, or I_2-tracking controllers appear to be the

best-performing scheme in terms of DEL.

Furthermore, the PBDs of the different control schemes are presented in Table 3.9. Here, the earlier hypothesis is confirmed. The highest PBD is found for the I_1-controller, which requires more pitching to track the reference as it does not seem to fully exploit the periodic content already present in the wake. In the PI-LPF_1-tracking case, the resulting PBD is slightly higher due to more extensive pitch variations and impacts the fatigue life of the bearing more than the other remaining cases. The I_2 controller exhibits the lowest PBD, as it is the least aggressive controller. The reason for a high PBD for the PI-LPF_1^+ case is due to the extended $\mathbf{M_e^{ref}}$ value, although it is still very reasonable.

Table 3.9: Overview of the PBDs under the different controllers.

Turbine	**Controller**	**PBD** ($\times 1e^{17}$) **[kNm^3 deg]**
T1	BL Helix	20.17
T2	I_1-tracking	2.23
	PI-LPF_1-tracking	1.88
	PI-LPF_2-tracking	1.36
	I_2-tracking	1.09
	PI-LPF_1^+-tracking	2.28

Finally, the vertical profile of the mean streamwise velocity in the wake of T2 is analyzed in this section. Figure 3.15 showcases these results, where a comparison is made against the baseline case across several rotor diameters behind T2 up to T3 for only the I_1 and PI-LPF_2 controller (for clarity's sake). The wake recovery of the I_1 appears similar in the first few rotor diameters behind T1 ($x/D = 6$ and $x/D = 7$). However, at $x/D = 10$, PI-LPF_2 has much better wake recovery above the hub, translating to the power increase observed at T3 shown in Fig. 3.14a.

The PI-LPF_2-tracking controller appears superior to the I_1 case, which explains the strong performance gain on T3 compared to the other methods.

3.8. CONCLUSION

This study examined downstream turbine control in a Helix wake, proposing two strategies: load rejection and phase synchronization. A novel extension of the multi-blade coordinate transformation was proposed, enabling the use of linear PID controllers to execute both strategies. Computational simulations incorporating three turbines demonstrated promising results for the selected cases: load rejection improved turbine fatigue life by up to 10%, while phase synchronization led to a 6% power gain on T3 compared to the baseline Helix setup. As inferred in Section 3.6.3, a more comprehensive turbine fatigue life assessment is beyond the scope of this study and, thus, subject to future work. Further optimization and exploration of advanced control strategies employing this coordinate transformation are recommended, as further power improvements are expected.

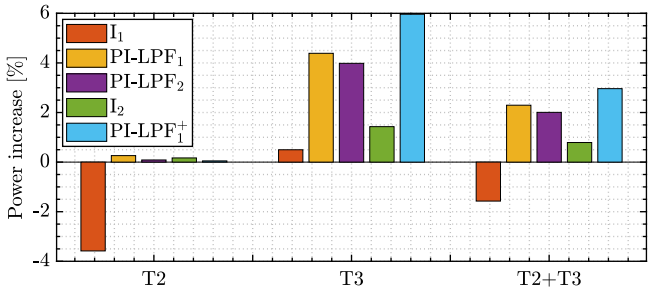

(a) Bar chart of the power increase relative to the baseline Helix case for both T2, T3, and combined.

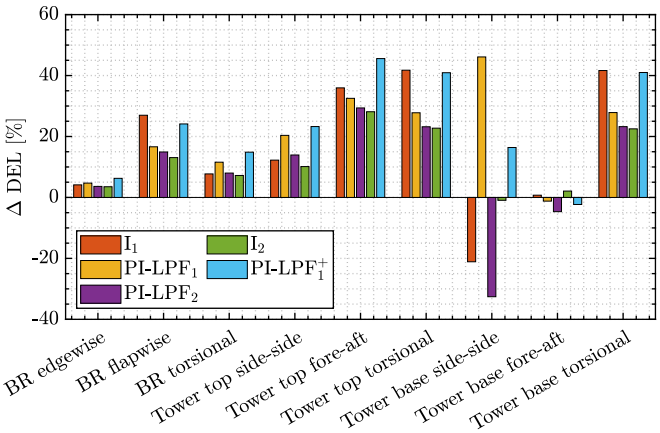

(b) Bar chart of the DEL increase relative to the baseline Helix case for T2 for the different controllers.

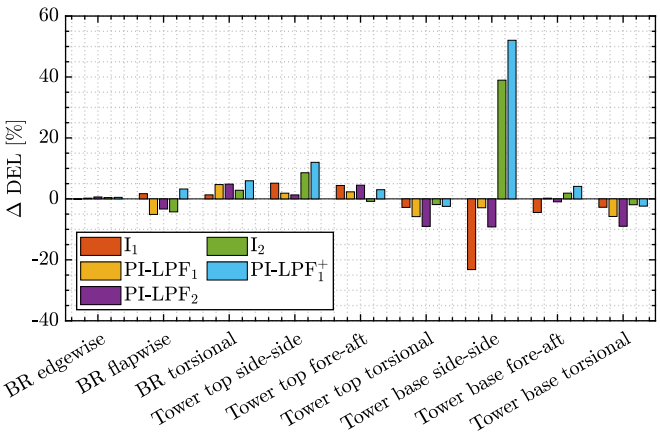

(c) Bar chart of the DEL increase relative to the baseline Helix case for T3 for the different controllers.

Figure 3.14: Performance plots of the tracking controllers.

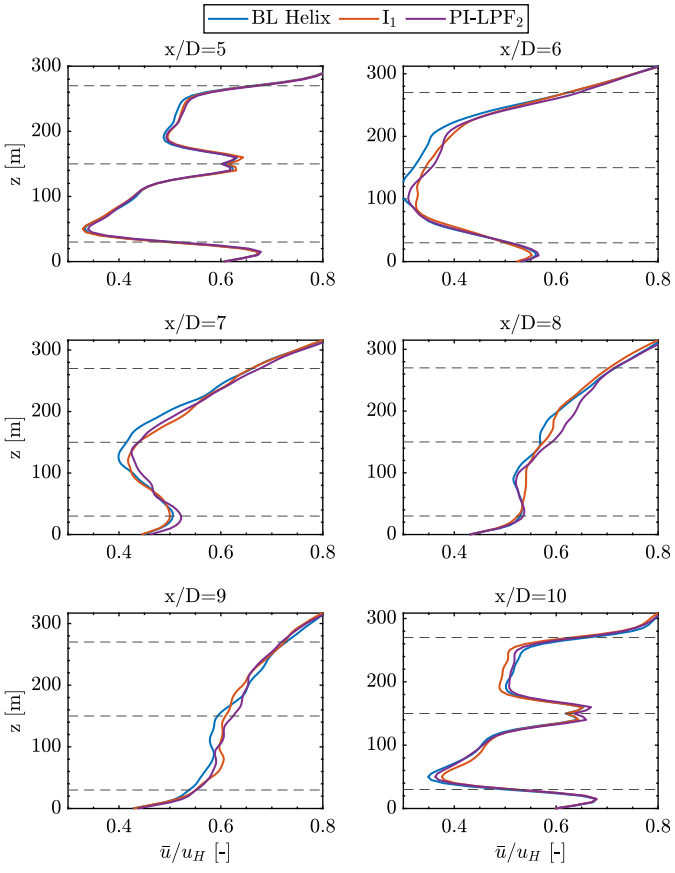

Figure 3.15: Vertical profile of the mean streamwise velocity of the wake behind T2 for several rotor distances D behind T2 ($x/D = 5$) for the tracking controllers. The dashed horizontal lines indicate the rotor top, hub, and bottom. T3 is located at $x/D = 10$.

4

LINEAR KALMAN FILTER FOR SYNCHRONIZED WAKE MIXING

Wakes of upstream turbines impinge on downstream turbines in wind farms, causing power losses and increased fatigue. Wind farm control methods, such as the Helix approach, have been proposed to actively stimulate mixing of the wake with the free stream by pitching the blades dynamically. As a result, a periodic structure is forced in the wake, which increases average downstream wind velocity and thereby improves downstream turbines' power production. However, downstream turbines could further exploit this periodic wake structure by pitching dynamically as well, but in sync with the phase of the incoming wake structure. Depending on the phase offset between the impinging wake and the downstream pitch, this creates destructive or constructive interference between the two wakes and further improves power production downstream. This work presents and experimentally validates such a control strategy for downstream wind turbines and evaluates it on a three-turbine wind farm in an experimental wind tunnel setting using scaled wind turbines. Results validate the controller's effectiveness and show that the third turbine's performance improvement is strongly influenced by the phase offset between the periodic wake components generated by the second turbine and those present in the upstream wake.

This chapter is based on previously published work:

van Vondelen, A. A. W., Ottenheym, J., Pamososuryo, A. K., Navalkar, S. T., and van Wingerden, J. W. (2023). "Phase Synchronization for Helix Enhanced Wake Mixing in Downstream Wind Turbines". In: *IFAC-PapersOnLine* 56.2. 22nd IFAC World Congress, pp. 8426–8431. DOI: 10.1016/j.ifacol.2023.10.1039

van Vondelen, A. A. W., van der Hoek, D. C., Navalkar, S. T., and van Wingerden, J. W. (2025). "Experimental validation of synchronized Helix wake mixing control". In: *Renewable Energy*, p. 124768. ISSN: 0960-1481. DOI: https://doi.org/10.1016/j.renene.2025.124768

Contents

4.1. INTRODUCTION

Wind energy serves as one of the main drivers towards the realization of a sustainable society. To reduce its cost, turbines are typically grouped in farms, allowing cabling, maintenance, and installation costs to be shared. The layout of such a farm primarily depends on the dominant wind directions (Baricchio, Gebraad, and van Wingerden 2024). Turbines are positioned so that their wakes minimally interact with downstream turbines, since such interactions significantly reduce performance and increase structural loading (R. J. Stevens and Meneveau 2017).

Situations in which turbines are waked occur relatively often (González-Longatt, Wall, and Terzija 2012). Studies show that the power production decrease of offshore wind farms can be as high as 20%, with structural loading increasing similarly (Barthelmie *et al.* 2009). This indicates significant potential for wind farm control strategies that mitigate wake effects. Optimizing production and balancing loads at the farm level have received growing attention in recent years, where some turbines deviate from their individual optimum to benefit downstream turbines and enhance overall farm performance (Meyers, C. Bottasso, *et al.* 2022).

One elementary control method involves derating upstream turbines to preserve energy for downstream turbines (Annoni, Gebraad, *et al.* 2016). Although not significantly enhancing performance, it may be used to distribute loads more evenly across turbines (van der Hoek, Kanev, *et al.* 2019). Wake steering appears more promising for performance increase and is already being adopted in state-of-the-art wind farms due to its simplicity and demonstrated Annual Energy Production (AEP) gains (Baricchio, Gebraad, and van Wingerden 2024; Fleming, Gebraad, *et al.* 2014; Siemens Gamesa 2019).

Another category of wind farm controllers promotes wake mixing with the surrounding ('free stream') wind field by dynamically manipulating the flow. Known as Dynamic Induction Control (DIC), this method collectively pitches blades sinusoidally to change the induction factor (Goit and Meyers 2015). This causes flow immediately behind the turbine to mix effectively due to speed differences. This method, referred to as the 'Pulse', shows promising results in simulations, with higher pitch amplitudes yielding higher power gains. However, dynamic actuation increases fatigue loads, increasingly with pitch amplitude, especially on the tower and blades (Frederik and van Wingerden 2022).

Dynamic Individual Pitch Control (DIPC) is a recent alternative to DIC (Frederik, Doekemeijer, *et al.* 2020). Unlike collective blade actuation, DIPC applies a 120° phase shift to the actuation of each blade. This repositioning of the effective thrust center creates a helical wake shape, thus referred to as the 'Helix' approach (Frederik, Doekemeijer, *et al.* 2020).

The rotational direction of the Helix influences power gain, with counterclockwise (CCW) rotation typically superior to clockwise (CW) rotation (Frederik, Doekemeijer, *et al.* 2020; van der Hoek, Van den Abbeele, *et al.* 2024). The Helix approach reduces thrust variations compared to the Pulse, adjusting only the thrust position rather than its magnitude. While blades experience slightly increased loads compared to the Pulse, tower loads significantly decrease (Frederik and van Wingerden 2022). Higher pitch amplitudes generally enhance performance but increase loads, especially on the pitch bearing (Taschner, van Vondelen, *et al.* 2023; van Vondelen, Navalkar, Kerssemakers, *et al.*

2023).

The Helix approach enhances wake mixing by applying periodic tilt and yaw moments upstream, introducing periodic wake structures (Frederik and van Wingerden 2022; Taschner, van Vondelen, *et al.* 2023). These structures improve downstream turbine performance, but also introduce a periodic load downstream due to interaction with the impinging wake. Yet downstream turbines are operated without awareness of this periodicity induced upstream, which could either be regulated to reduce loads or enhanced to propagate the Helix wake further downstream. Our recent work first investigated feedback control for downstream turbines within a Helix wake to mitigate or reinforce this load, validated in large-eddy simulations (LES) (van Vondelen, Pamososuryo, *et al.* 2025).

Although LES provides valuable insights, it remains computationally intensive and sensitive to various modeling choices (Meyers, C. Bottasso, *et al.* 2022). Lower-fidelity models reduce cost but introduce additional simplifications (R. J. Stevens and Meneveau 2017). Practical challenges such as sensor noise and actuator limitations are typically not captured, motivating experimental validation under realistic conditions.

The potential of actively controlling downstream turbines in response to periodic wakes is largely unexplored. Earlier work indicates that the relative phase between downstream control inputs and periodic wakes strongly influences power production (Korb, Asmuth, and Ivanell 2023). Aligning the up- and downstream wakes at any phase shift requires phase estimation techniques, as developed previously (van Vondelen, Ottenheym, Pamososuryo, *et al.* 2023). This is different compared to the approach developed in (van Vondelen, Pamososuryo, *et al.* 2025), which only allows load rejection or amplification.

Kalman filters effectively handle noise and provide unbiased estimates. Earlier work applied linear Kalman filters for wind speed estimation (Simley and Pao 2016), whereas others employed an extended Kalman filter (EKF) for nonlinearities (Knudsen, Bak, and Soltani 2011). The linear approach requires multiple models for different conditions, whereas the EKF accommodates nonlinearities but introduces complexity. Typically, the wind speed is modeled as a random walk. However, this is generally not suited to estimating periodic wake dynamics (van Vondelen, Ottenheym, Pamososuryo, *et al.* 2023).

Earlier work successfully explored an EKF synchronization approach for turbulent wake estimation, showing power improvements using nonlinear estimation in complex LES (van Vondelen, Coquelet, *et al.* 2025). Moving beyond numerical validation, this study conducts the first experimental implementation in a controlled wind tunnel environment. Wind tunnel experiments provide high repeatability and precise inflow control, essential to validate estimator performance and synchronization impacts under realistic constraints.

A practical limitation is that the experimental setup lacks blade load sensors required for complex modeling approaches like blade element models (van Vondelen, Coquelet, *et al.* 2025). Thus, a linear Kalman Filter relying solely on available strain measurements is adopted (van Vondelen, Ottenheym, Pamososuryo, *et al.* 2023). While less general, this approach is robust and computationally efficient for wind tunnel conditions.

Wind tunnels have validated wind farm control strategies effectively. Wake steering and closed-loop control have been demonstrated at Politecnico di Milano (Mancini,

Schreiber, and C. A. Bottasso 2023; Schreiber and C. A. Bottasso 2022), while DIC and Helix control have been demonstrated at TU Delft (van der Hoek, Frederik, *et al.* 2022; van der Hoek, Van den Abbeele, *et al.* 2024). Prior work attempted initial DIC wake alignment experiments without synchronization (van Vondelen, van der Hoek, *et al.* 2024). Experimental synchronization logically follows, bridging simulations and full-scale experiments.

This paper builds upon earlier theoretical and simulation studies (van Vondelen, Coquelet, *et al.* 2025; van Vondelen, Ottenheym, Pamososuryo, *et al.* 2023), addressing the gap by experimentally validating synchronization in a scaled wind farm. The linear Kalman filter is adapted from previous frameworks (van Vondelen, Ottenheym, Pamososuryo, *et al.* 2023) for the wind tunnel setting. Unlike prior studies, this paper develops practical estimator–controller integration, evaluates model accuracy, estimator repeatability, and quantifies phase offset impacts on performance, bridging theory and practical application.

The main contributions are:

1. **First experimental validation of synchronization:** Synchronization is validated within a three-turbine wind farm setup. The experiment assesses the ability of the downstream turbine to estimate the upstream wake phase and synchronize its control action.

2. **Adaptation of the synchronization control scheme:** Building upon the general synchronization framework proposed by (van Vondelen, Ottenheym, Pamososuryo, *et al.* 2023), this study extends the method for integration with the wind turbine pitch control system.

3. **Quantification of optimal phase offset:** We identify the phase offset setting that maximizes power production at the third turbine. This provides valuable insights into the relationship between phase synchronization and downstream energy production.

The remainder of this paper is structured as follows. Section 4.2 revisits the theoretical framework for phase estimation using an augmented Kalman filter, and describes its integration with the wind turbine control system. Section 4.3 outlines the experimental setup used to evaluate the proposed scheme. System identification and estimator tuning are presented in Section 4.4, and the results are analyzed in Section 4.5. The paper concludes with a summary and recommendations in Section 4.6.

4.2. ESTIMATION AND CONTROL FRAMEWORK

This section first revisits the estimation framework introduced in (van Vondelen, Ottenheym, Pamososuryo, *et al.* 2023), where a state-space model is augmented to include periodic inputs as additional states, enabling joint estimation of system states and periodic disturbances via a Kalman filter. The framework is then extended and connected to the wind turbine actuation system to enable real-time synchronization with the incoming periodic wake.

4.2.1. DERIVING THE AUGMENTED STATE-SPACE MODEL

To enable synchronization of the downstream turbine with the periodic wake-induced loading, it is necessary to estimate the phase and amplitude[1] of this disturbance in real time. However, the wake signal is not directly measurable. The strategy adopted here is to model the periodic wake forcing as a virtual input with known frequency but unknown amplitude and phase. By embedding this signal into the state-space system as an augmented state, its parameters can be estimated alongside the physical states using a Kalman filter. The derivation below formalizes this estimation structure.

A linear time-invariant (LTI) system with n states, r inputs, and m outputs is assumed:

$$\dot{x}(t) = Ax(t) + Bu(t), \tag{4.1}$$

$$y(t) = Cx(t) + Du(t), \tag{4.2}$$

where $x(t) \in \mathbb{R}^n$ denotes the state vector, $u(t) \in \mathbb{R}^r$ the input vector, $y(t) \in \mathbb{R}^m$ the output vector, and $\{A, B, C, D\}$ the system matrices of appropriate dimensions.

The state-space model described here represents the downstream turbine (T2), which uses wake estimation to synchronize its actuation. Although wind turbine dynamics are inherently nonlinear, the LTI assumption is considered acceptable in this context. This is because the experiments are conducted around a fixed operating point (constant wind speed and mean pitch angle), and the periodic forcing is performed at a single frequency. As such, the LTI model provides a sufficiently accurate approximation for use within the Kalman filter framework during these controlled wind tunnel experiments.

The inputs $u(t)$ are partitioned into controllable inputs $u^{\mathrm{c}}(t) \in \mathbb{R}^{r_c}$ and uncontrollable inputs $u^{\mathrm{u}}(t) \in \mathbb{R}^{r_u}$ such that $r = r_c + r_u$:

$$u(t) = \begin{bmatrix} u^{\mathrm{c}}(t) \\ u^{\mathrm{u}}(t) \end{bmatrix} + \begin{bmatrix} w^{\mathrm{c}}(t) \\ 0 \end{bmatrix}, \tag{4.3}$$

where $w^{\mathrm{c}}(t) \in \mathbb{R}^{r_c}$ is an input disturbance. Similarly, the input and feedthrough matrices are partitioned as:

$$B = \begin{bmatrix} B^{\mathrm{c}} & B^{\mathrm{u}} \end{bmatrix}, \quad D = \begin{bmatrix} D^{\mathrm{c}} & D^{\mathrm{u}} \end{bmatrix}. \tag{4.4}$$

The uncontrollable input $u^{\mathrm{u}}(t)$ primarily represents the environmental disturbances acting on the turbine, consisting mainly of the periodic component of the wake $u^{\mathrm{p}}(t) \in \mathbb{R}$, modeled as:

$$u^{\mathrm{p}}(t) = \sum_{i=1}^{h} \alpha_i \sin(\omega_i t + \varphi_i), \tag{4.5}$$

where α_i, φ_i, and ω_i are the amplitude, phase shift, and frequency of each periodic component, and h is the number of periodic components. Remaining uncontrollable disturbances are collected in $w^{\mathrm{u}}(t) \in \mathbb{R}^{r_u}$:

$$u^{\mathrm{u}}(t) = \begin{bmatrix} u^{\mathrm{p}}(t) \\ 0 \end{bmatrix} + w^{\mathrm{u}}(t). \tag{4.6}$$

[1] Although the estimated amplitude is not used in the current control strategy, it could be leveraged to adapt the magnitude of the downstream turbine's pitch actuation in response to variations in upstream wake strength.

Since an estimate of $u^{\mathrm{p}}(t)$ will be used for control, it is modeled as a periodic disturbance acting through the controllable actuators for estimation simplicity. Although the physical wake disturbance enters the system through unknown pathways (B^{u}), estimation is performed by reconstructing the disturbance effect in terms of the known controllable input channels (B^{c}). This is justified because the objective is to recreate the turbine's response rather than model the true disturbance path. Representing the periodic wake-induced loads as equivalent control actions allows accurate estimation and control synthesis without requiring identification of the matrix B^{u}.

To express the periodic input in state-space form suitable for Kalman filtering, we define the disturbance state vector as:

$$x^{\mathrm{p}}(t) = \begin{bmatrix} \alpha_1 \sin(\omega_1 t + \varphi_1) \\ \alpha_1 \cos(\omega_1 t + \varphi_1) \\ \vdots \\ \alpha_h \sin(\omega_h t + \varphi_h) \\ \alpha_h \cos(\omega_h t + \varphi_h) \end{bmatrix}, \tag{4.7}$$

so that:

$$u^{\mathrm{p}}(t) = \begin{bmatrix} 1 & 0 & \dots & 1 & 0 \end{bmatrix} x^{\mathrm{p}}(t), \tag{4.8}$$

$$u^{\mathrm{p}\dagger}(t) = \begin{bmatrix} 0 & 1 & \dots & 0 & 1 \end{bmatrix} x^{\mathrm{p}}(t), \tag{4.9}$$

where $u^{\mathrm{p}\dagger}(t)$ represents the quadrature (90-degree phase-shifted) component. The dynamics of $x^{\mathrm{p}}(t)$ follow as:

$$\dot{x}^{\mathrm{p}}(t) = A^{\mathrm{p}} x^{\mathrm{p}}(t), \tag{4.10}$$

where:

$$A^{\mathrm{p}} = \mathrm{diag}(\Omega_1, \dots, \Omega_h), \quad \Omega_i = \begin{bmatrix} 0 & \omega_i \\ -\omega_i & 0 \end{bmatrix}. \tag{4.11}$$

The periodic excitation frequencies ω_i are assumed to be known a priori from the upstream turbine actuation. Intuitively, the augmented states act as a virtual harmonic oscillator embedded within the system. As this oscillator evolves at the known excitation frequency, its phase and amplitude adjust to match the unmeasured periodic disturbance. This enables the Kalman filter to estimate the disturbance's effect on the system in real time, even though the forcing itself is not directly observable.

The mapping from the periodic disturbance states to the control inputs is achieved by introducing selection matrices. Specifically, the disturbance matrices are constructed as:

$$B^{\mathrm{p}} = B^{\mathrm{c}} V, \quad D^{\mathrm{p}} = D^{\mathrm{c}} V, \tag{4.12}$$

where

$$V = \begin{bmatrix} V_1 & V_2 & \dots & V_h \end{bmatrix}, \tag{4.13}$$

and each $V_i \in \mathbb{R}^{r_c}$ is a selection vector containing zeros except for a single one at the position corresponding to the control input through which the i-th periodic disturbance acts. This structure ensures that each periodic input component is associated with a specific control channel while maintaining flexibility for multi-input extensions.

The continuous-time system from Eqs. (4.1)-(4.2) augmented with the disturbance model is now given by:

$$\begin{bmatrix} \dot{x}(t) \\ \dot{x}^{\mathrm{p}}(t) \end{bmatrix} = \begin{bmatrix} A & B^{\mathrm{p}} \\ 0 & A^{\mathrm{p}} \end{bmatrix} \begin{bmatrix} x(t) \\ x^{\mathrm{p}}(t) \end{bmatrix} + \begin{bmatrix} B^{\mathrm{c}} \\ 0 \end{bmatrix} u^{\mathrm{c}}(t) + \begin{bmatrix} w(t) \\ 0 \end{bmatrix}, \tag{4.14}$$

with corresponding output equation:

$$y(t) = \begin{bmatrix} C & D^{\mathrm{p}} \end{bmatrix} \begin{bmatrix} x(t) \\ x^{\mathrm{p}}(t) \end{bmatrix} + D^{\mathrm{c}} u^{\mathrm{c}}(t) + v(t). \tag{4.15}$$

The augmented system is then discretized using a zero-order hold assumption at the controller sampling rate, yielding the discrete-time system matrices $A_{\mathrm{d}}, B_{\mathrm{d}}, C_{\mathrm{d}}, D_{\mathrm{d}}$.

4.2.2. CONNECTING THE WIND TURBINE CONTROL SYSTEM

The model is now connected to the turbine actuation system. Each blade ($i = 1,2,3$) can be actuated through its pitch angle $\theta_i(t)$. Blade root moments $M_i(t)$ can be measured. Due to coupling through the rotor, a multi-blade coordinate (MBC) transformation (Bir 2008) is applied to decouple the system into collective, tilt, and yaw components (Fig. 4.2). The backward MBC transform is:

$$\begin{bmatrix} \theta_1(t) \\ \theta_2(t) \\ \theta_3(t) \end{bmatrix} = \begin{bmatrix} 1 & \cos(\psi_1) & \sin(\psi_1) \\ 1 & \cos(\psi_2) & \sin(\psi_2) \\ 1 & \cos(\psi_3) & \sin(\psi_3) \end{bmatrix} \begin{bmatrix} \theta_0(t) \\ \theta_{\mathrm{tilt}}(t) \\ \theta_{\mathrm{yaw}}(t) \end{bmatrix}, \tag{4.16}$$

where ψ_i denotes the blade azimuth.

Helix control operates in this frame by prescribing sinusoidal tilt and yaw signals as:

$$\theta_{\mathrm{tilt}}(t) = a_h \sin(\omega_{\mathrm{e}} t), \tag{4.17}$$

$$\theta_{\mathrm{yaw}}(t) = a_h \sin(\omega_{\mathrm{e}} t \pm \pi/2), \tag{4.18}$$

with a_h the amplitude, ω_{e} the angular frequency, and the phase shift ($+\pi/2$ for CCW helix, $-\pi/2$ for CW). The angular frequency ω_{e} is governed by the dimensionless Strouhal number, which characterizes oscillating flow dynamics and is defined as the ratio of a characteristic frequency to the flow speed and a relevant length scale:

$$\mathrm{St} = \frac{f_{\mathrm{e}} D}{U}, \tag{4.19}$$

where $f_{\mathrm{e}} = \omega_{\mathrm{e}}/2\pi$ is the excitation frequency in Hz, D is the turbine rotor diameter, and U is the free stream wind speed. Previous studies have found Strouhal values between 0.2-0.4 to be optimal for wake mixing (van der Hoek, Van den Abbeele, *et al.* 2024). See Fig. 4.1 for a visualisation of the Helix wake.

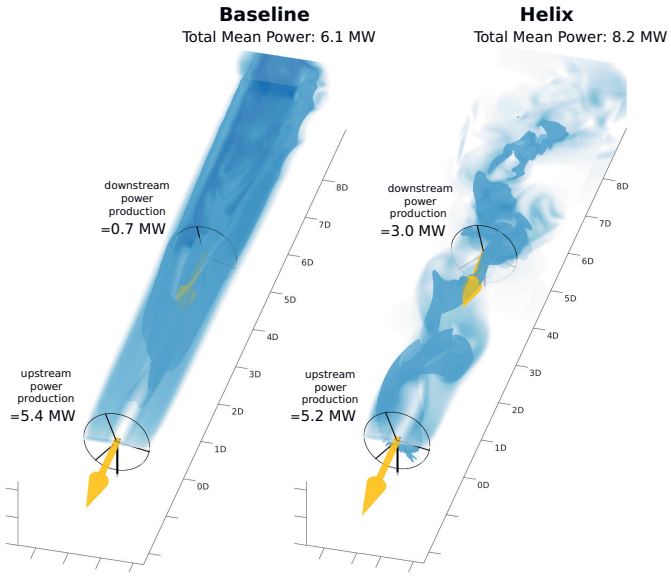

Figure 4.1: Visualization of the baseline (left) and Helix-controlled (right) cases in a two-turbine array under full wake overlap. The data is based on a Large-Eddy Simulation with laminar inflow conditions by (Frederik, Doekemeijer, *et al.* 2020), and the image is adapted from (Meyers, C. Bottasso, *et al.* 2022). Turbine spacing along the x-axis is normalized by rotor diameter D.

Similarly, blade root moments are mapped via the forward MBC transform:

$$\begin{bmatrix} M_0(t) \\ M_{\text{tilt}}(t) \\ M_{\text{yaw}}(t) \end{bmatrix} = \frac{2}{3} \begin{bmatrix} 0.5 & 0.5 & 0.5 \\ \cos(\psi_1) & \cos(\psi_2) & \cos(\psi_3) \\ \sin(\psi_1) & \sin(\psi_2) & \sin(\psi_3) \end{bmatrix} \begin{bmatrix} M_1(t) \\ M_2(t) \\ M_3(t) \end{bmatrix}. \tag{4.20}$$

A graphical representation of the fixed coordinate frame can be seen in Fig. 4.2.

To connect the abstract state-space model to the physical turbine system, we identify the controllable input vector $u^c(t)$ with the tilt and yaw components of the MBC-transformed pitch actuation:

$$u^c(t) = \begin{bmatrix} \theta_{\text{tilt}}(t) \\ \theta_{\text{yaw}}(t) \end{bmatrix}. \tag{4.21}$$

Similarly, the system output $y(t)$ consists of the measured blade root moments in the tilt and yaw directions:

$$y(t) = \begin{bmatrix} M_{\text{tilt}}(t) \\ M_{\text{yaw}}(t) \end{bmatrix}. \tag{4.22}$$

These quantities are obtained by applying the MBC transformations (Eqs. (4.16) and (4.20)) to the individual blade signals. This mapping grounds the abstract model in mea-

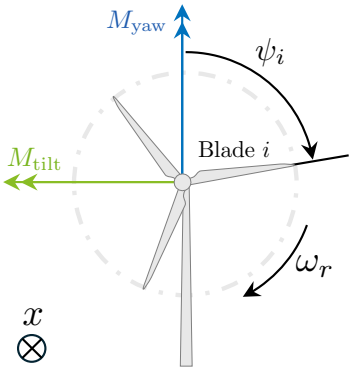

Figure 4.2: Graphic representation of blade azimuth ψ_i and associated sign convention for tilt and yaw moments M_{tilt} and M_{yaw}.

surable and actuated quantities on the real turbine, enabling state estimation and control in the rotating frame.

In the current experimental setup, however, only the fore-aft strain at the tower base is available as a measurement, which serves as a proxy for the tilt moment $M_{\text{tilt}}(t)$. No sensors are available to measure yaw-related loads or moments. As a result, system identification is performed on a single-input single-output (SISO) basis, considering only the tilt pitch input and the corresponding fore-aft strain output. This restriction simplifies the estimator implementation and focuses the phase estimation on the tilt component of the wake, which is sufficient due to the orthogonality of the tilt and yaw modes. The system output $y(t)$ is therefore limited to the fore-aft strain measurement, and the control input $u^{\text{c}}(t)$ is restricted to $\theta_{\text{tilt}}(t)$ in the present implementation.

4.2.3. PHASE EXTRACTION AND SYNCHRONIZATION

After Kalman filter estimation, the periodic states $\hat{x}_k^{\text{p}}$ are available (this step is not described here; any conventional Kalman filter method for state estimation suffices, see e.g., Verhaegen and Verdult 2007). The instantaneous phase $\phi_{i,k}$ of each periodic component i can be extracted as:

$$\phi_{i,k} = \texttt{atan2}\left(\hat{x}^{\text{p}}_{2i-1,k}, \hat{x}^{\text{p}}_{2i,k}\right). \tag{4.23}$$

The control action for the downstream turbine is synthesized as:

$$u^{\text{c}}_{i,k} = a_i \sin(\phi_{i,k} + \varphi_{\text{off}}), \tag{4.24}$$

where a_i is the desired actuation amplitude and φ_{off} a desired phase shift for synchronization. A schematic of the proposed control scheme is displayed in Fig. 4.3.

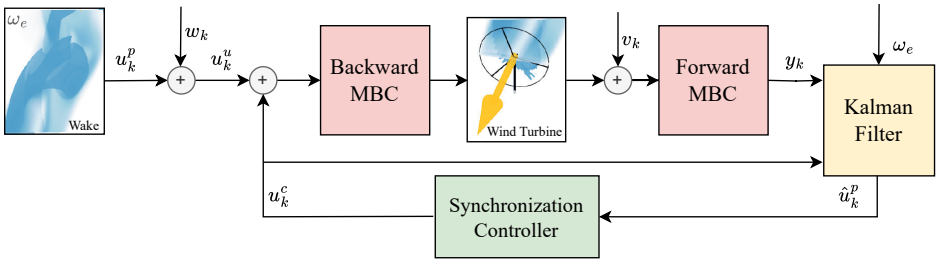

Figure 4.3: Schematic of the proposed control scheme.

4.2.4. INTERPRETATION OF φ_i

In the disturbance model of Eq. (4.5), the phase offset φ_i represents the initial phase shift of the i-th periodic component relative to a sine reference at $t = 0$. In practice, φ_i can be inferred from the estimated instantaneous phase $\phi_{i,k}$ and the known excitation frequency ω_i according to:

$$\varphi_i \approx \phi_{i,k} - \omega_i t_k, \tag{4.25}$$

where t_k is the time at step k. This allows phase differences to be computed in real time without requiring prior knowledge of the initial phase φ_i, as the estimator continuously tracks the phase from measurement data. Although the control algorithm directly uses the time-varying phase estimate $\phi_{i,k}$, the results section (Sec. 4.5) analyzes the inferred constant offset φ_i to better compare phase relationships across different cases.

4.2.5. SUMMARY

In summary, the proposed estimation framework integrates the periodic disturbance as an augmented state, enabling real-time estimation of its phase through a Kalman filter. By leveraging a known excitation frequency and mapping the disturbance effect through the controllable actuators, the method avoids the need to identify the true disturbance path. This provides a more effective and straightforward solution for downstream wake synchronization control.

4.3. EXPERIMENTAL SETUP

This section presents the experimental setup for evaluating the control scheme presented in the previous section. A description of the wind tunnel, wind turbine, and wind turbine control system is provided.

4.3.1. WIND TUNNEL

The experiments were conducted in the Open Jet Facility (OJF) at the Faculty of Aerospace Engineering, Delft University of Technology. The OJF is a closed-circuit, open-jet wind tunnel with an octagonal outlet measuring 2.85 m × 2.85 m. It has a contraction

ratio of 3:1 and is capable of reaching a free-stream velocity of up to 35 m/s, with a turbulence intensity (TI) between 0.5% and 2% Lignarolo *et al.* 2015. Unlike conventional closed-section wind tunnels, the open-jet setup minimizes wall interference, allowing for more representative wake and flow interaction studies. The current experiments were conducted at a free-stream velocity of $U = 6$ m/s. See Fig. 4.4 for a schematic of the setup in the wind tunnel.

4.3.2. WIND TURBINE

The experiment used three modified MoWiTo-0.6 scaled three-bladed wind turbines developed at Oldenburg University (Schottler *et al.* 2016) (see Fig. 4.5). Each turbine has a rotor diameter of 0.58 m and is equipped with a generator for torque control and a collective pitch control system.

Due to the small rotor size, the required Helix excitation frequency f_e is significantly higher than for utility-scale turbines. For example, compared to a modern 200 m rotor turbine, the actuation frequency is about 345 times larger (see Eq. (4.19)). This leads to stronger unsteady aerodynamic effects such as dynamic stall and lift hysteresis, resulting in greater production losses (McCroskey 1982). Previous experiments showed power losses of 10–15% on turbines applying Helix control (van der Hoek, Van den Abbeele, *et al.* 2024), while utility-scale turbines only see marginal losses in LES (Taschner, van Vondelen, *et al.* 2023).

Although the Helix excitation is applied at a fixed-frame frequency f_e, the MBC transformation shifts this in the rotating frame, interacting with the 1P frequency. The resulting blade-level frequency becomes $1P + f_e$ (CCW) or $1P - f_e$ (CW) (Bir 2008). For instance, at $U = 6$ m/s, 1P is around 16.5 Hz and f_e is 2.5 Hz, resulting in an effective 19 Hz actuation frequency for CCW Helix.

To avoid demanding high actuator bandwidth, a swashplate mechanism is used. Three stepper motors in the fixed frame actuate a static ring, which transfers motion to the rotating hub via a ball-bearing system, emulating IPC (see Fig. 4.6 for a render of this mechanism). Tilt and yaw pitching modes are generated using a Clarke transform (O'Rourke *et al.* 2019):

$$\begin{bmatrix} \theta_a \\ \theta_b \\ \theta_c \end{bmatrix} = \begin{bmatrix} 1 & 1 & 0 \\ 1 & -1/2 & \sqrt{3}/2 \\ 1 & -1/2 & -\sqrt{3}/2 \end{bmatrix} \begin{bmatrix} \theta_0(t) \\ \theta_{\text{tilt}}(t) \\ \theta_{\text{yaw}}(t) \end{bmatrix}. \tag{4.26}$$

In this setup, the collective pitch angle $\theta_0(t)$ is fixed at 10° to maintain operation near the optimal aerodynamic point. Only tilt and yaw modes are dynamically varied. The third turbine (T3) operates with greedy (non-synchronized) control.

Measurements include pitch angle, rotational speed, and generator current. Additionally, strain gauges were installed at the tower base to measure fore-aft strain, which serves as a proxy for the tilt moment. Blade root sensors were not available. As tilt and yaw modes are orthogonal, estimating only tilt is sufficient. All measurements and control commands are exchanged via a dSPACE MicroLabBox.[2]

[2] https://www.dspace.com/en/inc/home/products/hw/microlabbox.cfm

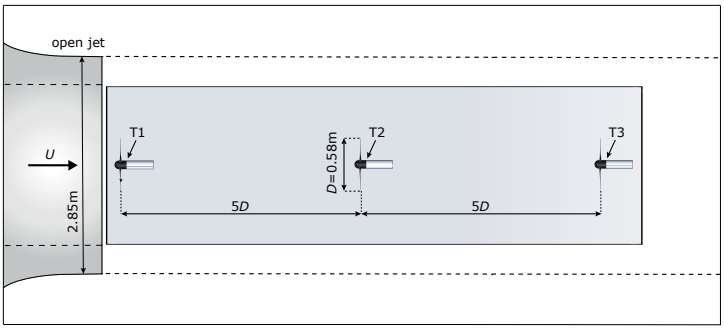

Figure 4.4: Schematic of the experimental setup in the OJF. U denotes the free stream wind speed, D the turbine rotor diameter, and $T1$, $T2$, $T3$ denote turbines 1 to 3.

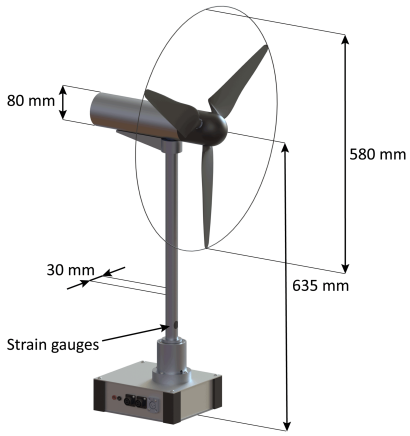

Figure 4.5: Illustration of the MoWiTo-0.6 scaled wind turbine and its dimensions and strain gauge location.

In prior work (van der Hoek, Frederik, *et al.* 2022), the aerodynamic coefficients C_{P_e} and C_T were characterized. At a tip-speed ratio of 5.5 and collective pitch of 10°, the turbine achieves maximum power. Figure 4.7 shows that even small pitch deviations reduce C_{P_e} significantly. However, because the collective pitch remains constant here, the main source of loss is unsteady aerodynamics like dynamic stall. This behavior is more pronounced in scaled turbines due to sharper C_P peaks, while full-scale turbines are more robust thanks to higher Reynolds numbers. Torque control uses a standard $K\omega^2$ law.

4.3.3. EXPERIMENTS

Each experimental trial begins with a baseline (BL) Helix case: Turbine 1 (T1) operates under Helix control, while Turbines 2 and 3 (T2 and T3) use greedy control. This estab-

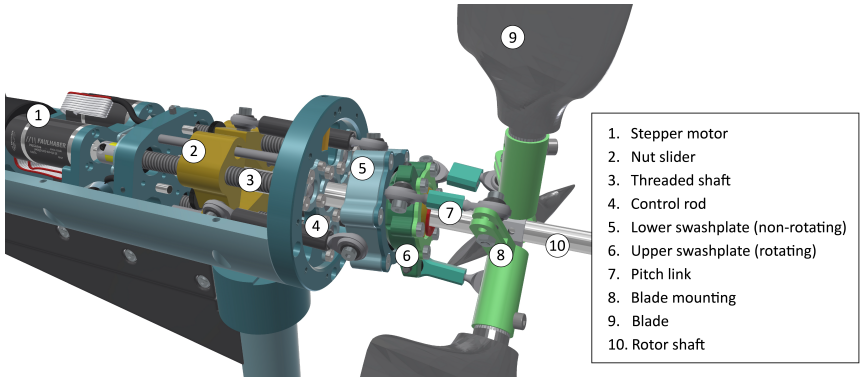

Figure 4.6: Render of the internal components of the MoWiTo-0.6 turbine with the modified swashplate mechanism. The swashplate enables IPC by translating low-frequency actuation in the fixed frame into cyclic pitching of the rotating blades, thereby facilitating implementation of the Helix control strategy at reduced actuation bandwidth requirements (van der Hoek, Van den Abbeele, *et al.* 2024).

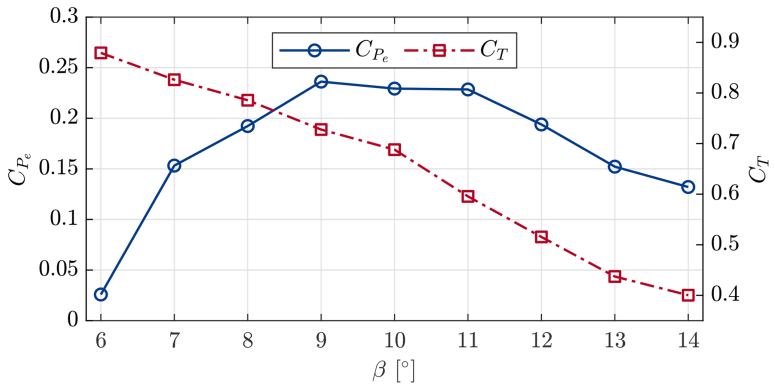

Figure 4.7: Characterization of the aerodynamic coefficients of the MoWiTo-0.6 turbine for the optimal tip-speed ratio of 5.5. Note the sharp decline of C_{P_e} for small deviations from the optimal pitch angle (van der Hoek, Frederik, *et al.* 2022).

lishes the reference performance level.

Next, a series of synchronization cases is executed, where T2 applies synchronized Helix control with a prescribed phase offset φ_{off}, selected from the set {0°, 30°, ..., 330°} in randomized order. T1 continues applying its Helix signal throughout the trial, while the Kalman filter estimation in T2 is reinitialized at each case. Each trial concludes with a second BL Helix case. Power and load results from the first and last BL cases are averaged to correct for startup effects and drift.

In total, 14 experiment trials and 3 validation trials were conducted. In the validation

trials, T2 performs phase estimation but does not apply control, allowing assessment of estimator performance alone. Each case lasts 90 seconds, followed by a 15-second transition. Figure 4.8 and Table 4.1 summarize the evaluated scenarios.

Table 4.1: Summary of the evaluated cases.

Case	T1	T2	T3
BL Helix	Helix	Greedy	Greedy
Cases	Helix	Sync Helix + 0:30:330 deg	Greedy

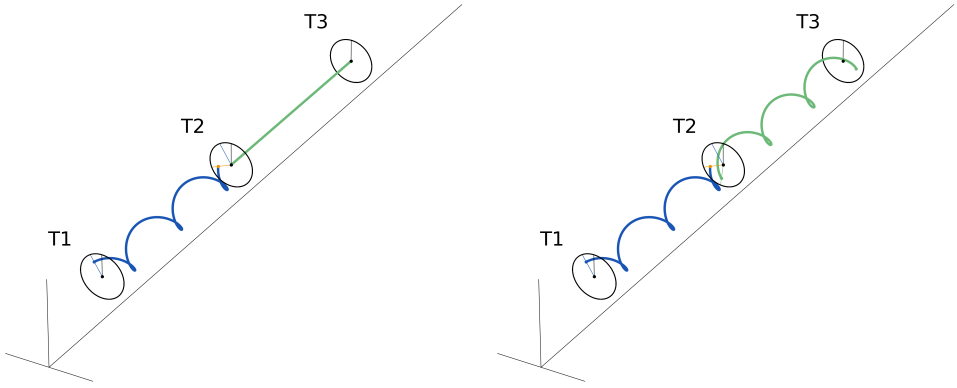

(a) BL Helix scenario (b) Synchronization

Figure 4.8: Schematic representation of the evaluated cases. In the baseline (BL) Helix scenario, only the upstream turbine (T1) applies Helix control. In the synchronization scenario, both T1 and T2 apply Helix control, with wake structures phase-aligned. T3 operates under baseline control.

4.4. SYSTEM IDENTIFICATION AND TUNING

Reliable performance of the Kalman-filter-based synchronization scheme requires an accurate linear model of the downstream turbine. Input–output data were collected at steady operating conditions using pseudo-random binary noise (PRBN) excitation. Subspace identification yielded a 5-state linear model that captures the turbine dynamics in the frequency range relevant for Helix synchronization (0.2–5 Hz). Model accuracy was confirmed by comparing the frequency response to experimental data (Fig. 4.9), with good agreement near the excitation frequency. Further details of the identification procedure, model order selection, and validation are provided in 4.A.

For Kalman filter tuning, process and measurement noise covariances were set heuristically based on repeated trials. Identified states were assigned low process noise, while augmented disturbance states were given adjustable noise to balance sensitivity and robustness. Measurement noise was set conservatively low, reflecting high sensor preci-

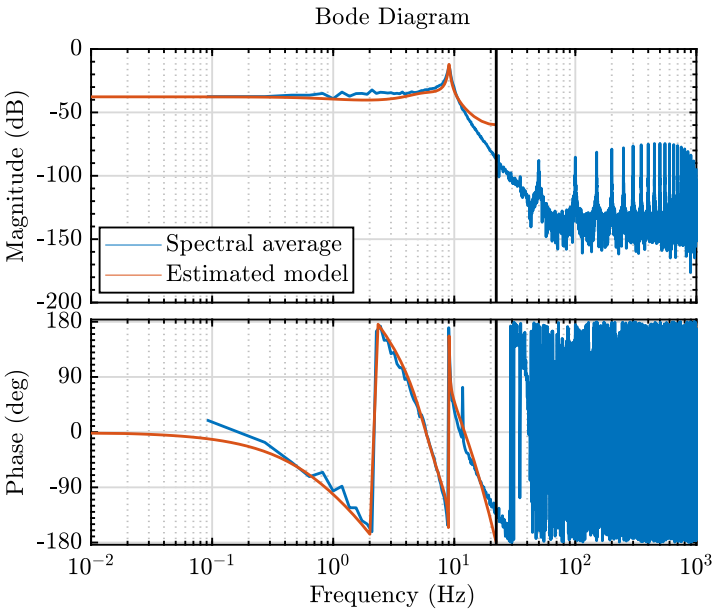

Figure 4.9: Frequency response comparison between the identified 5-state linear model and measured experimental data.

sion. This yielded stable convergence and consistent phase estimation across experiments. Full tuning details are given in 4.A.

4.5. RESULTS

This section presents the experimental results. The goal is to evaluate whether the downstream turbine can reliably estimate the phase of the incoming periodic wake *and* whether synchronized control based on that estimate improves performance. The results are grouped into three parts:

- Estimator validation, which verifies that the periodic wake can be detected in the measurements and that the estimator tracks its phase consistently.
- Repeatability analysis, which assesses how the estimated phase varies across multiple trials and under different synchronization settings.
- Synchronization performance, which analyzes how applying different phase offsets in the downstream turbine affects the power production of both that turbine and the one behind it.

4.5.1. ESTIMATOR VALIDATION

The first step in validating is to check whether the estimator can correctly detect the phase of the periodic upstream wake. Earlier studies (Frederik and van Wingerden 2022; van Vondelen, Pamososuryo, *et al.* 2025) showed that helix control creates a repeating wake pattern that appears in the strain measurements of the downstream turbine.

Let us first confirm that this periodic structure can be found in the measurement. Figure 4.10 shows the frequency content of the strain signal at the tower base of the downstream turbine. A clear peak is seen at the excitation frequency f_e, confirming the periodic nature of the wake and its presence in the measured signal.

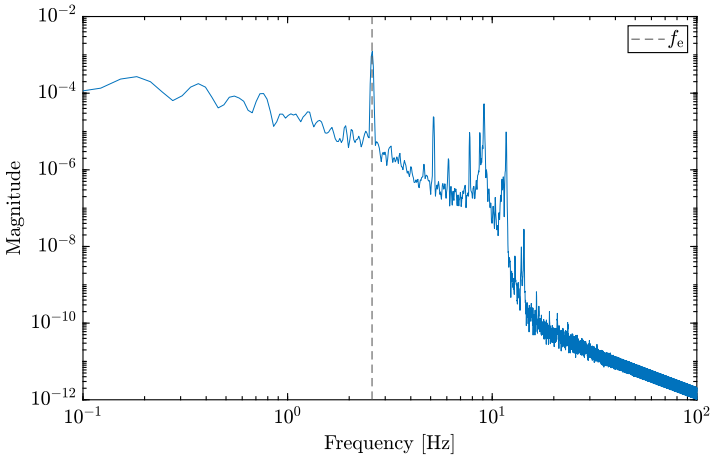

Figure 4.10: Power spectrum of the tower-base strain signal at the downstream turbine. A dominant peak appears at the helix excitation frequency f_e.

Now we need to test if the estimator can detect this signal and its phase consistently. To assess this, we conducted three open-loop trials, each consisting of 12 repetitions of the BL Helix case under identical inflow and upstream actuation conditions. In each case, the estimated phase shift was tracked over time, and a linear fit was applied to the unwrapped signal to extract a representative steady-state phase offset. Note that at this stage, we do not yet apply a control action to the downstream turbine, but only estimate the phase of the incoming wake (BL Helix case).

Let us now investigate the estimated phase shift results across the three trials. Because phase angles wrap around (e.g., 179° and −179° represent nearly the same direction), we used a method that accounts for this when computing the average phase shift in each trial. Also, the absolute phase values vary between trials. This is likely caused by small differences in how the Kalman filter was initialized in each trial. Because the estimator updates its prediction step by step, any small error at the initialization can continue throughout the whole trial. While this doesn't affect the overall trend within a single trial, it can shift the baseline of the estimated phase when comparing different trials. To better compare the spread of estimates, we therefore subtracted the average phase shift of the entire trial, $\bar{\varphi}$, from each individual estimate and wrapped the result to the interval

$[-180°, 180°]$. This gives a clear view of how much each estimate differs from the trial's average $\bar{\varphi}$, without being affected by angle wrapping.

Figure 4.11 presents the centered phase estimates using box plots. Each box indicates the 25th to 75th percentile, illustrating the spread of estimates within each trial. The spread is observed to be reasonable and consistent across all three validation trials, indicating stable estimator performance. To further assess the distribution, Fig. 4.12 shows a histogram of all centered phase estimates combined from the three trials, revealing a clear peak near zero and a symmetric distribution, suggesting unbiased estimation. Having established the reliability of the estimator in this open-loop setting, we now transition to the closed-loop scenario, where the estimated wake phase is used in real time to apply synchronized Helix control commands on the downstream turbine (T2).

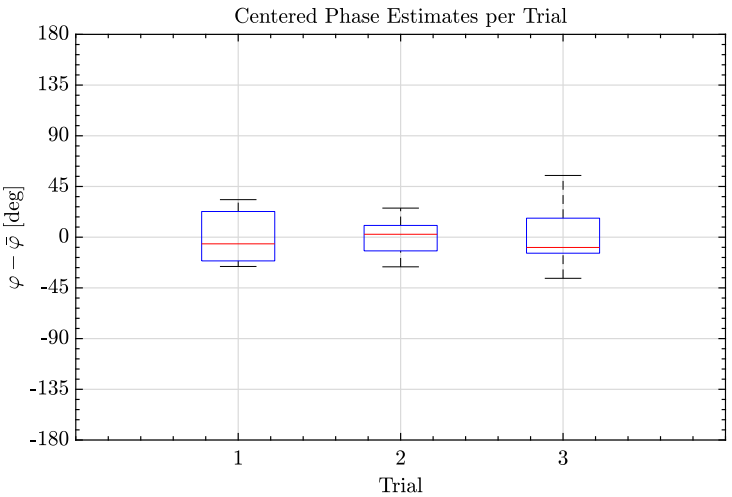

Figure 4.11: Box plot of phase estimates from three open-loop trials. Each estimate was adjusted by subtracting the trial's average $\bar{\varphi}$. The central red mark is the median, the bottom and top edges of the box are the 25th and 75th percentiles, respectively, and the whiskers denote the highest and lowest points not considered outliers.

4.5.2. REPEATABILITY OF ESTIMATED PHASE ACROSS TRIALS

The next experiment tested the estimator under active control, where different phase offsets were applied to the downstream turbine. The goal was to evaluate how the estimator performs when the downstream turbine itself changes due to actuation.

Like in the previous section, the estimated phase signal φ_k for each case was unwrapped and fitted with a linear model over the steady-state interval. The intercept of this fit, representing the steady-state phase shift φ, was then plotted against the applied phase offset φ_{off}, as shown in Fig. 4.13. However, here we now investigate the effect of φ_{off} on φ, as φ_{off} is varied at each case in the trial. A first harmonic fit was performed

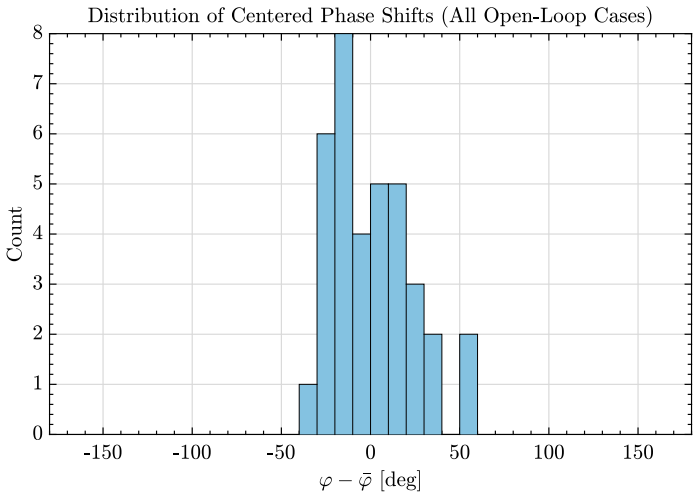

Figure 4.12: Histogram of centered phase estimates across all three open-loop trials. The narrow spread demonstrates repeatability of the estimator under identical flow conditions.

to illustrate the variation of the phase shift estimate against the applied offset. Note that the absolute values between trials differ, as discussed earlier.

Interestingly, the estimated φ is not constant across the applied φ_{off}, even though the upstream wake should remain unchanged within each trial. A consistent S-shaped trend is observed, where phase estimates are below average around 70° and above average near 250°. This behavior suggests that the estimator output is influenced by φ_{off} applied to T2 itself. Although the estimator is designed to detect the upstream wake, the cyclic actuation of the downstream turbine modifies the structural response in a nonlinear way. At certain φ_{off}, the control-induced motion either reinforces or partially cancels the wake-induced signal, leading to deviations in the estimated φ. These interactions are not accounted for by the linear Kalman filter model, which assumes additive and independent disturbances (see Coquelet, Lejeune, *et al.* 2024). As a result, the estimator slightly misattributes the combined response, causing φ estimates to vary slightly with φ_{off}. This denotes a limitation of the current estimator design: it does not model closed-loop interactions between control and wake-induced response, and may have slight bias under feedback. The presence of a bias mainly affects the absolute alignment between estimated and true wake phase, but the estimator consistently preserves the relative phase trends across applied offsets. As a result, synchronization accuracy in terms of aligning turbine response to upstream forcing remains intact, although calibration of the absolute phase may be shifted. The origin of the S-shaped bias is residual model mismatch, which causes part of the control-induced response to be projected onto the periodic state. A detailed frequency-domain derivation interpreting this bias is provided in 4.B. In future work, this limitation could be mitigated by extending the estimator to explicitly include closed-loop dynamics. Alternatively, measurement channels such as blade-root

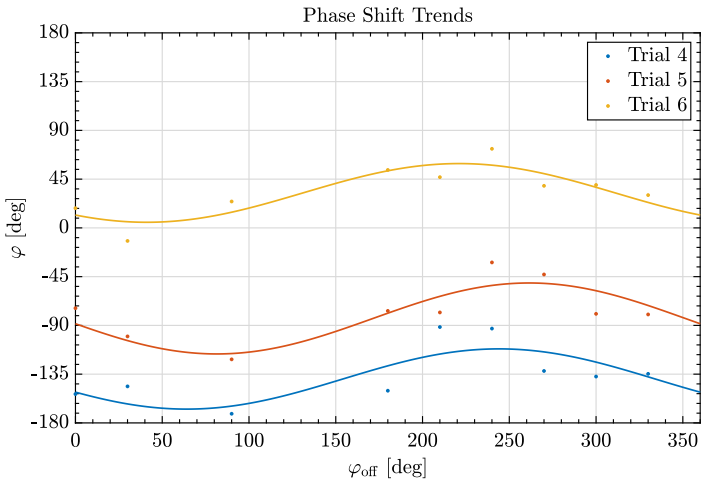

Figure 4.13: Estimated wake phase shift versus applied synchronization phase offset φ_{off}, grouped by experimental trial. Each marker corresponds to a steady-state estimate extracted from one case. Different colors represent different trials. A systematic S-shaped trend is visible, indicating that the estimator phase is slightly biased by the applied control offset.

loads or yaw moments could be added to help decouple wake- and control-induced responses.

To account for the absolute differences between trials, the mean phase shift per trial $\bar{\varphi}$ was subtracted, and the mean-centered results are shown in Fig.4.14. Gaussian Process Regression (GPR) Rasmussen and Williams 2006 was used to model the relationship between the applied phase offset φ_{off} and the estimated phase shift φ, capturing both the underlying trend and the uncertainty due to experimental variability. To reflect the periodic nature of the phase domain, the dataset was augmented with phase-shifted copies at ±360°. The shaded regions in Fig. 4.14 indicate ±1 standard deviation σ from the GPR posterior. Models were trained using MATLAB's `fitrgp` function (Statistics and Machine Learning Toolbox), with a Matérn 3/2 kernel, standardized inputs. Model fitting was fully automated within the analysis script. The consistent alignment of the individual trials and the smooth GPR trends confirm that the estimator reliably tracks the φ of the imposed offsets.

4.5.3. EFFECT OF SYNCHRONIZATION ON TURBINE PERFORMANCE

This section evaluates how synchronized Helix control affects turbine performance. In all experimental cases, the second turbine (T2) employs the proposed synchronization controller, which estimates φ of the periodic wake generated by the upstream turbine (T1) using a Kalman filter, and synchronizes its actuation accordingly.

To explore the effect of relative wake alignment between the two turbines, a prescribed phase offset φ_{off} is applied to the synchronized control action of T2. That is, the con-

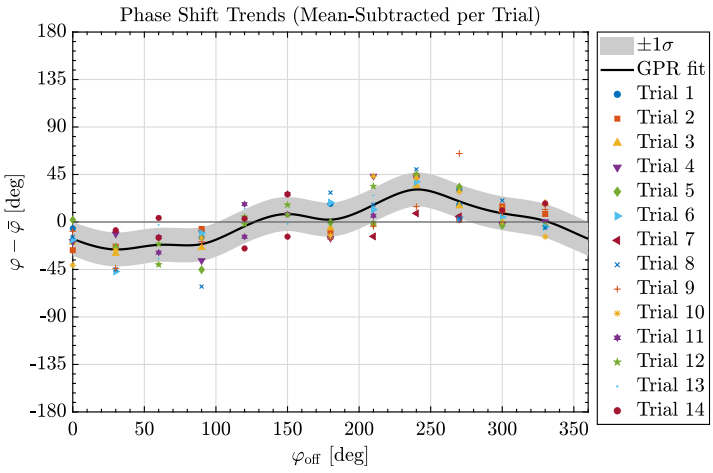

Figure 4.14: Mean-subtracted wake phase estimates across trials. For each trial, the average phase shift $\bar{\varphi}$ was removed to highlight the relative dependence on φ_{off}. The solid line shows a Gaussian Process Regression (GPR) model fitted to the data, and the shaded area denotes one standard deviation of posterior uncertainty. The alignment of data across trials confirms repeatability, while the smooth GPR curve emphasizes the consistent bias trend.

troller enforces actuation of T2 with a fixed phase shift relative to the estimated incoming wake phase, ranging from 0° to 330° in 30° increments. This setup ensures that all performance differences result directly from variations in synchronized phase alignment, while the upstream turbine applies a constant Helix.

Gaussian process regression is used to model the relationship between the applied phase offset and performance indicators. Figure 4.15 shows the GPR-modeled power production as a function of the applied phase offset, including ±1 standard deviation σ uncertainty bands from the posterior distribution. Similar settings as in the previous section were used, but here the noise standard deviation was fixed at $\sigma_{\text{noise}} = 0.02$. Turbine 1 applied a constant Helix forcing throughout the experiment, and its power output is unaffected across φ_{off}. It therefore acts as a fixed wake generator, while the relevant array-level variation arises from the trade-off between T2 and T3. For this reason, T1 is not further analyzed in terms of power or loads. Accordingly, we define the combined output of T2+T3 as the relevant array-level metric in this setup.

The third turbine (T3) shows a clear pattern: power increases by about 3% at a φ_{off} near 270°, and drops near 120°. This confirms that the phase difference between T1 and T2 affects how their wakes interact, either amplifying or canceling each other. Interestingly, the exact positions of the peak and dip are not 180° apart, which could be expected from ideal constructive and destructive interference.

T2's power output is consistently about 15% lower than in the baseline helix scenario. This reduction is caused by aerodynamic losses from the continuous pitch motion used for synchronization. As explained in Section 4.3, although the mean pitch angle remains

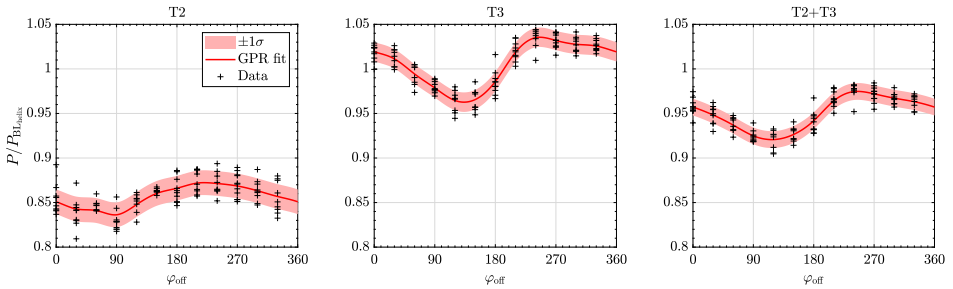

Figure 4.15: Normalized power production of turbines T2, T3, and the combined array as a function of applied synchronization phase offset at T2. T1 was held at a fixed Helix setting and therefore omitted. T3 shows a systematic dependence on phase offset, with a maximum gain of about 3% near $\varphi_{\mathrm{off}} \approx 270°$ and a minimum near 120°. T2 consistently experiences an approximate 15% power loss due to unsteady aerodynamic effects of cyclic pitching at model scale. The combined output (T2+T3) does not increase in this setup, but at utility scale, where cyclic losses are negligible, array-level benefits are expected.

at its optimal value, the cyclic actuation introduces effects such as lift hysteresis and dynamic stall, which reduce aerodynamic efficiency. These effects are particularly present in small-scale turbines, where the power coefficient curve drops steeply around the optimal value and Reynolds numbers are low. At utility scale, pitch amplitudes are orders of magnitude smaller relative to rotor dynamics, and such unsteady aerodynamic penalties are negligible. As a result, the absolute efficiency losses observed at T2 in this setup should not be directly generalized to full-scale turbines. Instead, the experiments should be viewed as a proof-of-principle demonstration of synchronization, with the main insight being the relative dependence of downstream performance on phase offset rather than the absolute values of turbine efficiency.

The optimal phase offset φ_{off} differs between the wind tunnel experiments and the LES study done in (van Vondelen, Pamososuryo, *et al.* 2025) and (Korb, Asmuth, and Ivanell 2023) due to variations in both the definition of φ_{off} and the estimation approach. In this study, a linear Kalman filter estimates the phase of the periodic wake-induced pitch disturbance on the downstream turbine, and the phase offset is defined relative to this estimated phase. Conversely, the EKF-based approach (van Vondelen, Pamososuryo, *et al.* 2025) defines the phase offset as the offset applied to the phase of the estimated periodic wind speed component impinging on the downstream turbine, while (Korb, Asmuth, and Ivanell 2023) determines the downstream wake phase through flow field analysis. These fundamentally different reference frames and estimation methodologies make it non-trivial to back-calculate an absolute phase shift between the approaches. In the current approach, all phase lags introduced by the turbine dynamics between the inflow, wake, and resulting blade loads are implicitly included, whereas the EKF-based approach does not capture these internal dynamics. Given the nonlinear nature of wind turbine behavior, these phase lags are also operating-point dependent (e.g., wind speed

and rotor speed). However, all these studies show similar trends, where there are regions of optimal and suboptimal power production, following a characteristic S-curve.

Figure 4.16 was created using identical GPR methodology. It shows the magnitude of the power spectrum at the excitation frequency against the applied φ_{off}, which reflects the degree of constructive or destructive interference between the turbine's pitching motion and the periodic incoming wake. Interestingly, the peak in fore-aft strain occurs around 150°, which does not align with the peak in power production at approximately 270°. Instead, it seems that the region of low power production is associated with higher tower-base strain, which aligns with results obtained in the DIC wind tunnel experiment (van Vondelen, van der Hoek, *et al.* 2024). Also in (van Vondelen, Coquelet, *et al.* 2025), this behavior is observed for the tower-base load. From that study, note that other components, such as the blades and tower top, experience increased fatigue around the phase offset region of high power production. This shows that the phase offset giving the highest power production is different from the one that minimizes structural loading, suggesting that future control strategies need to balance both objectives.

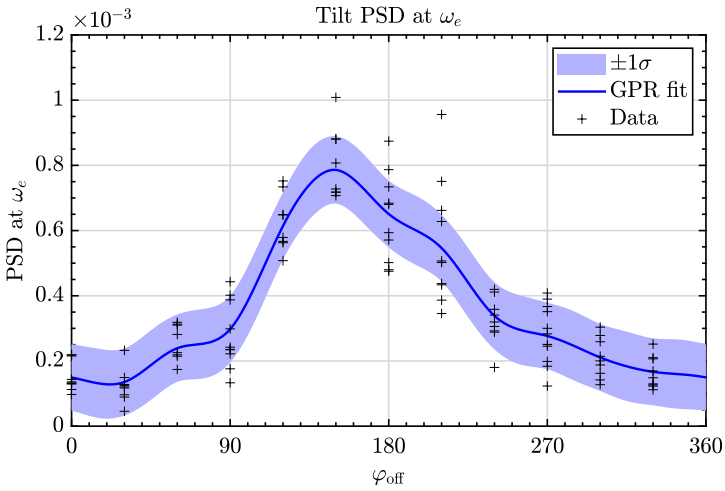

Figure 4.16: Magnitude of the tower-base strain spectrum at the excitation frequency ω_e as a function of synchronization phase offset φ_{off}. Solid line shows a Gaussian Process Regression (GPR) fit with shaded one-standard-deviation uncertainty bands. Peaks indicate constructive interference between wake-induced and control-induced loading, while troughs indicate partial cancellation. Notably, the load maximum occurs at a different phase offset than the power maximum (Fig. 4.15), illustrating a trade-off between maximizing energy capture and minimizing structural loading in synchronized wake control.

4.6. CONCLUSION

This study introduced and experimentally validated a synchronization control scheme aimed at leveraging periodic wake structures caused by upstream turbines to enhance the performance of downstream turbines. The control methodology extends previous theoretical work by incorporating a Kalman-filter-based phase estimation algorithm tailored specifically for wind turbine applications, employing the MBC framework for integration with individual pitch control.

Experimental validation conducted on a scaled three-turbine wind farm setup in a controlled wind tunnel environment demonstrated the estimator's capability to consistently and accurately track periodic wake structures generated upstream. The evaluation of different synchronization phase offsets revealed a dependency of downstream turbine performance on the imposed phase difference. The optimal phase offset for maximizing energy production at the third turbine resulted in a power gain of approximately 3% on the third turbine compared to a baseline Helix scenario without synchronization. Interestingly, the experimentally observed peak and dip in T3 production are not 180° apart. We hypothesize that non-ideal interference and operating point-dependent phase lags contribute to this shift. Quantifying these lags and their dependence on operating conditions is a direction for future work. The actuating turbine (T2) experienced a power decrease of about 15% due to small-scale unsteady aerodynamic effects associated with cyclic pitching at the high actuation frequencies of the model turbines. Importantly, when considering total array production, T1 acted as a fixed wake generator with constant output, so the relevant variation arises from T2 and T3. Their combined output did not show a systematic increase over the baseline Helix case, as losses at T2 generally outweighed gains at T3 in this small-scale setting; at utility scale, where cyclic pitch amplitudes and associated losses are much smaller, array-level benefits are expected to be more significant, as demonstrated in simulations in earlier work.

The experimental scope has several limitations that provide context for the interpretation of these results: (i) no blade load sensors were available, preventing advanced blade-element modeling in the estimator; (ii) a linear Kalman filter relying solely on tower-base fore–aft strain was employed, which limits the operating range; (iii) the current estimator design does not explicitly model closed-loop interactions between downstream actuation and measured response, which introduced a small phase-estimation bias that varied with the applied offset; (iv) all experiments were conducted around a fixed operating point (constant wind speed, fixed mean pitch angle) with periodic forcing at a single frequency, so variability across operating conditions and varying frequencies is not examined; (v) scaling limitations inherent to wind tunnel models restrict direct extrapolation of absolute performance values to full-scale turbines, and the findings should primarily be interpreted in terms of relative phase–performance trends; and (vi) the narrow sensor suite restricted validation to tower-base fore–aft strain only, preventing assessment of yaw-related and blade-root loads, so the estimator–controller framework was demonstrated in a simplified SISO setting rather than its full multivariable form.

The findings from the wind tunnel also have broader implications for wind farm control. In large offshore arrays, where multiple turbines are persistently exposed to wakes, the ability of downstream turbines to synchronize with upstream-induced periodic structures may provide a means to improve array-level performance. The exper-

iments show that downstream power depends sensitively on the relative phase alignment, indicating that coordinated synchronization across several turbines could enhance overall farm efficiency beyond what is achieved with conventional methods. At the same time, the observed difference between the phase offsets that maximize power and those that reduce structural loading stresses the need for multi-objective control approaches that consider both power production and fatigue life. These results suggest that synchronization can complement existing strategies as wind farms become larger and more densely packed.

Future work could explore nonlinear or adaptive modeling approaches to enhance estimation robustness under dynamic control conditions, explicitly address closed-loop coupling in the observer, and incorporate blade load sensing to enable more advanced models. In addition, full-scale field tests and extensive numerical simulations should evaluate multi-objective, array-level control that balances total production and structural loading across turbines beyond a single operating point.

4.A. DETAILS ON SYSTEM IDENTIFICATION AND TUNING

The proposed Kalman-filter-based synchronization control scheme requires an accurate system model to reliably estimate the periodic wake disturbances. Although wind turbines are inherently nonlinear, linear system identification is frequently employed in practice due to its relative simplicity and computational efficiency. However, linear models are typically only accurate around their specific operating points, which means that a different model may be required for other operating conditions (e.g., wind speeds, rotor speeds).

IDENTIFICATION PROCEDURE

To identify a suitable linear model, input-output data were collected at steady-state conditions using pseudo-random binary noise (PRBN) applied to the tilt control input for 30 minutes. The PRBN excitation frequency content extended up to 6 Hz, surpassing the actuator bandwidth of about 5 Hz, ensuring persistent excitation within the relevant frequency range. The turbine response was measured using the tower-bottom fore-aft strain gauge (see Fig. 4.5).

Before identification, the data were preprocessed to remove biases and high-frequency noise. Specifically, the data were mean-centered, detrended, and resampled from the original sampling frequency of 2 kHz to 25 Hz (factor of 80 reduction) to focus identification on the low-frequency dynamics most relevant for synchronized wake control.

The identification procedure employed the optimal predictor-based subspace identification method ($\text{PBSID}_{\text{opt}}$) as described in (Chiuso 2007), due to its robustness and suitability for linear system identification from noisy data.

MODEL ORDER SELECTION AND VALIDATION

The selection of the appropriate system order is critical to ensure that the model accurately captures the essential system dynamics without unnecessary complexity. Singular value decomposition (SVD) of the Hankel matrix was initially performed, but it provided

no definitive indication of an optimal model order. Therefore, a model set with orders ranging from 3 to 10 was evaluated based on frequency-response fits.

A 5-state model emerged as the most appropriate choice, as lower-order models inadequately captured the resonances, whereas higher-order models only provided marginal improvements while introducing complexity.

The accuracy of the selected 5-state model was validated by comparing its frequency response with the measured experimental data, as illustrated in Fig. 4.9. The model accurately represents the system behavior in the frequency range crucial for the wake mixing control experiments (approximately 0.2 Hz to 5 Hz), particularly around the wake excitation frequency ($f_e \approx$ 1–3 Hz). Minor discrepancies are present above 5 Hz, but these frequencies are outside the band of interest for wake mixing control.

FINAL IDENTIFIED MODEL

The final discrete-time linear state-space model used in the Kalman-filter implementation is represented as:

$$x_{k+1} = A_d x_k + B_d u_k + w_k, \tag{4.27}$$

$$y_k = C_d x_k + D_d u_k + v_k, \tag{4.28}$$

where matrices $\{A_d, B_d, C_d, D_d\}$ were obtained from the optimal PBSID identification procedure. Process noise w_k and measurement noise v_k are modeled as zero-mean white Gaussian sequences with finite covariance.

In the identified model, the input $u_k \in \mathbb{R}$ corresponds to the tilt control command (Eq. (4.16)) applied to the second turbine. The output $y_k \in \mathbb{R}$ is the measured fore-aft tower-base strain, which serves as a proxy for the tilt moment (Eq. (4.20)). Thus, the identified system is single-input, single-output (SISO), consistent with the actuation and sensing architecture described in Section 4.3. Although the full multi-blade system is inherently multivariable, only the tilt input and response are considered for identification, as this mode directly captures the periodic loading used for phase estimation. This choice is motivated by the availability of strain sensing and the orthogonality of the tilt and yaw axes, as discussed in Section 4.2.2.

This linear model was subsequently augmented with the periodic disturbance states and integrated into the Kalman-filter-based synchronization control framework for experimental evaluation. The number of periodic components in the disturbance model is set to $h = 1$, corresponding to the known Helix excitation frequency ω_e. The disturbance state vector $x_p(t) \in \mathbb{R}^{2h}$ therefore has dimension 2, capturing the in-phase and quadrature components (i.e., sine and cosine) of this single frequency. While the framework allows for multiple periodic inputs with arbitrary frequencies ω_i, only a single component is used in the current experiments due to the upstream wake excitation with ω_e.

KALMAN FILTER TUNING

The Kalman filter is initialized with zero state estimates and an identity matrix for the error covariance. To ensure consistent convergence across experimental repetitions, the filter state and covariance are reset at the start of each new case. This is triggered using a pulse signal that rises from 0 to 1 on the first timestep of a new case. On this rising edge,

both the state estimate and the error covariance matrix are reinitialized. This prevents residual estimation errors or phase lag from persisting across cases, which is especially important when comparing performance across different control phase offsets.

The process and measurement noise covariances were tuned heuristically by evaluating performance across multiple trials. In this context, performance refers to the consistency and accuracy of the estimated wake phase, as validated by repeatability in open-loop experiments (see Section 5.1) and by the correlation between estimated phase offsets and downstream power production trends (Section 5.3). Lower process noise was assigned to the identified states, while the augmented periodic disturbance states were given adjustable noise levels to balance phase tracking sensitivity and robustness. Measurement noise was set conservatively low to reflect the high precision of the available sensor data. Tuning parameters were iteratively adjusted to minimize phase estimation drift and ensure stable convergence across repeated experiments, without the use of a formal optimization procedure.

4.B. DETAILED INTERPRETATION OF ESTIMATOR BIAS

To interpret the estimator bias, let us analyse the estimator output at the excitation frequency $\omega = \omega_e$. The response of the strain gauge can be expressed in the frequency domain as:

$$Y(j\omega) = G_c(j\omega)\, U^c + G_w(j\omega)\, U^p, \tag{4.29}$$

with $U^c = A_c e^{j\phi_c}$ the applied control phasor and $U^p = A_w e^{j\phi_w}$ the upstream wake phasor. The model used in the Kalman filter predicts:

$$\widehat{Y}(j\omega) = \widehat{G}_c(j\omega)\, U^c + \widehat{G}_w(j\omega)\, \widehat{U}^p. \tag{4.30}$$

Any mismatch between the identified model and the real system $\Delta G_c = G_c - \widehat{G}_c$ contributes to a residual between the measured and predicted output, i.e., the innovation of the Kalman filter, which the filter projects onto the periodic state, because in the SISO implementation we have $V = 1$, as such $B^p = B^c$ and $D^p = D^c$. As a result, the residual cannot be distinguished from the periodic disturbance, and it is partially projected onto the periodic state estimate. This channel alignment was chosen deliberately to avoid having to identify the true disturbance pathway. While this simplifies implementation, it also implies that the filter cannot cleanly separate control-induced and wake-induced dynamics in the case of model mismatch. At steady state, this model mismatch propagates as:

$$\widehat{U}^p \approx U^p + H(\omega)\, \Delta G_c(\omega)\, U^c, \tag{4.31}$$

where, $H(\omega)$ represents the frequency-dependent mapping from innovation to the disturbance state that arises from the Kalman filter update. Writing $H(\omega)\Delta G_c(\omega) = |B| e^{j\delta}$ yields:

$$\widehat{U}^p = A_w e^{j\phi_w} + |B| A_c e^{j(\phi_c+\delta)}, \tag{4.32}$$

where $|B|$ is the magnitude of the bias contribution and δ is its phase angle. The estimated phase, therefore, becomes:

$$\hat{\phi} - \phi_w = \arg\left(1 + \rho e^{\mathrm{j}(\varphi_{\text{off}}+\delta)}\right), \qquad \rho = \frac{|B|A_c}{A_w}, \tag{4.33}$$

which is the argument of a two-vector phasor sum. As $\varphi_{\text{off}} = \phi_c - \phi_w$ is varied, this relation yields the characteristic S-shaped trend seen in Fig. 4.13. In the ideal case $\Delta G_c = 0$, the bias term vanishes and $\hat{\phi} = \phi_w$, independent of φ_{off}.

5

EXTENDED KALMAN FILTER FOR SYNCHRONIZED WAKE MIXING

Wind farm control optimizes wind turbines collectively, implying that some turbines operate suboptimally to benefit others, resulting in a farm-level performance increase. This study presents a novel control strategy to optimize wind farm performance by synchronizing the wake dynamics of multiple turbines using an Extended Kalman Filter (EKF)-based phase estimator in a Helix control framework. The proposed method influences downstream turbine wake dynamics by accurately estimating the phase shift of the upstream periodic Helix wake and applying it to its downstream control actions with additional phase offsets. The estimator integrates a dynamic Blade Element Momentum model to improve wind speed estimation accuracy under dynamic conditions. The results, validated through turbulent large-eddy simulations in a three-turbine array, demonstrate that the EKF-based estimator reliably tracks the phase of the incoming Helix wake, with slight offsets attributed to model discrepancies. When integrated with the closed-loop synchronization controller, significant power enhancement with respect to the single-turbine Helix can be attained (up to +10% on the third turbine), depending on the chosen phase offset. Flow analysis reveals that the optimal phase offset sustains the natural Helix oscillation throughout the array, whereas the worst phase offset creates destructive interference with the incoming wake, which appears to negatively impact wake recovery.

This chapter is based on previously published work:
van Vondelen, A. A. W., Coquelet, M., Navalkar, S. T., and van Wingerden, J.-W. (2025). "Synchronized Helix wake mixing control". In: *Wind Energy Science* 10.10, pp. 2411–2433. DOI: 10.5194/wes-10-2411-2025.

Contents

5.1. INTRODUCTION

Optimizing wind farm layout is an important aspect of wind farm design (Manwell, McGowan, and Rogers 2010). Specifically, the spacing between wind turbines, typically ranging from 3 to 7 rotor diameters, has a strong influence on power production and turbine fatigue life due to the presence of wake interactions between turbines. When the wind direction aligns with the turbine array, downstream turbines can experience a performance drop of up to 20% in some large offshore wind farms (Barthelmie *et al.* 2009). However, increasing the spacing between turbines requires more offshore sea and cabling, reducing the energy density and increasing the cost of the power production site. Therefore, a site-specific trade-off is often made, balancing cost optimization with accepted losses due to wake effects.

To mitigate these losses in existing and future wind farms, researchers are exploring innovative control solutions to recover the 'lost' energy. One prominent method is wake steering, which involves intentionally misaligning the upstream turbine's rotor to redirect the wake away from downstream turbines (Fleming, Gebraad, *et al.* 2014). While promising, this technique only slightly reduces the wake intensity and may still impact other turbines further downstream in the farm. Also, if the wake is not deflected enough, it can still partially impinge on downstream turbines, which can cause load increases. Recent advancements in optimizing farm layouts using control co-design with wake steering have shown potential for further enhancing production (Baricchio, Gebraad, and van Wingerden 2024; Stanley, Bay, and Fleming 2023).

Another category of wind farm control approaches focuses on wake mixing, which aims to enhance the mixing of the wake with the surrounding free stream flow. The earliest method, dynamic induction control (DIC), involves dynamically varying the turbine thrust, either by adjusting torque or pitch, to create a pulsating wake that mixes more rapidly with the free stream (Frederik, Weber, *et al.* 2020; Goit and Meyers 2015). This approach has demonstrated moderate power gains (up to 4.6% on T2 in two-turbine setups with 2.5 degree pitch amplitude) (Frederik and van Wingerden 2022), albeit with substantially increased tower load variations, up to 104% higher tower DELs compared to baseline operation under low turbulence intensity conditions (Frederik and van Wingerden 2022).

A later method involves rotating the thrust vector across the rotor disk, creating a helical wake shape (Frederik, Doekemeijer, *et al.* 2020). Compared to DIC, the Helix approach results in lower tower load variations and higher power gains, garnering considerable attention (Frederik and van Wingerden 2022; van Vondelen, Navalkar, Kerssemakers, *et al.* 2023). For instance, the counterclockwise Helix implementation achieved a 12.1% increase on T2 with 2.5 degree pitch amplitude while increasing tower loads by only 11% under similar conditions. On downstream turbines (which are impinged by a Helix or DIC wake while operating at baseline control), Helix was also shown to induce 5–10% lower fatigue loads than DIC. One major challenge remains the pitching frequency of the actuators. While similar to that of IPC, DIC has significantly lower pitch variations, limiting damage to the pitch bearings significantly. Nevertheless, these findings demonstrate a more favorable trade-off between performance and structural loading for Helix wake mixing.

Most studies have applied the Helix approach to an upstream turbine, maintaining

baseline control for the downstream turbines. However, in multi-turbine arrays, applying the Helix approach to multiple turbines could potentially enhance overall power production further. For instance, Korb, Asmuth, and Ivanell 2023 explored a three-turbine setup with the two upstream turbines employing Helix and the downstream turbine employing baseline control. They found that the power output depends on the phase shift between the two helix wakes, though they did not propose a method for achieving this phase difference. Similar results were found in a three-turbine wind tunnel experiment with DIC (van Vondelen, van der Hoek, *et al.* 2024). However, both studies also observe power losses at certain phase shifts, highlighting the importance of optimizing the synchronization.

While Korb, Asmuth, and Ivanell 2023 and van Vondelen, van der Hoek, *et al.* 2024 have shown that phase differences between periodic wakes in a multi-turbine setup can influence power production, a robust synchronization method remains lacking. Moreover, even without active control, wake deficits naturally recover through entrainment and wake–to-wake interactions: large-eddy simulations indicate that by the fourth to sixth turbine row, the average velocity deficit has already recovered substantially (R. J. A. M. Stevens, Gayme, and Meneveau 2015). Consequently, dynamic wake-mixing strategies yield their greatest benefit in the first two to three rows, where the deficit is strongest. Extending phase-synchronized Helix control to these upstream rows is therefore essential to maximize farm-level performance. Hence, it is important to address this research gap.

To establish the concept of synchronized Helix wake mixing, van Vondelen, Ottenheym, Pamososuryo, *et al.* 2023 suggested synchronizing turbines by estimating the phase of the incoming Helix wake on the downstream turbine from the blade loads using a linear Kalman filter, allowing for downstream control actions that incorporate the Helix's phase and any desired phase offset. While promising, this technique may only provide accurate phase estimates near the system model's linearization point, and phase estimates may deteriorate when the turbine's state goes far from this region. Recognizing its potential, the approach has been patented despite the need for further improvements (van Vondelen, Ottenheym, Kalogera, *et al.* 2025).

A more versatile approach is proposed in van Vondelen, Pamososuryo, *et al.* 2025, where an output feedback controller is designed for the downstream turbine to maintain a magnitude reference on the periodic load caused by the impingement of the Helix wake, essentially amplifying the Helix while preserving phase. This method allows for robust amplitude control of the periodic wake and thus gives direct control of the magnitude of the load. Being output-only, it cannot apply an out-of-phase control action, as the blade is both the sensor and the actuator. It is not possible to discern the phase of the load effect of the incoming wake from the total load, which also contains the effect of an out-of-phase control action. This in-phase synchronization approach has demonstrated a 6% power improvement on the third turbine, beyond the power increase of the baseline Helix effect. However, according to Korb, Asmuth, and Ivanell 2023, better performance may be achieved with an out-of-phase shift, suggesting further potential for power gains through out-of-phase synchronization.

As such, this study proposes an Extended Kalman Filter (EKF)-based phase synchronization method, building on the initial concept from van Vondelen, Ottenheym,

Pamososuryo, *et al.* 2023. The novel controller employs an EKF and is capable of handling nonlinearities addressing the limitations of the linear Kalman filter used in van Vondelen, Ottenheym, Pamososuryo, *et al.* 2023. Also, it utilizes a dynamic blade-element momentum (dynBEM) model in the EKF as suggested by Coquelet, Lejeune, *et al.* 2024, which should provide a more robust model of the simulated turbine while performing dynamic pitch actions compared to regular BEM. The main contributions of this study are as follows:

1. **Extending the EKF-based estimator for Helix phase detection:** We extend the EKF-based wind speed estimator incorporating dynBEM (Coquelet, Lejeune, *et al.* 2024) to track Helix flow oscillations regardless of dynamic pitching. By inclusion of a parametric model, including several coordinate transformations, and tuning of the internal models, the estimator is able to isolate the wake's phase from blade load signals—thus enabling synchronized Helix control.

2. **Development of a synchronized Helix wake mixing control framework:** The EKF-based estimator for Helix phase detection is integrated into a closed-loop control framework for synchronized Helix wake mixing control on downstream wind turbines.

3. **Application to multi-turbine Helix control:** The proposed synchronized Helix wake mixing method is applied to a three-turbine array, demonstrating significant power gains while systematically exploring the impact of phase offsets on power production and structural loads.

4. **Comprehensive validation framework:** High-fidelity large-eddy simulations coupled with OpenFAST provide a detailed validation of the proposed method, offering insights into optimal configurations and real-world applicability.

5. **Insights into wake dynamics and interference mechanisms:** The study provides novel insights into how constructive and destructive wake interference influences wake recovery by examining wake centerlines and velocity deficits across the simulation domain.

This work covers a broad range of topics: estimation, control design, high-fidelity simulation, and flow analysis. These components are integrated to address a central objective: enabling synchronized wake mixing control in a realistic wind farm environment using only local turbine measurements. Each component contributes to this goal. The estimator infers the phase of upstream Helix wake motion; the controller synchronizes the actuation of downstream turbines; high-fidelity simulations provide a realistic testing environment; and fatigue and flow analyses assess the resulting impact on turbine performance and wake development. Together, these elements provide a comprehensive evaluation of the proposed approach. To help navigate the scope of this work, an outline is provided below.

Section 5.2 introduces the estimation and control framework. It describes the baseline Helix control approach, presents the Extended Kalman Filter (EKF) for estimating the upstream wake phase from turbine blade loads, outlines the wake parametrization and

the dynBEM-based internal model, explains the noise tuning strategy, and introduces the synchronization controller design.

Section 5.3 describes the high-fidelity simulation setup, including the inflow conditions, turbine model, and control implementation. The section also defines the evaluation cases and performance metrics.

Section 5.4 presents the results. First, the EKF estimator is validated against the ground truth. Then, the closed-loop control performance is analyzed in terms of power production and structural loading. Finally, flow visualizations and velocity deficit analyses are used to interpret the underlying physical mechanisms of synchronization.

Section 5.5 compares the results of this work with earlier studies and discusses the limitations compared to our approach.

Section 5.6 concludes this work and presents possible future research directions.

5.2. ESTIMATION AND CONTROL METHODS

This section presents the estimation and control methods that form the foundation of the proposed phase synchronization method. It covers the fundamentals of the Helix approach for wake mixing control and introduces the Extended Kalman Filter as the tool for estimating the wake phase shift and enabling synchronized control actions. Furthermore, the parametrization of the Helix wake required for detection is provided, along with the phase synchronization controller design. Lastly, specific tuning methodology is discussed, for both the dynBEM and estimator.

5.2.1. THE HELIX APPROACH

The Helix approach is an open-loop control strategy that enhances the power output of downstream wind turbines by applying periodic signals to the upstream wind turbine's blades (see Fig. 5.1 for an illustration).

Typically, the actuation commands are provided as *tilt* and *yaw* commands in the 'fixed' coordinate frame. Using the so-called backward Multi-Blade Coordinate (MBC) transformation, the Helix tilt and yaw commands (β_{tilt} and β_{yaw}) are converted into effective pitch commands for each blade (β_i, where $i = 1,2,3$):

$$\begin{bmatrix} \beta_1 \\ \beta_2 \\ \beta_3 \end{bmatrix} = \underbrace{\begin{bmatrix} 1 & \cos(\psi_1+\psi_o) & \sin(\psi_1+\psi_o) \\ 1 & \cos(\psi_2+\psi_o) & \sin(\psi_2+\psi_o) \\ 1 & \cos(\psi_3+\psi_o) & \sin(\psi_3+\psi_o) \end{bmatrix}}_{T_{\text{cm}}^{-1}(\psi(t)+\psi_o)} \begin{bmatrix} \beta_{\text{col}} \\ \beta_{\text{tilt}} \\ \beta_{\text{yaw}} \end{bmatrix}, \tag{5.1}$$

where ψ_i is the azimuthal position of blade i (see Fig. 5.2 for definition) and ψ_o is an azimuth offset accounting for unmodeled actuator delays and blade flexibility, which is required to fully decouple the tilt and yaw channels (Mulders *et al.* 2019; van Vondelen, Pamososuryo, *et al.* 2024). The pitch angle sign convention is the following: increasing the pitch angle corresponds to pitching to feather and reduces the force intensity on the blade while decreasing the pitch angle value corresponds to pitching to stall and increases the force intensity on the blade. The collective pitch, β_{col}, is excluded hereafter

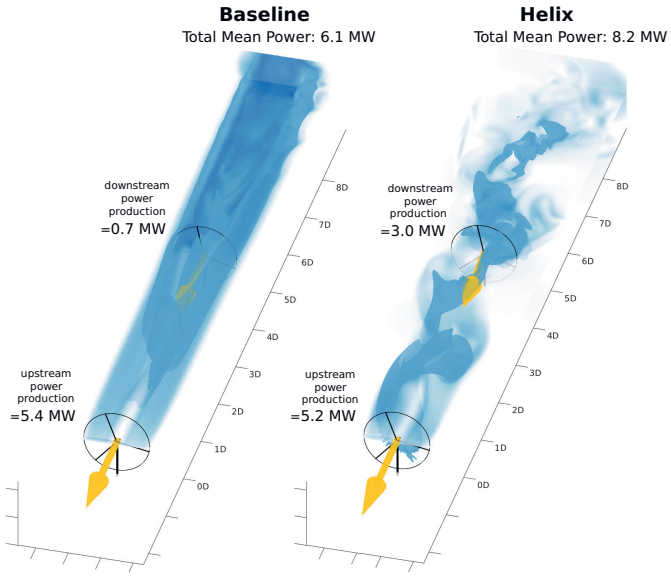

Figure 5.1: Comparison of the Helix approach (right) and the baseline case (left) in a two-turbine setup during full wake overlap, based on data from a Large-eddy simulation study in purely laminar inflow by (Frederik, Doekemeijer, *et al.* 2020). The image, adapted from (Meyers, C. Bottasso, *et al.* 2022), shows the velocity magnitude in light blue and the isosurface of velocity in dark blue. The x-axis indicates the turbine spacing normalized by the rotor diameter D. For further simulation details, please refer to the referenced works.

as it is regulated by the collective pitch controller, which adjusts the pitch angle of all blades in response to rotor speed feedback, optimizing wind turbine performance by maintaining consistent power output and rotor speed.

Although multi-sine approaches have also been explored (see Huang *et al.* 2023), here we consider the pure sine approach, so the Helix control commands for tilt and yaw are defined as follows:

$$\begin{bmatrix} \beta_{\text{tilt}} \\ \beta_{\text{yaw}} \end{bmatrix} = \begin{bmatrix} A\sin(\omega_{\text{e}} t) \\ A\sin(\omega_{\text{e}} t \pm \pi/2) \end{bmatrix}, \tag{5.2}$$

The excitation frequency $\omega_{\text{e}} = 2\pi f_{\text{e}}$ is governed by the dimensionless Strouhal number, St, calculated as:

$$\text{St} = \frac{f_{\text{e}} D}{U_\infty}, \tag{5.3}$$

where D is the rotor diameter, and U_∞ denotes the free-stream wind velocity. Previous studies recommend Strouhal numbers between 0.2 and 0.4 for optimal performance (Frederik, Doekemeijer, *et al.* 2020; Goit and Meyers 2015). The amplitude A is typically limited to a maximum of a few degrees due to practical constraints like pitch rate limitations.

The out-of-plane bending moments (M_1, M_2, M_3) can similarly be analyzed in the fixed frame. Here we use the forward MBC transformation to obtain M_{col}, M_{tilt}, M_{yaw}:

$$\begin{bmatrix} M_{\text{col}} \\ M_{\text{tilt}} \\ M_{\text{yaw}} \end{bmatrix} = \underbrace{\frac{2}{3}\begin{bmatrix} 1/2 & 1/2 & 1/2 \\ \cos(\psi_1) & \cos(\psi_2) & \cos(\psi_3) \\ \sin(\psi_1) & \sin(\psi_2) & \sin(\psi_3) \end{bmatrix}}_{T_{\text{cm}}(\psi(t))} \begin{bmatrix} M_1 \\ M_2 \\ M_3 \end{bmatrix}. \tag{5.4}$$

The sign convention is provided in Fig 5.2: positive tilt moment corresponds to an overload on the top part of the rotor, while positive yaw moment corresponds to an overload on the right part of the rotor.

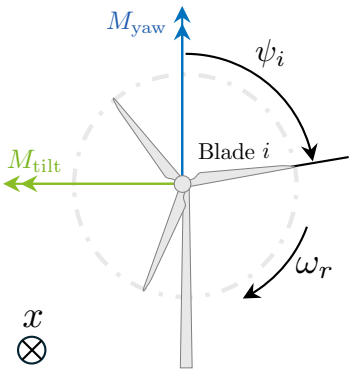

Figure 5.2: Graphic representation of blade azimuth ψ_i and associated sign convention for fixed-frame moments M_{tilt} and M_{yaw}.

Note that Eq. (5.1) and Eq. (5.4) can be used to go back and forth between the fixed and rotating domain for any blade-effective signal.

There are two variants of the Helix approach: clockwise (CW) and counter-clockwise (CCW) rotation. The CW variant is implemented by setting $-\pi/2$ in β_{yaw}, while the CCW variant uses $+\pi/2$. Although both variants maintain the same actuation frequency in the fixed frame, the effective frequency experienced by the pitch actuator differs when these commands are translated to the rotating frame, yielding:

$$\beta_i = \beta_{\text{col}} + \cos(\psi_i + \psi_{\text{o}})\beta_{\text{tilt}} + \sin(\psi_i + \psi_{\text{o}})\beta_{\text{yaw}}, \tag{5.5}$$

which leads to the Helix frequency in the rotating frame being the sum or difference of the rotor's rotational frequency ω_{r} and the excitation frequency ω_e, depending on whether the rotation is CCW or CW, respectively:

$$\begin{aligned}\beta_i &= \beta_{\text{col}} + \cos(\omega_{\text{r}} t + \psi_i^0 + \psi_{\text{o}})\beta_{\text{tilt}} \\ &\quad + \sin(\omega_{\text{r}} t + \psi_i^0 + \psi_{\text{o}})\beta_{\text{yaw}}, \\ &= A\cos(\omega_{\text{r}} t + \psi_i^0 + \psi_{\text{o}})\sin(\omega_{\text{e}} t) \\ &\quad + A\sin(\omega_{\text{r}} t + \psi_i^0 + \psi_{\text{o}})\sin(\omega_{\text{e}} t \pm \pi/2) \\ &= A\sin[(\omega_{\text{r}} \pm \omega_{\text{e}})t + \psi_i^0 + \psi_{\text{o}}],\end{aligned} \tag{5.6}$$

(5.7)

where ψ_i^0 is the azimuthal position of blade $i = 1,2,3$ at $t = 0$. Note that $\omega_e/\omega_r = \text{St}/\text{TSR}$, choosing $\text{St} \leq 0.4$ for a typical tip speed ratio (TSR) $\text{TSR} \approx 6$ ensures $\omega_e/\omega_r \leq 0.21$ and thus stays far from any low-frequency aliasing. Typically, the CCW Helix variant yields greater energy gains for the downstream turbine (Frederik, Doekemeijer, *et al.* 2020; Taschner, van Vondelen, *et al.* 2023), while the CW Helix is preferred for its reduced impact on pitch bearing wear (van Vondelen, Navalkar, Kerssemakers, *et al.* 2023), attributed to the lower effective actuation frequency of $\omega_{\text{r}} - \omega_{\text{e}}$.

The employment of the Helix approach induces periodic loading, affecting the fatigue life of the turbine performing the actuation (van Vondelen, Navalkar, Kerssemakers, *et al.* 2023). This periodic loading also extends to downstream turbines, as observed by Frederik and van Wingerden 2022, which directly results from interaction with the periodic structure in the wake induced by the upstream turbine (see Fig. 5.1). Manipulating this periodic structure in the wake by actuating the Helix approach on the downstream turbine in an in-phase/out-of-phase synchronized fashion could potentially enhance wake mixing and, thereby, power production downstream even more (Korb, Asmuth, and Ivanell 2023; van Vondelen, Pamososuryo, *et al.* 2025). Phase estimation in Helix wake mixing can be understood as an implicit wind speed estimation, as the wake's periodic structure is influenced by variations in incoming flow. To achieve this, we estimate the incoming wind speed and extract phase information of the periodic wind speed component using an estimator. One way to estimate this phase shift is through state estimation techniques, such as the extended Kalman filter, which we introduce below.

5.2.2. ESTIMATION USING THE EXTENDED KALMAN FILTER

The EKF is an extension of the Kalman Filter and is tailored for nonlinear systems. It approximates the nonlinear state and measurement models through linearization, enabling state estimation. The EKF is widely used to estimate states in systems where the relationships between variables are nonlinear, providing a means to manage the associated uncertainties effectively. This section describes how the EKF is leveraged in this work (see e.g. Chui and Chen 2017 for extensive EKF theory). First, we have a nonlinear system description:

$$\mathbf{x}_{k+1} = f(\mathbf{x}_k, \mathbf{u}_k) + \mathbf{w}_k, \tag{5.8}$$

$$\mathbf{y}_k = h(\mathbf{x}_k, \mathbf{u}_k) + \mathbf{v}_k, \tag{5.9}$$

where $\mathbf{x}_k$ is the state vector, $\mathbf{u}_k$ is the control input vector, $\mathbf{y}_k$ is the measurement vector, $\mathbf{w}_k$ is the process noise vector, and $\mathbf{v}_k$ is the measurement noise vector. The functions

$f(\cdot)$ and $h(\cdot)$ are the state and measurement functions, respectively. Let us now tailor this general representation for our application. A distinction can be made between controllable and uncontrollable inputs:

$$\mathbf{u}_k = \begin{bmatrix} \mathbf{u}_k^{\mathrm{c}} \\ \mathbf{u}_k^{\mathrm{u}} \end{bmatrix}, \tag{5.10}$$

where $\mathbf{u}_k^{\mathrm{c}}$ is the input vector containing *controllable* inputs, which are the pitch control inputs in our case, and $\mathbf{u}_k^{\mathrm{u}}$ is the input vector containing *uncontrollable* inputs, which is the incoming periodic Helix wake impinging on the downstream turbine. The goal is to estimate the unknown uncontrollable input vector $\mathbf{u}_k^{\mathrm{u}}$ by treating it as the state to be estimated. This can be achieved by assuming the following model representation (see e.g. Verhaegen and Verdult 2007):

$$\mathbf{u}_{k+1}^{\mathrm{u}} = \mathbf{u}_k^{\mathrm{u}} + \mathbf{w}_k^{\mathrm{u}}, \tag{5.11}$$

commonly known as the random walk model. Note that this model can only be assumed for biases or slowly varying states, which is a reasonable assumption in our application as we estimate constant parameters that define a sinusoid (treated in Section 5.2.3). In the case of a periodic state, an undamped oscillator may be a more suitable model (van Vondelen, Ottenheym, Pamososuryo, *et al.* 2023). The state-space system becomes:

$$\underbrace{\begin{bmatrix} \mathbf{x}_{k+1} \\ \mathbf{u}_{k+1}^{\mathrm{u}} \end{bmatrix}}_{\mathbf{x}_{k+1}^{\mathrm{aug}}} = \begin{bmatrix} f(\mathbf{x}_k,\, \mathbf{u}_k^{\mathrm{u}},\, \mathbf{u}_k^{\mathrm{c}}) + \mathbf{w}_k \\ \mathbf{u}_k^{\mathrm{u}} + \mathbf{w}_k^{\mathrm{u}} \end{bmatrix}, \tag{5.12}$$

$$\mathbf{y}_k = h(\mathbf{u}_k^{\mathrm{u}}, \mathbf{u}_k^{\mathrm{c}}) + \mathbf{v}_k. \tag{5.13}$$

Using an EKF, it is now possible to estimate the uncontrollable input vector $\mathbf{u}_k^{\mathrm{u}}$. The measurement function $h(\mathbf{u}_k^{\mathrm{u}}, \mathbf{u}_k^{\mathrm{c}})$ is chosen to be the dynBEM model which computes the blade out-of-plane loads based on blade-effective wind speeds (BEWS), rotor velocity, and pitch angle in the rotating (blade) coordinate frame. It represents a nonlinear measurement mapping dependent on both the controllable and uncontrollable inputs. In practice, $h(\cdot)$ first uses the estimated amplitude and phase to generate the fixed-frame periodic wind perturbations,

$$U_{\mathrm{tilt}} = A_{\mathrm{helix}} \sin(\omega_{\mathrm{e}} t + \varphi_{\mathrm{tilt}}), \quad U_{\mathrm{yaw}} = A_{\mathrm{helix}} \cos(\omega_{\mathrm{e}} t + \varphi_{\mathrm{yaw}}),$$

and then maps these through the backward MBC transform and dynBEM to predict blade loads, thereby embedding both the oscillatory wake model and the turbine dynamics into the measurement. Note that the actual system state equation is unknown, and dynBEM does not depend on it; the dynamics are modeled according to the engineering model of Snel and Schepers 1995. Since we are only interested in estimating $\mathbf{u}_k^{\mathrm{u}}$, we can formulate the EKF problem as follows:

$$\hat{\mathbf{u}}_{k+1}^{\mathrm{u}} = \hat{\mathbf{u}}_k^{\mathrm{u}} + K_k \mathbf{e}_k, \tag{5.14}$$

$$\mathbf{e}_k = \mathbf{y}_k - h(\hat{\mathbf{u}}_k^{\mathrm{u}}, \mathbf{u}_k^{\mathrm{c}}), \tag{5.15}$$

where $\hat{(\cdot)}$ denotes an estimate, K_k is the Kalman gain, and $\mathbf{e}_k$ is the innovation signal vector.

BEWS represents the local wind speed experienced by each blade as it rotates through the wake-affected flow field. Unlike freestream wind speed, BEWS accounts for variations due to wake dynamics, turbulence, and aerodynamic interactions.

Next to the above-mentioned turbine signals, dynBEM requires system parameters such as the rotor radius, hub radius, and airfoils (see Coquelet, Lejeune, *et al.* 2024 for additional details on using dynBEM in a wind speed estimator).

To calculate the Kalman gain, it is assumed that estimates of the covariance matrices of $\mathbf{w}_k$ and $\mathbf{v}_k$ are available:

$$E\left[\begin{bmatrix}\mathbf{w}_k\\ \mathbf{v}_k\end{bmatrix}\begin{bmatrix}\mathbf{w}_k^T & \mathbf{v}_k^T\end{bmatrix}\right] = \begin{bmatrix}Q & S^T\\ S & R\end{bmatrix} \geq 0, \tag{5.16}$$

where Q and R are the covariance matrices of $\mathbf{w}_k$ and $\mathbf{v}_k$, respectively, S is their cross-covariance, and the matrix is assumed to be positive semi-definite.

The state transition matrix F_k is the identity matrix based on the definition of the state equation (Eq. (5.14)), simplifying the covariance propagation. Additionally, the process noise $\mathbf{w}_k$ and measurement noise $\mathbf{v}_k$ are assumed to be uncorrelated, allowing the cross-covariance term S to be neglected. This assumption is valid given the independent nature of the noise sources in the system.

The Kalman gain is then obtained by first propagating the Riccati difference equation:

$$P_{k+1} = P_k + Q - K_k P_k {H_k^{\mathrm{u}}}^T, \tag{5.17}$$

where P_k is the covariance matrix estimate, and H_k^{u} is the Jacobian of the measurement function h with respect to $\mathbf{u}^{\mathrm{u}}$.

Note that we do not have a differentiable nonlinear expression for the measurement function (Eq. (5.13)). As such, the Jacobian H_k^{u} is approximated by central differences, given that $h(\cdot)$ is a nonlinear function:

$$H_k^{\mathrm{u}} \approx \frac{h(\hat{\mathbf{u}}_k^{\mathrm{u}} + \mathrm{d}n/2, \mathbf{u}_k^{\mathrm{c}}) - h(\hat{\mathbf{u}}_k^{\mathrm{u}} - \mathrm{d}n/2, \mathbf{u}_k^{\mathrm{c}})}{\mathrm{d}n}, \tag{5.18}$$

where $\mathrm{d}n$ is a small deviation from the operating point. The choice of $\mathrm{d}n$ requires balancing truncation and round-off errors. Typically, $\mathrm{d}n$ should be small relative to u_k, often in the range of 10^{-5} to 10^{-2} times u_k, ensuring numerical accuracy without excessive sensitivity to floating-point precision. The chosen value in our setup is $\mathrm{d}n = 1 \times 10^{-5}$ rad. This value was selected empirically based on implementation testing. It offered the most stable and accurate performance among the values tried. Given that the control input amplitude is approximately 0.07 rad (4 degrees), this perturbation corresponds to about 0.014% of the signal magnitude, small enough to remain in the linear regime while avoiding round-off errors.

Finally, the Kalman gain is calculated as:

$$K_k = P_k {H_k^{\mathrm{u}}}^T (R + H_k^{\mathrm{u}} P_k {H_k^{\mathrm{u}}}^T)^{-1}. \tag{5.19}$$

The Kalman gain K_k and error covariance P_k generally converge to steady-state values under constant wind conditions. However, in realistic wind farm environments, wind

speed variations and turbulence influence the uncertainty in phase estimation, requiring K_k to adapt dynamically. The EKF inherently provides some adaptivity by updating state estimates in real time, but further improvements can be achieved by tuning the process noise Q and measurement noise R based on observed wind conditions, which is discussed in Section 5.2.5. The next section presents the parameterization of the Helix wake used in the EKF.

5.2.3. STATE VECTOR: HELIX WAKE REPRESENTATION

As described in Section 5.2.1, the Helix wake is generated by periodic control actions applied to an upstream turbine (T1). While the fluid dynamics phenomena relating the actuation and the shape of the wake remain an active area of research (Coquelet, Gutknecht, *et al.* 2024; Korb, Asmuth, and Ivanell 2023), a consensus is that the Helix wake propagates following a helical shape (see Fig. 5.1). From a downstream turbine (T2) perspective, this implies that the incoming wind field consists of a wake deficit that is misaligned from the rotor center and rotates around it over time. This can be modeled as wind speed changes in the tilt and yaw directions. To capture this behavior, the wake is then represented as a U_{tilt} and U_{yaw} sine-like perturbation. The frequency of these perturbations is assumed equal to that of the periodic control input applied at the upstream turbine.

This assumption on the frequency content is supported by Fig 5.3, which shows U_{col}, U_{tilt} and U_{yaw} extracted from the velocity field at 5D behind a single turbine for a Helix and a baseline case. How U_{tilt} and U_{yaw} are retrieved from the slice of velocity is presented in Section 5.3.3. A clear peak at the Helix frequency can be observed, further suggesting that the Helix-induced wake structure, while subject to turbulent mixing, retains a coherent oscillatory pattern as it travels through the wind farm (Frederik and van Wingerden 2022; van Vondelen, Pamososuryo, *et al.* 2025).

The model for the wind speed U at a downstream turbine T2 is then expressed as:

$$\begin{bmatrix} U_{\text{col}} \\ U_{\text{tilt}} \\ U_{\text{yaw}} \end{bmatrix} = \begin{bmatrix} A_{\text{col}} \\ A_{\text{helix}} \sin(\omega_{\text{e}} t + \varphi_{\text{tilt}}) \\ A_{\text{helix}} \cos(\omega_{\text{e}} t + \varphi_{\text{yaw}}) \end{bmatrix}, \tag{5.20}$$

where A_{col} represents the collective wind speed component, and A_{helix} is the amplitude of the periodic components of the Helix wake. The collective amplitude A_{col} therefore represents the mean wind speed over the rotor swept area. The sign convention and physical meaning of U_{tilt} and U_{yaw} are similar to those of the rotor moments: a positive U_{tilt} corresponds to an over-speed on the top part of the rotor (naturally causing a positive tilt moment if no individual pitch control (IPC) command is applied on T2), while positive U_{yaw} corresponds to an over-speed in the right part of the rotor (naturally causing a positive tilt moment if no IPC command is applied on T2). The parameters φ_{tilt} and φ_{yaw} represent the phase shifts between the tilt and yaw actuation on T1 and the tilt and yaw wind speed perturbation of the wake impinging on T2 (see Fig. 5.6). If the wake propagated as a perfect helix, these parameters would be identical. As distortion happens as the wake propagates downstream, an additional degree of freedom is given to the model by considering distinct values for these offsets in the tilt and yaw direction.

These phase shifts are the main parameters of interest as they influence the alignment of the wake structures with downstream turbines.

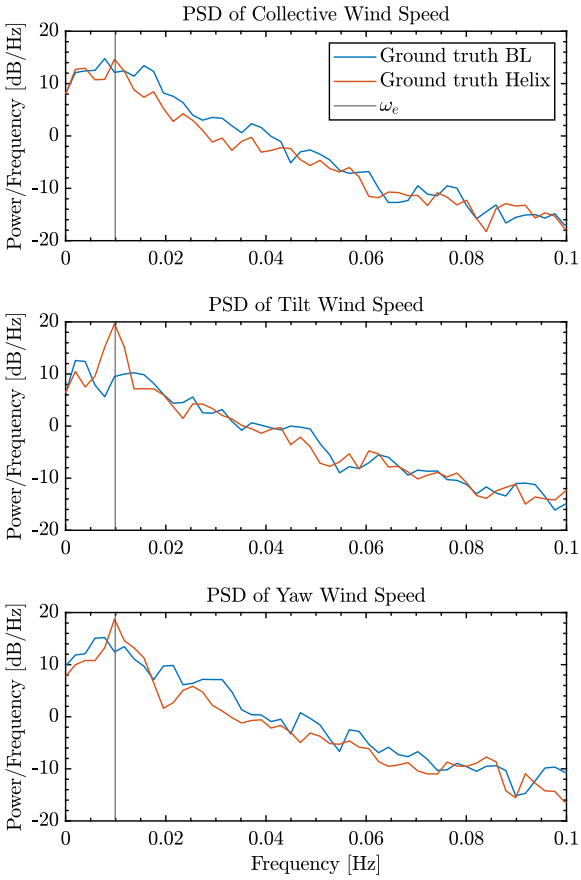

Figure 5.3: Power spectral density comparison at 5D downstream from a turbine using Baseline control (blue) and Helix control (red). The Helix wake shows a distinct peak at the excitation frequency f_e (black line), confirming the periodic nature of the wake. This periodicity is required for phase estimation and synchronization in downstream turbines.

The purpose of the estimator is then to estimate the parameters of the model described by Eq. 5.20, and the following state vector is employed:

$$\mathbf{u}_k^u = \begin{bmatrix} A_{\text{col}} \\ A_{\text{helix}} \\ \varphi_{\text{tilt}} \\ \varphi_{\text{yaw}} \end{bmatrix}. \tag{5.21}$$

This state vector captures both the amplitude and phase information necessary to de-

scribe the wind speed components at the downstream turbine. Given that these parameters are typically constant under steady operating conditions, they are modeled as random walks in the estimation process. This approach allows for capturing slow variations in the wake characteristics due to changing environmental conditions or turbine dynamics.

By directly estimating the phase shifts $\hat{\varphi}_{\text{tilt}}$ and $\hat{\varphi}_{\text{yaw}}$ from the observed wind speed data, the model provides the necessary information for downstream synchronization control. The next section presents how we tune the EKF internal model, i.e. the measurement function.

5.2.4. EKF INTERNAL MODEL SPECIFICATIONS AND TUNING

In the estimation procedure, the state vector $\mathbf{u}_k^u$ is used by the EKF internal model through the measurement function h (see Eq. 5.13). As mentioned in Section 5.2.2, this work relies on the BEM theory (Coquelet, Lejeune, *et al.* 2024), which computes the blade out-of-plane loads based on BEWS, rotor velocity, and pitch angle in the rotating (blade) coordinate frame. The state vector therefore needs to be adapted to fit the required inputs of the BEM, i.e. BEWS. The state vector is used in Eq. 5.20 to provide the vector of wind speed perturbation in the rotor frame, consisting of U_{col}, U_{tilt} and U_{yaw}. This vector is then mapped onto the rotating frame using the backward MBC transform defined in Eq. (5.1), eventually leading to BEWS that are usable by the BEM model (see Fig. 5.7 for the illustration of the flow of information in the estimation process).

Wind turbine models like the BEM can capture the essential dynamics of the system; however, delays can still occur due to factors like actuator response time, induced velocities reaction time, or blade flexibility. To treat these delays, this work combines two approaches given in the literature.

On the first hand, the pitch response delays are accounted for using an optimal azimuth offset to be used in the backward MBC transform (Eq. 5.1) (Mulders *et al.* 2019). This ensures that the pitch angle fed to BEM is the actual blade pitch angle and not the pitch command. Identifying the optimal azimuthal offset is typically done using the relative gain array (RGA) of a linearized system model, and can depend on the simulation tool, as the delays reflect unmodeled dynamics. van Vondelen, Pamososuryo, *et al.* 2024 proposed a method for directly identifying the optimal azimuth offset within the simulation environment through system identification. Using that methodology, we identified the optimal azimuth offset of $\phi_{\text{off}} = 17°$ for our scenario. Note that this offset is highly model-dependent and should be determined for each specific wind turbine model and/or configuration.

On the other hand, we account for the aerodynamic delays appearing between the pitch angle changes and the blade forces response using a dynamic version of the BEM. It was indeed shown in Coquelet, Lejeune, *et al.* 2024 that dynamic effects appear in the local inductions computed at the blade due to the Helix pitch. Those are not modeled by the standard BEM model as the BEM theory considers steady operation.

Figure 5.4 demonstrates the effect of these two corrections of this optimal azimuth offset on the blade root moments computed using the BEM and compared to a reference LES consisting of an upstream turbine operating the Helix in a laminar inflow. The figure compares:

- the standard BEM output when the pitch values are the actual pitch angles (Eq. 5.1 with optimal azimuth offset),
- the dynBEM output when the pitch values are identical to the pitch commands (Eq. 5.1 with no azimuth offset),
- the dynBEM output when the pitch values are the actual pitch angles following the actuator response (Eq. 5.1 with optimal azimuth offset).

The figure shows that incorporating the optimal azimuth offset significantly improves the alignment between the model output and actual measurements. Additionally, the dynBEM model, which can be tuned with a single parameter, shows a closer match to the LES data compared to the static BEM model, indicating its superior ability to capture dynamic effects. The next section describes the tuning of the noise covariance matrices.

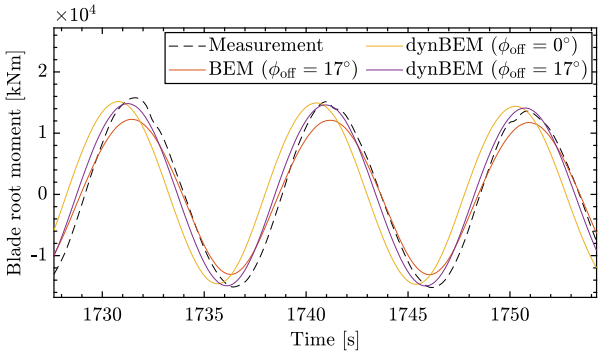

Figure 5.4: Blade root moments comparison with and without optimal azimuth offset ϕ_{off} using the static BEM and dynamic BEM models, highlighting the improved match of the dynBEM model with azimuth offset to LES data.

5.2.5. EKF NOISE PARAMETERS TUNING

The EKF relies on accurately defined process noise (Q) and measurement noise (R) covariance matrices, which are often challenging to estimate accurately. This section presents methodologies for tuning these matrices, starting with estimating the R matrix.

The process begins by selecting a frequency band of interest for the system's dynamics, treating frequencies outside this band as noise components (see Fig. 5.5). We employ a high-pass filter on the signal to isolate this noise, extracting the high-frequency components (see Fig.5.5. The filter was configured to isolate the Helix control frequency, while suppressing higher-frequency dynamics such as the 0.3 Hz component, which are not used in the estimator and may introduce bias. We employ a high-pass filter on the signal to isolate these parts, extracting the high-frequency components. The variance of this filtered output is then adopted as the entries of the R matrix.

The estimation of the Q matrix involves more nuanced steps. Initially, the Helix wind speed component is determined from the ground truth wind speed data (details on the

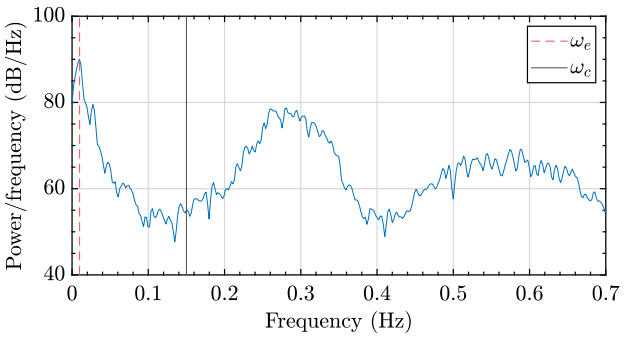

Figure 5.5: Power spectrum analysis of M_{tilt}: Determining the measurement noise covariance matrix (R). The Helix frequency is highlighted with a red dashed line, and the cut-off frequency ω_c is denoted by the black line.

ground truth provided in Sections 5.3.3 and 5.4.1) using a low-pass filter. This ensures that only the frequencies contributing significantly to the signal's behavior are considered. After filtering, the amplitude and phase shift of the wind speed are computed, forming the basis for the Q matrix selection. Specifically, the Q matrix is set as the variance of the derivative of these filtered signals, providing a measure of process noise. In real-world conditions, actual wind speed measurements and similar post-processing could provide an initial value for the Q matrix.

After the initial estimates, the Q matrix requires further refinement to enhance the EKF's performance. This is achieved through iterative tuning, where the matrix is scaled by a constant factor based on the observed performance of the filter in simulation trials. This iterative process continues until the EKF's performance aligns with the desired accuracy and reliability criteria. The pseudo-code in Alg. 1 summarizes the tuning process.

To enhance the accuracy and robustness of the proposed EKF-based synchronization method, real-time calibration can be a suitable addition. This approach involves dynamically adjusting the estimator's parameters to respond to changing environmental conditions and operational dynamics (Mehra 1970). One critical aspect of real-time calibration is the adaptive adjustment of the process noise (Q) and measurement noise (R) covariance matrices within the EKF. These matrices, initially set during offline tuning according to Alg. 1, may not fully capture the complexities of real-world conditions, where wind speeds, turbulence, and atmospheric stability can vary significantly. By continuously monitoring the estimator's performance, particularly through the innovation sequence (the difference between predicted and actual measurements, Eq. (5.15)), the system can detect when the current noise assumptions are inadequate. For instance, during periods of high turbulence, increasing the process noise covariance can account for greater uncertainty in wind speed estimates, leading to more accurate control actions. However, this is out of the scope of the current work. The next section presents the phase synchronization controller.

Algorithm 1 Tuning the EKF Covariance Matrices

1: **Input:** Raw signal data from the wind turbine
2: **Output:** Optimized Q and R matrices for the EKF
3: **Step 1: Estimate Measurement Noise Covariance (R)**

1. Identify the frequency band of interest in the signal (around ω_e in our case).
2. Apply a high-pass filter to isolate high-frequency noise (see Fig. 5.5).
3. Compute the variance of the filtered signal.
4. Set the R matrix to this computed variance.

4: **Step 2: Estimate Process Noise Covariance (Q)**

1. Apply a low-pass filter to the ground truth wind speed signal to isolate the Helix component.
2. Calculate the amplitude and phase shift of the filtered signal.
3. Compute the variance of the derivative of these filtered signals.
4. Set the Q matrix to this computed variance.

5: **Step 3: Fine-Tune Q Matrix**

1. Initialize the EKF with the estimated Q matrix.
2. **while** EKF performance is unsatisfactory **do**
   a) Scale the Q matrix by a constant factor.
   b) Re-run the EKF and assess performance against validation data.
   c) Adjust the scaling factor as necessary.
3. **end while**

5.2.6. PHASE SYNCHRONIZATION CONTROLLER DESIGN

The synchronization controller is designed to align the control actions of downstream turbines with the phase of the incoming wake generated by upstream turbines. It utilizes phase estimates provided by the EKF, which tracks the phase shifts $\hat{\varphi}_{\text{tilt}}$ and $\hat{\varphi}_{\text{yaw}}$ of the incoming wake as described in the previous section. Based on these estimates, the controller adjusts the tilt and yaw control signals of the downstream turbines. The control signals are expressed as:

$$\begin{bmatrix} \beta_{\text{tilt}} \\ \beta_{\text{yaw}} \end{bmatrix} = \begin{bmatrix} A\sin(\omega_{\text{e}} t + \hat{\varphi}_{\text{tilt}} + \varphi_{\text{off}}) \\ A\sin(\omega_{\text{e}} t \pm \pi/2 + \hat{\varphi}_{\text{yaw}} + \varphi_{\text{off}}) \end{bmatrix}, \tag{5.22}$$

where A_{T2} is the downstream turbine's amplitude, ω_{e} is the excitation frequency, and φ_{off} is an additional phase shift that can be applied to modify the alignment of the up- and downstream Helix wakes. Note that the amplitude can differ from the upstream amplitude, and all pitch commands are fed through ROSCO's (Abbas, D. Zalkind, *et al.* 2022) pitch rate limiter to prevent actuator saturation. A graphical representation of the synchronization is provided in Fig. 5.6. The phase offset is defined such that

- $\varphi_{\text{off}} = 0$ indicates that the pitch is in phase with the wind speed perturbation (see Eq. 5.20): the blade pitch increases as a blade travels through the area of higher wind speed, hence the blade forces are locally reduced compared to a case where IPC is not active;
- $\varphi_{\text{off}} = 180^\circ$ indicates that the pitch is out-of-phase with the wind speed perturbation (see Eq. 5.20): the blade pitch decreases as a blade travels through the area of higher wind speed, hence the blade forces are locally increased compared to a case where IPC is not active.

The adjusted control signals are then implemented by the downstream turbine's pitch system (Eq. (5.1)), which alters the rotor's tilt and yaw to create a controlled wake. The overall process is focused on achieving a precise phase offset between the downstream turbine's control actions and the incoming wake, using the EKF-derived phase information to inform these adjustments. A schematic of the entire framework, including the proposed estimator and control strategy is given in Fig. 5.7. The next section will present the framework used for evaluating the proposed method.

5.3. HIGH-FIDELITY SIMULATION FRAMEWORK

This section outlines the simulation framework and configurations employed to evaluate the performance of the novel synchronization controller using the high-fidelity simulation tools OpenFAST (B. Jonkman, Platt, *et al.* 2024) and AMR-Wind (Brazell *et al.* 2021). These tools are integrated to simulate complex wake interactions between wind turbines under realistic atmospheric conditions.

5.3.1. LARGE-EDDY SIMULATION ENVIRONMENT

The Large-eddy simulations are performed with the AMR-Wind software, which is well suited for the study of wind farms in atmospheric boundary layer flows Brazell *et al.* 2021.

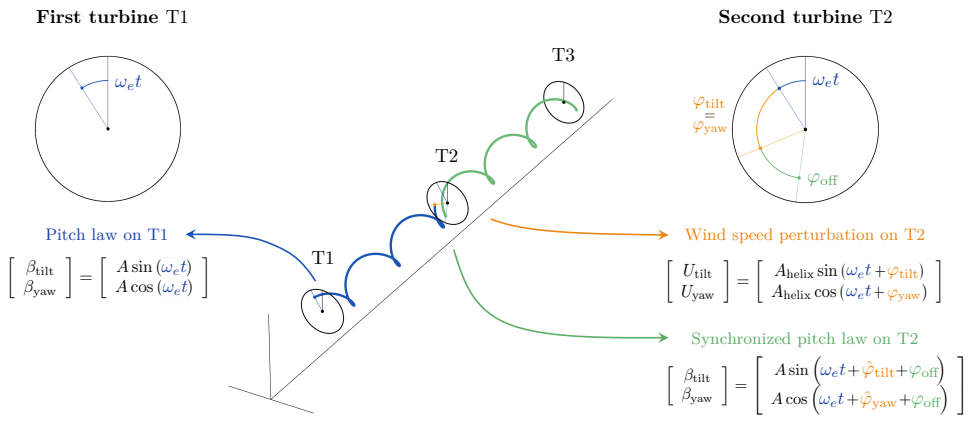

Figure 5.6: Graphical representation of the phase synchronization controller. The control action on T2 is based on the estimated phase shift of the incoming Helix wake $\hat{\varphi}_{\text{tilt}}$ and $\hat{\varphi}_{\text{yaw}}$, and a user-defined phase offset φ_{off}. Note that in this figure, the CCW Helix is illustrated.

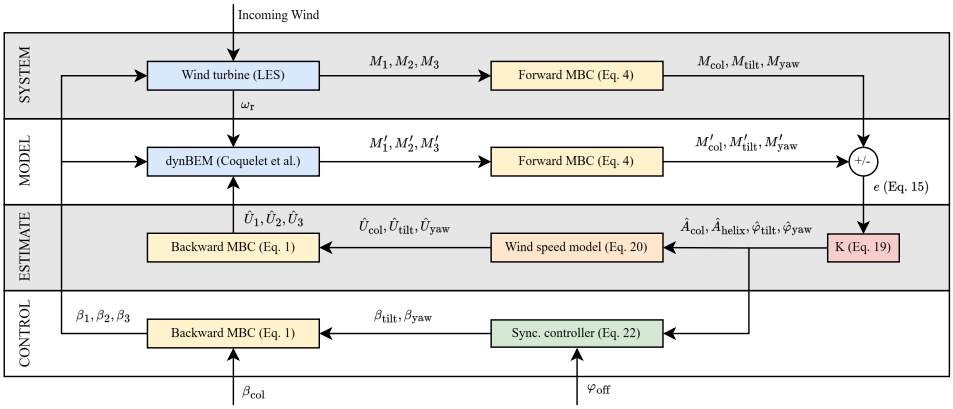

Figure 5.7: Schematic of the synchronized Helix wake mixing control framework illustrating the flow of information. The figure illustrates the integration of the wind turbine, EKF, dynBEM, and synchronization controller. Note that the model outputs are distinguished from the system outputs with an apostrophe. U_i, where $i = 1,2,3$, are the blade-effective wind speeds after transforming to the rotating reference frame.

The simulation employs a Convective Boundary Layer (CNBL) setup that includes Coriolis effects to replicate a stable stratified atmosphere interacting with the wind turbines. This setup is similar to the one used in Taschner, van Vondelen, *et al.* 2023 and identical to the one used in van Vondelen, Pamososuryo, *et al.* 2025.

The precursor simulation is performed with a domain of dimensions 5360 m in the x-direction, 3200 m in the y-direction, and 1600 m in the z-direction. An isotropic grid size of 10 m is used, complying with CNBL requirements (Wurps, Steinfeld, and Heinz 2020). Periodic boundary conditions allow the flow to evolve over 16 hours, achieving a quasi-stationary turbulent ABL state (Zilitinkevich, Esau, and Baklanov 2007), where the wind speed at hub height U_{hub} of the first turbine is forced to be 10.5 m/s and the turbulence intensity TI_{hub} is around 5 %. The vertical profile of the streamwise velocity, along with the lateral veer and turbulence intensity, is shown in Fig. 5.8. These inflow characteristics result in veered and vertically sheared wakes, contributing to a more realistic simulation environment.

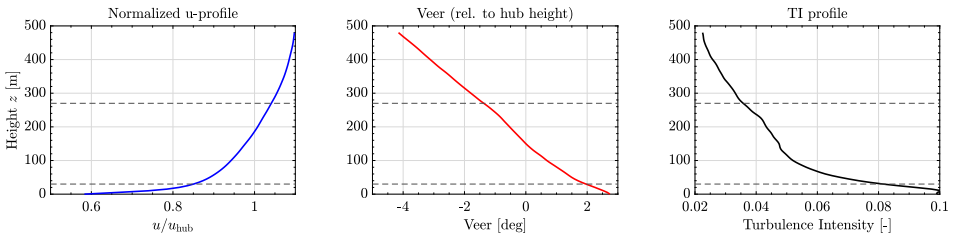

Figure 5.8: Time-averaged inflow characteristics at a sampling plane 2D upstream, extracted over a duration of 2100 s. (Left) Normalized streamwise velocity profile u/u_{hub}, indicating the vertical shear of the inflow. (Middle) Lateral veer angle in degrees, relative to the hub height, highlighting directional shear across the rotor span. (Right) Turbulence intensity (TI) profile computed from the standard deviation of the streamwise velocity, characterizing inflow unsteadiness relevant for load analysis. The dashed lines indicate the top and bottom of the rotor.

After this initial phase, y-z planes at the inflow boundary ($x = 0$ m) are sampled for 45 minutes at a frequency of 1 Hz to serve as inflow conditions for turbine simulations. For these simulations, the domain and boundary conditions remain identical to those used in the precursor run. The turbine blades are modeled using the Actuator Line Method (ALM) coupled with OpenFAST.

The ALM setup includes 60 actuator points per blade and 72 points for the tower. Turbines are operating around a tip-speed ratio of 9.3. The OpenFAST simulations are restarted from a converged precursor checkpoint and advanced synchronously with the LES, using a fixed time step of 0.05 s. Inflow planes extracted at 1Hz ensure that the dominant Helix excitation is well-resolved.

The turbines, which are modeled by OpenFAST (see next section), are placed within the domain at coordinates (x = 1200 m, y = 1600 m) for turbine 1 (T1), (x = 2400 m, y = 1600 m) for turbine 2 (T2), and (x = 3600 m, y = 1600 m) for turbine 3 (T3). This corresponds to a $5D$ spacing, where D represents the rotor diameter (see Table 5.1), from the inflow and between the turbines, and also sufficient space for wake development behind the third turbine.

To facilitate higher-resolution flow analysis around the wind turbines, a mesh refinement to 5 m is implemented. This refinement covers a static box area starting $4.5D$ up-

stream of the first turbine, with dimensions of 5040 m in the x-direction, 960 m in the y-direction, and 600 m in the z-direction. The upstream extension ensures accurate resolution of incoming turbulence and shear from the inflow boundary, providing well-resolved conditions at the rotor plane for synchronization analysis.

Coriolis effects are included via the CNBL setup, using a latitude of 52.6°, corresponding to a Coriolis frequency of approximately 1.3×10^{-4} s^{-1}.

5.3.2. WIND TURBINE SIMULATION TOOL

The turbine is modeled by the OpenFAST solver, which serves as a comprehensive multi-fidelity simulation tool by integrating various modules focused on structural dynamics, aerodynamics, and control systems. The simulation setup for this study employs the International Energy Agency's (IEA) 15 MW fixed-bottom reference wind turbine (specifics in Table 5.1) (Gaertner *et al.* 2020). The proposed method is implemented in an external Python script that computes pitch control setpoints in real time. These setpoints are then transmitted to ROSCO during runtime via ZeroMQ, a lightweight messaging library for high-performance asynchronous communication (Hintjens 2013).

In the LES-coupled simulation environment, the turbine blades are represented via the Actuator Line Method (ALM), where each blade segment exerts dynamic forces on the surrounding air, thereby influencing local flow properties such as velocity and turbulence (J. N. Sørensen and Shen 2002). The interaction between OpenFAST's fine temporal resolution and the coarser LES grid in AMR-Wind necessitates sophisticated interpolation techniques and phase adjustments to ensure accurate and timely controller responses.

Table 5.1: Specifications of the IEA 15 MW reference turbine used in the simulations.

Characteristic	**Value**
Hub height	150 m
Rotor diameter	240 m
Rated power	15 MW
Rated wind speed	10.59 m/s
Cut-in wind speed	3 m/s
Cut-out wind speed	25 m/s
Min. rotor speed	5 rpm
Max. rotor speed	7.56 rpm

5.3.3. SIMULATION CASES

This section introduces the simulation cases designed to validate the proposed estimator and evaluate the control strategy. It starts by detailing the methodology for obtaining the ground truth, followed by an overview of the synchronization cases, including a summary of the simulation setups and the performance metrics used for evaluation.

GROUND TRUTH FOR ESTIMATOR VALIDATION

A ground truth is required for validating wind estimates from the proposed controller. The ground truth is generated through an LES involving only the first turbine (T1) in the array, capturing wind conditions unaffected by downstream turbines. This scenario establishes a baseline for comparing wind speed estimates derived from T2's blade loads.

Wind velocity data are sampled 5D downstream of T1, aligning with the location of T2 in synchronization cases. The sampling process involves:

- Sampling n lines originating from the rotor center across the flow field located at azimuthal positions $\psi_{L,1},\dots,\psi_{L,n}$ (see Fig. 5.9);
- Averaging wind speed along these lines over time to obtain line-effective wind speeds $U_{L,1},\dots,U_{L,n}$;
- Mapping the line-effective wind speeds to fixed-frame to obtain U_{col}, U_{tilt}, and U_{yaw} using the MBC transform generalized for n lines proposed in Moens *et al.* 2022:

$$\begin{bmatrix} U_{\text{col}} \\ U_{\text{tilt}} \\ U_{\text{yaw}} \end{bmatrix}^{\text{GT}} = \frac{2}{n} \begin{bmatrix} 1/2 & \dots & 1/2 \\ \cos(\psi_{L,1}) & \dots & \cos(\psi_{L,n}) \\ \sin(\psi_{L,1}) & \dots & \sin(\psi_{L,n}) \end{bmatrix} \begin{bmatrix} U_{L,1} \\ \vdots \\ U_{L,n} \end{bmatrix}. \tag{5.23}$$

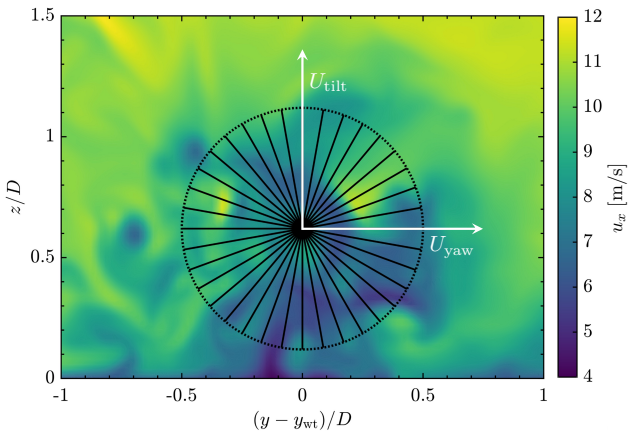

Figure 5.9: Sampling methodology for estimating blade-effective wind speeds from the LES flow field. The average wind speed on thirty-six lines is mapped to the tilt and yaw axes to derive the effective wind speed at 5D downstream in the fixed coordinate frame.

The number of lines is set to $n = 36$ in this case. A band-pass filter is applied to the fixed-frame wind speeds to isolate the Helix component. The resulting tilt and yaw wind signals are narrow-band and spatially averaged, leading to clean harmonic components. Applying the Hilbert transform to these filtered signals yields a smooth and consistent

phase trace, suitable as a ground truth reference. A pseudo-code showing the full procedure is given in Alg. 2. These processed data serve as a benchmark for validating the estimator in simulations with multiple turbines, facilitating the tuning of the EKF. Note that this bandpass filter is not applied on the signals shown in Fig. 5.3.

Algorithm 2 Ground Truth Wind Estimation from LES

1: **Input:** LES velocity field with only T1 present; sampling distance $5D$ behind T1.
2: **Output:** Fixed-frame wind signals $U_{\text{col}}(t)$, $U_{\text{tilt}}(t)$, $U_{\text{yaw}}(t)$
3: **Step 1: Define Sampling Geometry**

1. Set the number of sampling lines n.
2. Define azimuthal angles $\psi_{L,1}, \ldots, \psi_{L,n}$ uniformly around the rotor disk center of T2.
3. For each $\psi_{L,i}$, define a line extending radially outward from the rotor center at 5D downstream (see Fig. 5.9).

4: **Step 2: Compute Line-Averaged Velocities**

1. For each time step t and each line $i = 1$ to n:
   a) Sample the LES wind velocity $U_{\text{line},i}(t, s)$ along the spatial coordinate s.
   b) Average along s to obtain $U_{L,i}(t) = \text{mean}_s(U_{\text{line},i}(t, s))$.

5: **Step 3: Apply Generalized Coleman Transform**

1. For each time step t, compute:

$$U_{\text{col}}(t) \leftarrow \frac{1}{n} \sum_{i=1}^{n} U_{L,i}(t)$$

$$U_{\text{tilt}}(t) \leftarrow \frac{2}{n} \sum_{i=1}^{n} U_{L,i}(t) \cos(\psi_{L,i})$$

$$U_{\text{yaw}}(t) \leftarrow \frac{2}{n} \sum_{i=1}^{n} U_{L,i}(t) \sin(\psi_{L,i})$$

2. Store the resulting signals as the time series ground truth.

6: **Step 4: Isolate Helix Component**

1. Apply a band-pass filter to $U_{\text{tilt}}(t)$ and $U_{\text{yaw}}(t)$ (cutoff chosen ≈ 0.15 Hz to capture the Helix frequency).
2. Retain $U_{\text{col}}(t)$ unfiltered.

7: **Return** $U_{\text{col}}(t)$, $U_{\text{tilt}}(t)$, $U_{\text{yaw}}(t)$

SYNCHRONIZATION CASES

The synchronization cases evaluate the performance of the EKF-based phase synchronization control strategy. The simulations consist of three turbines (T1, T2, and T3) arranged linearly with 5D spacing. Realistic inflow conditions are generated using a precursor LES (see Section 5.3).

Control strategies for the turbines are as follows:

- **T1:** Operates under Helix control in all cases.
- **T2:** Applies either baseline control or synchronized phase control depending on the scenario.
- **T3:** Always operates under baseline control to isolate the impact of upstream control strategies.

The primary objective is to explore the influence of different phase shift offsets (φ_{off}) in T2's control on downstream power production and structural loads.

CASES SUMMARY

Ten distinct simulation cases are defined, as summarized in Table 5.2:

1. **T1 Only (Helix):** T1 employs Helix control, with T2 and T3 absent. This serves as the baseline for wake development and ground truth sampling (see Section 5.3.3).
2. **BL Helix:** T2 and T3 apply baseline control, while T1 operates with Helix control. This case serves as a reference for the synchronization evaluations.
3. **Synchronization Cases ($\varphi_{\text{off}} = 0^\circ - 270^\circ$):** T2 applies synchronized Helix control with phase shifts of $0^\circ, 90^\circ, 180^\circ$, and 270°.
4. **Additional Phase Shifts:** Further cases with phase shifts of $120^\circ, 150^\circ, 210^\circ$, and 330° refine the optimal phase offset analysis.

Each case has a total simulation time of 2700 seconds, where during the first 600 seconds T2 operates using BL control such that the Helix wake from T1 can propagate through the domain. At $t = 600$ s, the synchronization controller is activated on T2.

Simulations were executed on the Dutch national high-performance computing system Snellius (SURF 2024), utilizing 512 cores and consuming 24k CPU hours per simulation.

QUANTITIES OF INTEREST

The performance metrics for evaluating the synchronization strategies are listed below:

Estimator Performance Metrics

- **Root Mean Square Error (RMSE):** Evaluates the deviation between estimated and ground truth phase shifts for tilt and yaw components, indicating estimation accuracy.

Table 5.2: Overview of simulation cases. The final four cases are additional to determine the optimal phase offset.

Case	T1	T2	T3
T1 Only (Helix)	Helix	-	-
BL Helix	Helix	BL	BL
$\varphi_{\text{off}} = 0°$	Helix	Sync + 0°	BL
$\varphi_{\text{off}} = 90°$	Helix	Sync + 90°	BL
$\varphi_{\text{off}} = 180°$	Helix	Sync + 180°	BL
$\varphi_{\text{off}} = 270°$	Helix	Sync + 270°	BL
$\varphi_{\text{off}} = 120°$	Helix	Sync + 120°	BL
$\varphi_{\text{off}} = 150°$	Helix	Sync + 150°	BL
$\varphi_{\text{off}} = 210°$	Helix	Sync + 210°	BL
$\varphi_{\text{off}} = 330°$	Helix	Sync + 330°	BL

- **Phase Coherence:** Measures the correlation between estimated and true phase shifts at the Helix frequency, providing insight into estimator reliability.
- **Phase Error:** Quantifies the average deviation in degrees between estimated and ground truth phase shifts to assess tracking precision.

Turbine Performance Metrics

- **Power Production:** Power output from T2 and T3 to assess the influence of phase synchronization on energy production.
- **Structural Loads:** Damage Equivalent Loads (DELs) on T2 and T3, calculated using rainflow counting, to evaluate effects on fatigue life. For this, we use NREL's Mlife toolbox (Hayman 2012).

Flow Analyses

- **Wake Centerlines:** Extracted using Gaussian convolution on phase-averaged velocity fields to analyze wake deflection and mixing patterns.
- **Velocity Deficits:** Quantified as the reduction in velocity relative to free-stream conditions, providing insights into wake recovery and energy availability.

These metrics collectively offer a comprehensive assessment of the trade-offs and effectiveness of the synchronization control strategies.

5.4. RESULTS

This section presents the results of this study. First, the results of the proposed estimator after validation against the ground truth are presented. Then, we investigate the closed-loop results and the effect on power production and loads for the synchronized

test cases. Lastly, flow analysis is performed, investigating wake centerlines and velocity deficits on phase-averaged data.

5.4.1. ESTIMATOR VALIDATION USING GROUND TRUTH

This section provides a preliminary validation of the estimator, by verifying that it is able to capture the parameters of the incoming Helix wake parameters when T2 is operating with baseline control, i.e. where the closed-loop control on T2 is not applied yet. To do so, we present in Fig. 5.10 the wind speeds and Helix phases computed by the estimator of the second turbine in the BL Helix case. We compare these estimates with the ground truth as defined in Section 5.3.3.

Regarding the collective wind speed estimates U_{col}, two comments arise. The estimator is able to capture the variations of mean wind speed but does it with a bias. This discrepancy is mostly attributed to differences between the ALM used in the simulations and the BEM used in the estimator (Coquelet, Lejeune, *et al.* 2024). The ALM tends to compute higher loads than the BEM for similar conditions, especially at relatively coarse grid resolutions as those employed here.

When it comes to the tilt and yaw wind speed components, a transient can be observed for the signals to converge to the ground truth (the estimation process starts at $t = 600$ s). From 1000 s, the estimation aligns with the ground truth, even if the amplitudes of the estimated tilt and yaw components tend to be smaller than those of the ground truth. This can be a consequence of the band-pass filtering process applied during the analysis, or of the use of the same amplitude factor A_{helix} for tilt and yaw wind speed, limiting flexibility in capturing asymmetries in wake dynamics. Allowing independent scaling factors could improve phase and amplitude accuracy, although, in our case, better results were obtained with a single amplitude factor.

Eventually, the main variables of interest in this case are the estimated phase shifts φ_{tilt} and φ_{yaw}. Indeed, these are the values that will be used in the controlled cases. The ground truth values of these signals are obtained from the tilt and yaw wind speed signals using Hilbert transforms. After the estimation transient, the estimates show a consistent trend over time and with the ground truth (quantification is provided in the next section).

These first observations of the estimator's outputs when T2 is operating with baseline control are promising. However, the question remains: can the estimator maintain this performance when T2 is dynamically pitching? To address this, we integrate the estimator into a closed-loop control framework and quantitatively evaluate whether it consistently captures the phase trends under dynamic pitching conditions.

5.4.2. ESTIMATOR PERFORMANCE ANALYSIS

The goal of this analysis is to quantitatively validate the estimator's performance when integrated within a closed-loop control system under dynamically varying conditions using the estimator performance metrics defined in Sec. 5.3.3. This section presents the estimator's performance across synchronization scenarios characterized by distinct phase offsets (φ_{off}). The aim is to confirm that the estimator accurately tracks incoming

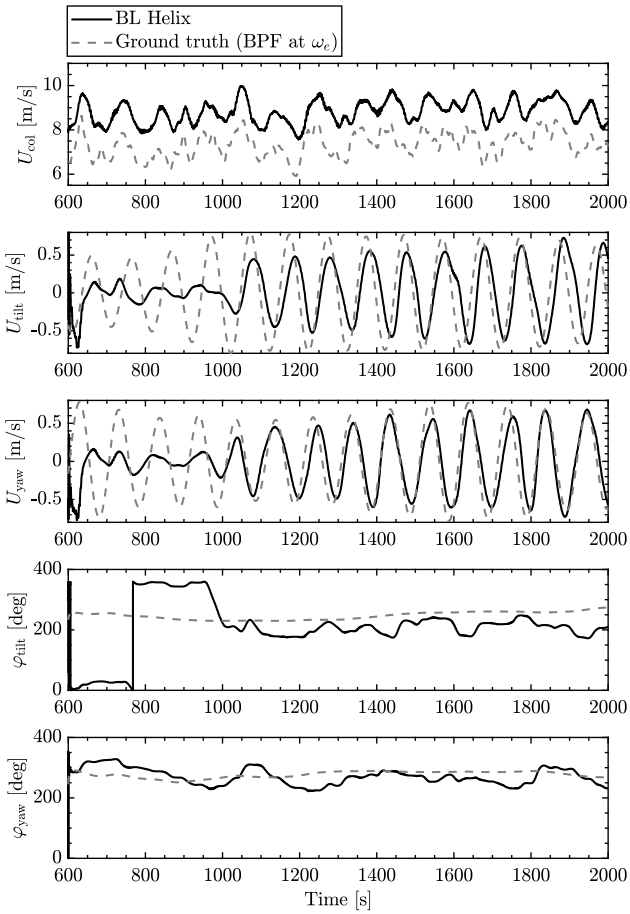

Figure 5.10: Validation of wind speed estimator against ground truth data. Estimation results on T2 for BL Helix case. The ground truth signal is smoother due to spatial averaging and narrow-band filtering before applying the Hilbert transform. The EKF estimate is reconstructed from noisy blade load data at three locations and therefore exhibits greater variability.

wake phase shifts (φ_{tilt} and φ_{yaw}) and remains effective regardless of dynamic control actions.

Figure 5.11 shows the results from the estimator across all four closed-loop synchronized scenarios. A qualitative observation shows that the estimator closely follows the phase trends, regardless of the downstream control actions. However, some deviations are apparent, particularly for the tilt phase estimate, where more time is required to converge to the correct phase shift after activating the synchronization controller at $t = 600$ s, and larger differences between the estimates can be found compared to the yaw phase estimate. Despite these anomalies, the estimator performs well overall, main-

taining close alignment with the expected phase shifts according to the ground truth.

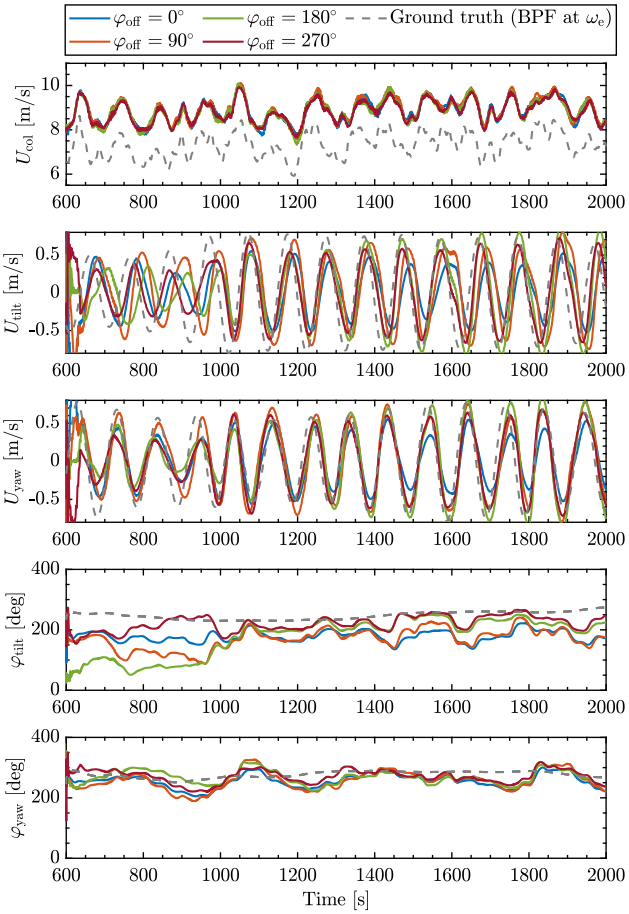

Figure 5.11: Validation of wind speed estimator in closed-loop scenarios. Estimation results on T2 for synchronization cases with different φ_{off}.

To quantify the estimator's reliability, Table 5.3 summarizes the relevant frequency-domain and phase-domain metrics across different phase offsets. Phase error indicates the estimator's ability to align with the timing of the ground truth oscillations. High coherence values (close to 1) suggest a strong correlation between estimated and true signals, reinforcing estimation reliability. The Root Mean Square Error (RMSE) metric evaluates the estimator's capacity to track the phase over time.

The observed RMSE values for tilt phase estimates, between 30° and 82°, indicate a notable bias in the phase estimation. The bias in yaw phase estimates is much more constant, between 28° and 45°, indicating stronger estimator consistency. However, it is important to note that the proposed synchronization control strategy relies predominantly on maintaining a consistent relative phase offset between turbines, rather than

achieving absolute phase accuracy. As the bias remains relatively constant across scenarios for the yaw phase, its impact on control effectiveness is limited. The consistency allows the controller to reliably synchronize downstream actions relative to the incoming wake phase, ensuring effective wake mixing. For the tilt phase, less consistency implies that the synchronization effect may be less predictable between the different cases, although this is not directly apparent from the results. This is further supported by the observed correlation between applied phase offsets and power production changes (discussed later on), suggesting that the estimator, despite its bias, still captures the essential phase dynamics required for successful synchronization.

An interesting comparison can be made between coherence and phase error across the different offset cases. In the 180° case, coherence values are among the highest of all channels, while the corresponding phase errors, especially for the tilt and yaw components, are also relatively large. This suggests that the estimator accurately captures the dominant frequency content but demonstrates a systematic phase offset. Such biases may arise from discrepancies between the internal dynBEM model and the true wake dynamics observed in the LES input or limitations of the ground truth computation methodology. In contrast, the 270° case combines high coherence with low phase error and RMSE values, indicating both accurate and stable tracking. The 0° and 90° cases, by comparison, exhibit lower coherence and higher RMSE, suggesting reduced estimator robustness and increased sensitivity to model mismatch in those configurations.

Further sensitivity studies may be required to analyze the effects of the biases on the controller performance. Nonetheless, future improvements could focus on systematic bias correction. For instance, calibrating the estimator using controlled field experiments or enhancing the dynBEM model to better match observed wake dynamics could reduce this bias. Alternatively, adaptive filtering techniques that account for model-structure uncertainties may further improve phase accuracy.

Table 5.3: Frequency-domain and EKF phase metrics for different orientations at f_0.

Metric	**0°**	**90°**	**180°**	**270°**
Frequency-Domain Metrics				
U_{col} Phase Error [deg]	2.95	3.35	7.75	4.98
U_{col} Coherence	0.87	0.82	0.83	0.89
U_{tilt} Phase Error [deg]	-16.85	-6.58	16.83	5.03
U_{tilt} Coherence	0.65	0.77	0.94	0.96
U_{yaw} Phase Error [deg]	0.07	12.36	13.50	8.00
U_{yaw} Coherence	0.88	0.88	0.94	0.91
Phase Metrics (EKF Estimates)				
φ_{tilt} RMSE [deg]	82.37	68.99	39.33	30.72
φ_{yaw} RMSE [deg]	44.78	46.11	34.33	27.75

Overall, these results confirm that the estimator performs robustly across the phase offsets, with coherence levels above 0.8 for most components indicating strong reliabil-

ity. However, discrepancies in tilt component estimates, particularly in RMSE, suggest potential improvement areas. These deviations may originate from model inaccuracies within the estimator but could also be due to uncertainties in the ground truth calculations.

5.4.3. CLOSED-LOOP SYNCHRONIZATION ANALYSIS

To understand the effect of synchronization on the turbine operation, we examine the correlations between the estimated incoming wake, the pitch action that is performed, and the impact of the loads. Figure 5.12 presents these signals for the tilt axis. It first shows the control signals generated for the downstream turbine based on the estimated phase and the applied additional phase shift, following Eq. 5.22. The control signals are evenly spaced in accordance with the intended phase shifts, indicating that the control system effectively implements the intended phase adjustments. This regular spacing also confirms that the estimator's phase outputs are being correctly interpreted by the control system and that the phase shifts are accurately applied to the downstream control actions. Figure 5.12 then shows the impact of the pitch action on the moments. Note that the moments have been low-pass filtered with a passband frequency 0.01 Hz for clarity. In the BL Helix case, T2 does not perform the Helix control and its pitch angles remain constant during operation. The moments are therefore the direct reflection of the local changes in wind speed. When the incoming U_{tilt} shows a local maximum (as at $t = 1275$ s for example), the tilt moment M_{tilt} also reaches a local maximum. When synchronization is applied, the effect of the pitch interacts with that of the local changes in wind speed. We here highlight two characteristic interactions:

- $\varphi_{\text{off}} = 180°$: The pitch acts in opposition of phase with the incoming wind, as described in Section 5.2.6. When the wind speed perturbation U_{tilt} reaches a maximum, the pitch angle β_{tilt} reaches a minimum. From the aerodynamic perspective, this means that the angles of attack increase, and so do the moments. This is confirmed when looking at the signal of the tilt moment M_{tilt}, whose peak appears at the same location as in the Helix BL case (black curve), but with a higher amplitude. This amplification reflects a constructive interference between the control action and the oscillations in incoming wind speeds induced by the Helix wake.

- $\varphi_{\text{off}} = 0°$: The pitch acts in phase with the incoming wind. When the wind speed perturbation U_{tilt} reaches a maximum, the pitch angle β_{tilt} also reaches a maximum. This implies a decrease in local angles of attack, and hence of moments. There is, therefore, a competing effect: the blade passes through a high wind speed region but reduces its angle of attack. In this case, the pitch angle is rather important (4°) and the control effect takes over the incoming wind effect. Looking at the time series of the moment, one can observe that the tilt moment signal is in this case in opposition of phase with that of the BL Helix case (black curve). There is therefore a destructive interference between the control action and the incoming Helix wake.

Figure 5.13 examines the frequency content of the tilt moments displayed in Fig. 5.12, focusing on the frequency band around the helix frequency peak. The 180° phase shift

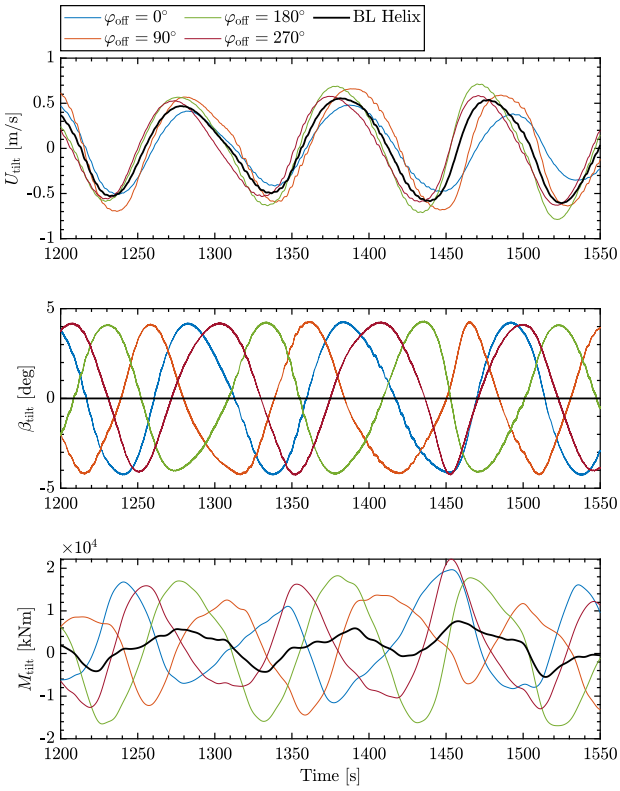

Figure 5.12: Tilt wind speed estimate U_{tilt}, synchronized pitch β_{tilt} and resulting moment M_{tilt} of the downstream turbine under various phase-shifted control strategies.

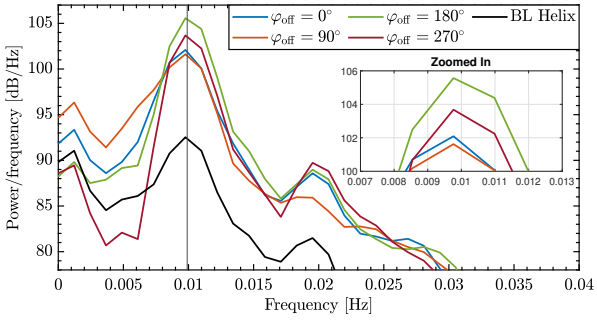

Figure 5.13: Frequency content analysis of tilt moments around the Helix frequency. The 180° case exhibits higher magnitudes at the Helix frequency, indicating enhanced resonance.

case shows the largest magnitude at the helix frequency. This result indicates a stronger resonant effect when the control signals are phase-shifted by 180°, which could be linked to the synchronization of the downstream turbine's response with the periodic wake structure. Such resonance may lead to both beneficial and adverse effects, enhancing power production but potentially increasing fatigue loads. The next section will further investigate the performance differences between the different synchronization cases from a power and load perspective.

5.4.4. CLOSED-LOOP PERFORMANCE ANALYSIS

The effect of these phase-shifted control strategies on overall power production is shown in Fig. 5.14. Note that the power differences shown are with respect to the BL Helix case (see Table 5.2). Hence, the reported power increases are on top of the power increases *already* generated by implementing the Helix on the upstream turbine. In addition to the relative power increases plotted by black crosses, a Gaussian Process (GP) regression fit is plotted that captures the trend between these data points and provides confidence intervals (see e.g. Rasmussen 2004). This approach not only interpolates between the measured phase shifts but also quantifies the predictive uncertainty, illustrating the potential power gains at unmeasured offsets[1]. It appears that, from this figure, the optimal offset is at 150°, which yields a power gain of around 10% on the third turbine (middle plot). Collectively, this amounts to a power increase of around 5% (right plot), since a small loss of 1-2% (left plot) on T2 can be observed. This illustrates a core principle of wake mixing control: the upstream turbine (here, T2) may incur a small power loss to improve the inflow to a downstream turbine (T3), resulting in a net farm-level gain. Such upstream sacrifices are typical of coordinated wind farm flow control (Meyers, C. Bottasso, *et al.* 2022). Interestingly, the best-performing case also sees the lowest power loss on T2, while the worst-performing cases (270° and 330°) exhibit significant power losses for both T2 and T3—over 6% overall—suggesting that implementing a Helix without synchronization on T2 could lead to considerable power losses. Overall, the results highlight that the synchronized Helix wake mixing approach exhibits both optimal and suboptimal regions of power production governed by the phase shift relative to the incoming Helix wake.

It is worth noting that extending synchronization to T3 would change its role from passive beneficiary to active contributor. By doing so, T3 would likely experience a small power loss, as it would then act to enhance the inflow to a hypothetical fourth turbine. Hence, further actuation downstream is only beneficial if additional turbines can exploit the modified wake.

Figure 5.15 provides an overview of the load impacts across different turbine components due to the various phase-shifted control strategies. The results reveal that the loads on the second turbine generally increase for all phase shifts, except a notable tower base load reduction in both fore-aft and side-side is observed for the best-performing 150° case. For the third turbine, increased loads are primarily observed in cases with power gains. This is driven by enhanced wake mixing, which amplifies wake meandering at T2,

[1] GP configuration: zero-mean prior; squared-exponential covariance (GPML's `covSEiso` (Rasmussen and Nickisch 2010)); hyperparameters (length-scale and signal and noise variances) optimized via marginal likelihood maximization (gradient descent); shaded band denotes the 95 % predictive confidence interval.

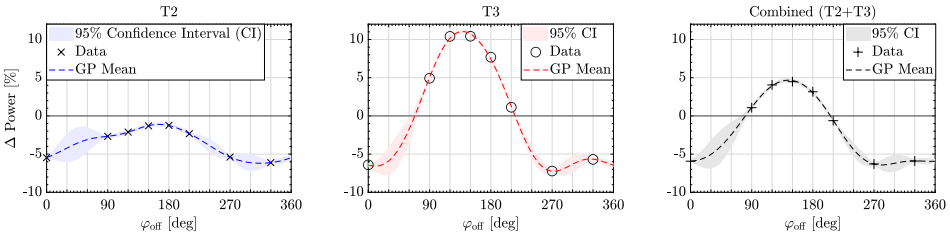

Figure 5.14: Effect of phase offsets in the synchronization controller on power production of downstream turbines. The data points show the relative power change, while the Gaussian process confidence interval shows uncertainty at untested phase offsets. Note that the power differences shown are with respect to the BL Helix case (see Table 5.2). Hence, the power increases are on top of the power increases *already* generated by implementing the Helix on the upstream turbine.

causing greater wind speed fluctuations at T3, this is further highlighted in Section 5.4.5. Such variations increase cyclic loading and fatigue, leading to higher DELs. These results stress the trade-off between power production and structural loading, where certain phase shifts that improve power output might simultaneously increase the fatigue build-up on the turbines, potentially affecting their lifespan.

This analysis exposes the complex interactions between phase-shifted control actions, wake dynamics, and turbine performance. While some phase alignments, like the 120° and 150° shift, offer significant improvements in power output, they also come with potential drawbacks in terms of increased loads.

5.4.5. FLOW ANALYSIS

This final analysis aims to understand the impact of the synchronized controller on T2's wake, further highlighting its effect on T3's performances.

Horizontal velocity slices were extracted at hub height. These velocity fields were phase-averaged over 21 full Helix cycles (approximately 100 seconds per cycle), with each cycle divided into 36 equidistant phases. This approach reveals the periodic characteristics of the Helix wake while averaging out transient fluctuations.

The wake centerline was estimated from these phase-averaged velocity deficit fields using a Gaussian convolution method (Coudou *et al.* 2018). The convolution was applied to the streamwise velocity component u_x, to enhance the identification of coherent wake structures. The Gaussian kernel effectively amplifies regions of high-velocity gradients along the lateral direction, allowing for a robust identification of wake boundaries. The wake trajectory was then determined by locating the lateral position of the maximum convolution response at each streamwise location.

Figure 5.16a illustrates the phase-averaged horizontal velocity deficit fields for the 150° phase shift case, which yielded the highest collective power gain. Figure 5.16b shows the phase-averaged horizontal velocity deficit fields for the 330° phase shift case, which, together with the 270° case, was the worst-performing in terms of power gain. Here, we

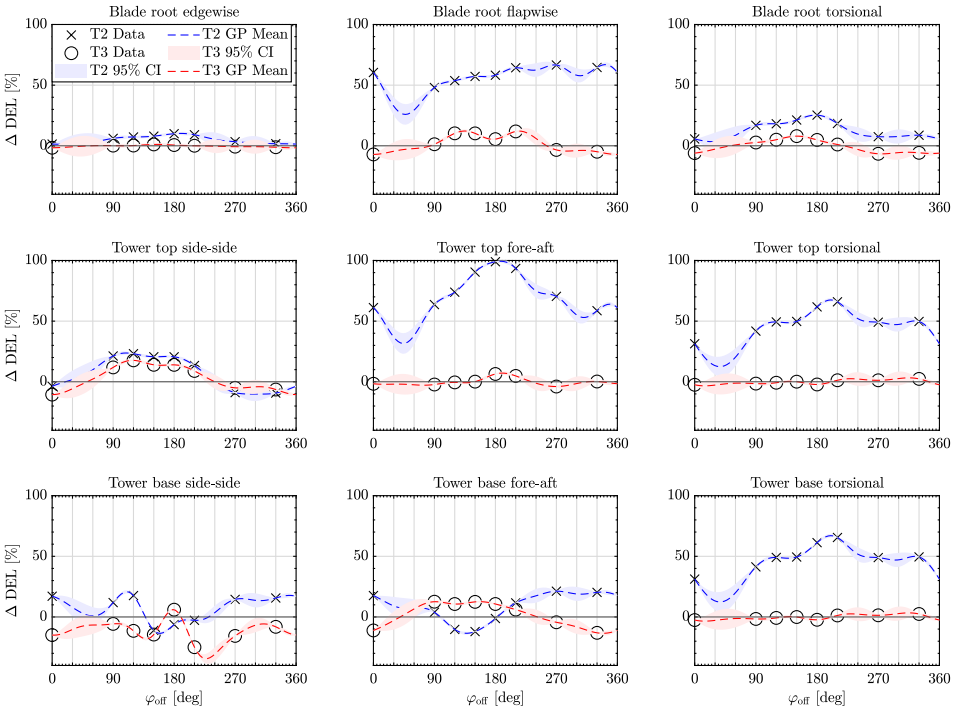

Figure 5.15: Effect of phase offsets in the synchronization controller on damage-equivalent loads for both T2 and T3. The data points show the relative DEL change, while the Gaussian process confidence interval shows the uncertainty of the DEL change at untested phase offsets. CI denotes confidence interval.

choose to compare 150° and 330° since they are 180° apart. Figure 5.16c overlays the wake centerlines from Figs. 5.16a– 5.16b with the wake centerlines from the cases T1 only (Helix) and BL Helix. This highlights that the wake displacement is higher behind T2 for the 150° scenario, with the wake exhibiting a more sustained structure thanks to constructive interference created at the rotor. The amplitude of the 330° case appears more flattened after T2, we identify this as the result of the destructive interference with the incoming wake. Sustaining rather than going against the Helix oscillation on T2 therefore leads to enhanced displacement of T2, which contributes to the higher power produced by T3 in the 150° case.

Lastly, in Fig. 5.17, we examine the velocity deficits across the wake's width at several instances behind T2. To obtain these results, the wake centers have been recentered to zero using the wake centerline. This enables us to separate the effects of wake displacement and wake deficit reduction when it comes to the increased power on T3. This figure shows that the in-phase control ($\varphi_{\text{off}} = 150°$) not only enhances the lateral/vertical displacement of the downstream wake but also reduces the intensity of the wake deficit.

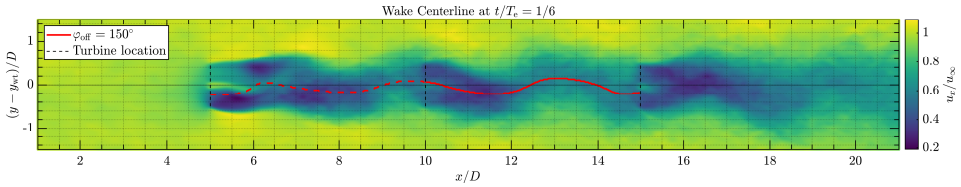

(a) 150° phase shift case. The wake centerline (red line) exhibits sustained periodicity and constructive interference, improving wake mixing and downstream power production.

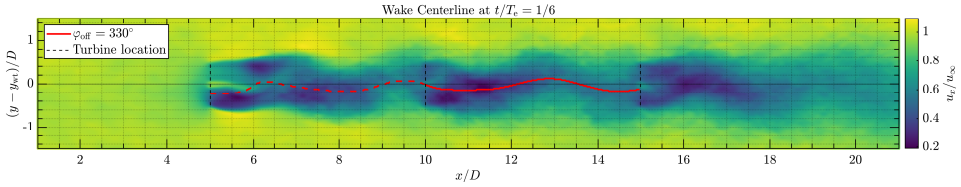

(b) 330° phase shift case. The wake trajectory (red line) displays flattened oscillations and destructive interference, reducing wake mixing and downstream performance.

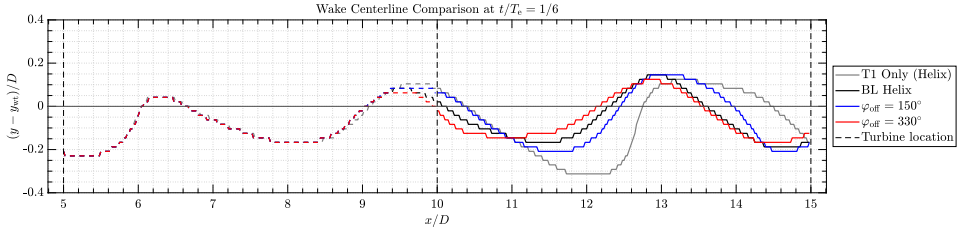

(c) Wake trajectory comparison between the best-performing (150°) and worst-performing (330°) cases, alongside the baseline Helix wake trajectory.

Figure 5.16: Comparison of phase-averaged horizontal velocity fields at hub height for different phase shift cases. T_e is the Helix period and t indicates the time instance at which the snapshot is taken. The best-performing case (150°) aligns closely with the natural Helix oscillation with T1 only, while the worst-performing case (330°) diverges. Note that the y-axis has been scaled in the third subfigure to better visualize the differences.

This 150° case enhances the combined effects of the helix: it promotes wake deficit recovery through mixing, but also enhances lateral wake displacement, which could be assimilated to forced/enhanced meandering. These combined effects explain the higher power leveraged at T3.

5.5. DISCUSSION

This study presents a significant advancement in phase synchronization strategies for wind farm optimization, addressing research gaps identified in prior research by Korb,

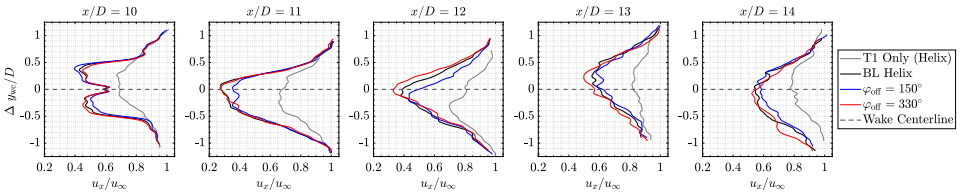

Figure 5.17: Velocity deficits across several flow slices downstream of T2 for the best (150°) and worst (330°) phase-shift cases. The best-performing case shows reduced deficits near the wake centerline, suggesting improved wake recovery.

Asmuth, and Ivanell 2023 and van Vondelen, Pamososuryo, *et al.* 2025.

- **Dynamic Phase Synchronization:**
  - Korb, Asmuth, and Ivanell 2023 demonstrated that specific phase alignments between turbines could improve power recovery. However, their approach, which relied on geometric phase shifts, is sensitive to wind speed and turbine spacing, limiting practical applicability.
  - Our EKF-based synchronization method addresses this gap by dynamically estimating the upstream wake phase and adjusting downstream turbine controls accordingly. The approach is robust to changing wind conditions and turbine configurations.
  - The results indicate that a 150° phase shift between the incoming wake and the turbine action achieved a substantial 10% increase in power output at the third turbine (T3), with an additional overall power gain of 5% over the baseline achieved by implementing the Helix.
- **Balancing Power Gains and Structural Loads:**
  - While power gains were accompanied by increased structural loads, particularly on T2, this trade-off provides valuable insights for optimizing load-mitigation control strategies in future applications.
  - Understanding the relationship between phase alignment, power gains, and structural loads enables more informed control decisions, ensuring long-term turbine integrity while maximizing energy production.
- **Enhanced Performance Over Previous Studies:**
  - Compared to the +6% power gain reported by van Vondelen, Pamososuryo, *et al.* 2025 using in-phase synchronization, our method (+10% on T3) demonstrates superior performance by leveraging optimized out-of-phase alignments.
  - Although this approach introduces additional complexity in phase estimation and control, it offers greater potential for enhancing wind farm efficiency.

- **Insights from Flow Dynamics:**
  - Flow analysis reveals that constructive interference (e.g., 150° phase offset) sustains the natural Helix wake oscillation, enhancing wake recovery and improving downstream power generation.
  - Conversely, destructive interference (e.g., 330° offset) disrupts wake recovery, reducing downstream energy yield. This highlights the importance of aligning control strategies with the natural dynamics of the wake.

The main challenge for practical implementation lies in accurately parameterizing wake dynamics and ensuring robust phase detection under high turbulence and gust conditions. While the proposed EKF-based method demonstrates reliable performance in controlled scenarios, increased turbulence could make identifying consistent phase trends more difficult, complicating synchronization. Enhancing model fidelity and integrating adaptive estimation techniques may be necessary to ensure robustness in variable conditions. Wind tunnel and field testing will be critical to confirm real-world applicability.

Overall, the proposed EKF-based synchronization method demonstrates promise for real-world applications, offering a robust and adaptable approach to enhance wind farm performance. Future research could focus on further refining load-mitigation control strategies and expanding the methodology to larger wind farm configurations.

5.6. CONCLUSION

This study proposed and evaluated an Extended Kalman Filter-based phase synchronization method to enhance downstream turbine performance in wind farms through coordinated wake control. By addressing the limitations of linear Kalman filters and incorporating a dynamic Blade Element Momentum model, the approach demonstrated improved accuracy in estimating wake phases and collective wind speeds, which are necessary for synchronized control strategies.

The results of this study performed in the CNBL with $U_{\text{hub}} = 10.5$ m/s and $TI_{\text{hub}} = 5\%$ showed that the optimal phase shift yields a significant net power gain of approximately 10% at turbine 3 and 5% collectively across turbine 2 and turbine 3 while sustaining the natural Helix oscillation to enhance wake recovery. The findings also reveal a trade-off between power gains and increased structural loads, particularly on turbine 2. This suggests the need for a careful balance between energy production and turbine fatigue build-up in wind farm control.

Future efforts could enhance the estimator to address model discrepancies and robustness, explore adaptive approaches to mitigate structural loads while maintaining high power yields and expand on testing scenarios including different wind farm layouts.

6

CONCLUSION

The final chapter of this dissertation revisits the overarching dissertation goal and research objectives as stated in the introduction chapter. It then reflects on the limitations encountered, mentioning areas for improvement or extension. These insights form the basis for a set of recommendations for future research directions. Finally, the chapter concludes with a reflective statement on the broader implications of these findings.

Contents

6.1. DISSERTATION GOAL AND RESEARCH OBJECTIVES

The primary aim of this dissertation was to explore and extend dynamic wake mixing strategies beyond the scope of isolated turbine control, with the goal of enabling effective synchronized control within larger wind farm arrays to optimize performance. As wind farms grow in size and complexity, and the number of prime offshore sites is decreasing, the need for smart coordination between turbines becomes increasingly apparent. Inspired by natural synchronization phenomena, such as the flapping of birds in formation, this dissertation introduced frameworks that enable turbines to dynamically align their control actions to exploit upstream wake structures.

The overarching dissertation goal, as outlined in Chapter 1, was therefore formulated as follows:

> **Dissertation goal:** *To extend dynamic wake mixing strategies such as the Helix approach beyond isolated turbine applications, and to develop methods that enable their effective use in deeper wind farm arrays through synchronized control.*

This goal was pursued through six interrelated research objectives (ROs), each advancing synchronized wake mixing control towards technology readiness, quantified through technology readiness levels (TRLs). Later, in the reflection section, a statement on this level is made based on the accomplished objectives. The order of the objectives presents a structured progression: starting with physical feasibility, moving through controller synthesis and estimator design, and finally validating these frameworks in realistic numerical and physical environments, including flow analyses.

RO1: LOAD IMPLICATIONS OF HELIX CONTROL

The first research objective (RO1) addressed a foundational concern: whether dynamic wake mixing using the Helix approach is structurally feasible for wind turbines, and to what extent. Before investigating any advanced coordinated control strategy, it was important to assess the structural implications of continuous dynamic pitching on the turbine components.

Chapter 2 investigated the structural implications of the Helix approach by quantifying pitch bearing damage and damage equivalent loading under different actuation settings, realizing the first research objective and the first two TRLs (1-2):

> **RO1:** *Quantify the structural impact of the Helix approach on the actuating (upstream) turbine. Particular attention must be given to pitch bearing damage, which is critical for assessing the long-term feasibility of dynamic pitching strategies in wind turbines* (see Chapter 2).

The results showed that while the Helix approach can be implemented without excessive load violations, the amplitude of the control signal significantly affects the resulting fatigue damage, especially on the pitch bearing. Additionally, directional differences were observed: counterclockwise Helix actuation resulted in more pitch bearing damage, whereas clockwise actuation caused slightly higher blade root moments. These

insights provide important input for further controller development and fatigue constraints in pitch bearing design.

RO2: OUTPUT-FEEDBACK CONTROL USING LOCAL MEASUREMENTS

Having established that the Helix approach can be implemented within certain structural limits, the second objective (RO2) turned to the development of a controller that could synchronize turbines while addressing two distinct goals: phase alignment for either power optimization and/or load rejection. The central idea was that a downstream turbine could exploit the periodic wake structure induced by upstream Helix actuation, thereby requiring lower pitch amplitudes (when in-phase) to achieve effective wake mixing. At the same time, rejecting the incoming oscillatory loads (i.e., anti-phase) induced by the upstream control signal was hypothesized to reduce fatigue loading and potentially even support improved wake recovery. This objective therefore was the first step toward a coordinated control strategy (TRL 3) that is both enhancing wake recovery and reducing structural loads. Since these two goals, power optimization and load rejection, were eventually found to be conflicting, the control strategy was designed to allow for a deliberate trade-off between them.

In Chapter 3, an output-feedback controller was developed to enable downstream turbines to synchronize with upstream wake structures using only local rotor-level measurements, investigating the second research objective:

> **RO2:** *Develop and evaluate an output-feedback control strategy for synchronized wake mixing that enables downstream turbines to exploit upstream wake structures using only local rotor-level measurements, while allowing for a toggling between power optimization and load rejection.* (see Chapter 3).

The proposed control scheme demonstrated successful closed-loop in-phase synchronization without requiring flow field measurements or explicit (model-based) phase estimation. In addition to improving power output, the controller also enabled the rejection of wake-induced oscillatory loads transmitted from the upstream turbine, depending on the selected control setting. Simulations showed that coordinated *in-phase* Helix actuation enhanced downstream power production, whereas switching to a desynchronized mode suppressed structural loads at the cost of reduced power production. These results confirm that synchronization can be achieved in a decentralized fashion using local sensing and actuation, and that load and power objectives can be traded off via a tunable control strategy.

RO3: REAL-TIME PHASE ESTIMATION VIA KALMAN FILTERING

While in-phase synchronization using local sensing proved effective, its performance appeared to depend on the relative timing of the actuation (Korb, Asmuth, and Ivanell 2023). Thus, the third objective (RO3) tackled the challenge of estimating this phase offset in real time, enabling also *out-of-phase* synchronization, which offers an additional control handle to manipulate wake-to-wake interaction through phased wake alignment (TRL 3).

Chapters 4 and 5 addressed the development of real-time estimators to reconstruct the phase of wake-induced flow structures from local measurements to allow *out-of-phase* synchronization, tackling the third research objective:

> **RO3:** *Design and implement an estimator-based framework to reconstruct the phase of periodic wake-induced flow structures in real time. The estimator must be designed to enable out-of-phase synchronization across the turbine array* (see Chapters 4 and 5).

A linear Kalman filter was first implemented in a wind tunnel environment (Chapter 4), successfully tracking the incoming phase in real time and enabling out-of-phase synchronization. Subsequently, an extended Kalman filter was developed for broader operating use (Chapter 5), providing improved estimation accuracy under realistic, turbulent, inflow conditions. Out-of-phase synchronization demonstrated regions of enhanced and reduced power production, depending on the phase offset, following a characteristic S-shape pattern. This research objective showed that the relative phase alignment between turbines directly governs the degree of constructive or destructive wake interference and thereby influences downstream performance.

RO4: LES VALIDATION OF SYNCHRONIZED CONTROL

With both control and estimation frameworks in place, the fourth objective (RO4) focused on validating synchronized wake mixing under realistic turbulent conditions using high-fidelity LES. This was a critical step to assess how robust the coordination frameworks are when faced with realistic environmental conditions and advancing the technology towards TRL 4-5.

High-fidelity simulations in Chapter 5 were used to evaluate the effectiveness of synchronized wake mixing under turbulent conditions, taking on the fourth research objective:

> **RO4:** *Validate the effectiveness of synchronized wake mixing control in realistic high-fidelity LES using modern reference wind turbines, assessing both power and load implications across different synchronization settings* (see Chapter 5).

The results confirmed that synchronization yields consistent power gains across a range of phase alignments, with constructive interference between Helix-induced structures leading to enhanced wake recovery, and destructive interference to negative performance effects. Tower base loads on downstream turbines were also reduced in certain scenarios, suggesting a combined benefit of increased power and decreased fatigue. These findings validate the control framework in a realistic simulation environment and support motivation for further experimental developments.

RO5: EXPERIMENTAL DEMONSTRATION IN A SCALED ARRAY

Motivated by the simulation results, the fifth objective (RO5) attempted a physical demonstration (TRL 4-5): implementing synchronized Helix control in a scaled wind

tunnel setup. This advanced the study of synchronized wake mixing from theoretical simulation to experimental proof-of-concept.

The feasibility of synchronized Helix control was experimentally demonstrated in Chapter 4 using a scaled wind tunnel setup, realizing the fifth research objective:

> **RO5:** *Demonstrate the feasibility of synchronized control experimentally in a wind tunnel setup using a scaled turbine array. This includes real-time phase estimation, closed-loop synchronization, and downstream performance evaluation* (see Chapter 4).

The experimental results confirmed that downstream turbines can synchronize their control actions with upstream wake structures in real time using only local measurements. Notably, the power gain of the closed-loop system was relatively consistent across repeated trials. This is the first known experimental demonstration of synchronized dynamic wake control in a multi-turbine setup.

RO6: INTERFERENCE INSIGHT INTO SYNCHRONIZED WAKE BEHAVIOR

Finally, the sixth objective (RO6) zoomed back in to understand the physical flow mechanisms that govern synchronized wake effects. This analysis provided some insights into the aerodynamic origins of the observed performance gains, helping to understand potential directions for future synchronization developments towards higher TRLs.

Chapter 5 also provided interference insight into how synchronized Helix actuation influences wake development and downstream turbine performance, to address the final research objective:

> **RO6:** *Investigate the physical mechanisms responsible for performance changes under synchronized control. Flow analyses must be used to identify how phase alignment, coherent structures, and turbulence interactions contribute to wake recovery and downstream performance gains* (see Chapter 5).

Flow field analysis revealed that phase alignment plays a decisive role in shaping coherent structures within the wake and promoting efficient momentum entrainment. Constructive synchronization enhances wake recovery and improves downstream inflow conditions, while misaligned, destructive alignment may have nonexistent or even negative effects. Based on these findings, it is clear that phase coordination is crucial for optimizing wake mixing in deeper arrays.

Together, these achieved research objectives address the full control pipeline: from understanding structural constraints (RO1), to designing decentralized controllers (RO2), developing robust estimators (RO3), validating control effectiveness in simulation and experiment (RO4, RO5), and interpreting underlying aerodynamic mechanisms (RO6). Combined, they achieve the dissertation's central goal: enabling synchronized wake mixing in realistic wind farm settings through integrated estimation and control.

6.2. LIMITATIONS AND BOUNDARIES

While the research in this dissertation demonstrates the feasibility and benefits of synchronized wake mixing control, several limitations and boundaries of the scope must be acknowledged. These originate from both methodological choices and practical constraints, and they highlight areas where further investigation is needed before full-scale deployment in wind farms can be investigated.

- **Scalability limitations of the experimental setup.** The experimental validation was conducted in a controlled wind tunnel using scaled turbine models. While this environment enabled precise measurements and repeatable conditions, scaling effects may influence wake behavior and structural responses, as was already apparent from the high actuation losses on the upstream turbines due to significantly higher pitching frequencies required by scaled models compared to utility-scale wind turbines (see Chapter 4).

- **Idealized inflow conditions in experiments.** Although wind tunnel experiments provide realistic flow conditions, they were conducted with consistent, controlled inflow. Real-world wind conditions often contain greater variation, such as gusts, shear, and veer. Such variability may affect the robustness of real-time estimation and synchronization, and thus remains an important challenge for further experimental validation. Advanced wind tunnel or field experiments could validate the framework in more complex scenarios (see Chapter 4).

- **Assumptions in estimator design.** The Kalman filter-based estimators rely on linear or weakly nonlinear models derived from system identification or engineering models. While effective in controlled conditions, these models may not generalize to all inflow scenarios or turbine designs. Estimator performance could decline under changing conditions or model mismatch (see Chapter 4 and 5).

- **Focus on a single wake mixing method.** The dissertation focuses exclusively on dynamic wake mixing via Helix actuation. Other wind farm control strategies, such as dynamic induction control, wake steering, or axial induction control, were not considered individually or in combination with Helix. The broader integration of multiple control methods within a unified, synchronized framework remains an open challenge and presents a promising direction for supervisory or hybrid wind farm control strategies.

- **No variation in wind field realizations in simulations.** The simulation studies validate only a selection of controller settings using a single precursor due to the high computational cost of LES. While the evaluated simulation environment is realistic, exploring different turbulent intensities and realizations is important to demonstrate the robustness of the synchronization controller in varying flow environments, required for understanding the complete performance effects (see Chapter 3 and 5).

These limitations, however, do not reduce the validity of the presented results but do provide a realistic context for interpretation. They also indicate important directions for

follow-up research and field validation needed to transition synchronized wake mixing from experimental concept to an established technology.

6.3. RECOMMENDATIONS FOR FUTURE WORK

The findings and limitations discussed in this dissertation motivate several directions for future research. To further develop synchronized wake mixing into an established wind farm control strategy, efforts are needed across conceptual, computational, and experimental domains. The following recommendations are made:

- **Field testing in utility-scale wind farms.** An important next step is the implementation of synchronized control in operational wind farms. Field campaigns could validate estimator robustness, controller performance, and structural impacts under real atmospheric conditions. A two-turbine offshore demonstration of the Helix approach is already scheduled (GROW – Dynamic Wind Farm Flow Control 2025). Synchronization field experiments represent a logical next step toward farm-scale implementation of wake mixing control strategies.

- **In-depth flow field analysis of synchronization.** While the current work offers preliminary insights into wake interference mechanisms, these remain largely qualitative. A more detailed flow analysis, focusing on coherent structures such as vortex shedding, wake merging, and turbulent entrainment, could reveal the aerodynamic mechanisms that drive enhanced wake recovery. Gutknecht *et al.* 2025 presents a comprehensive investigation of a single Helix-induced wake; extending such analyses to the interaction between two synchronized Helix wakes would provide a deeper understanding of the flow physics involved. This could inform the design of more effective control strategies that deliberately exploit wake–to-wake interactions to improve overall wind farm performance.

- **Integration with yaw and induction control.** Synchronized Helix actuation could be combined with wake steering or (dynamic) derating strategies in a hybrid control framework. Such coordination likely depends on inflow directionality, turbine spacing, or operational objectives, allowing the farm to dynamically switch between different control modes. The SUDOCO research project is working on this topic, and synchronization could provide an interesting additional control mode (WindpowerNL 2023).

- **Array-to-array effects of synchronization.** Future work should investigate how synchronized turbine arrays interact with each other. Coordinating the phase dynamics of adjacent arrays may enable beneficial flow alignment or even phased interference effects that enhance downstream transport and power extraction. Heydari, Hang, and Kanso 2022 showed that side-by-side configurations for swimmers have specific spatial phase relationships minimizing energy expenditure. Such a relationship may also exist for wind farms through layout optimization combined with synchronized flow patterns.

- **Advanced estimation and control strategies.** Future work may integrate nonlinear estimators such as unscented Kalman filters, particle filters, or learning-based

methods with advanced control to improve robustness and enable horizon-aware actuation. Reinforcement learning, for example, could enable the control system to adapt online to site-specific dynamics and turbulence.

These directions stress the interdisciplinary nature of future work in wind farm flow control. Advancing synchronized wake mixing will require continued collaboration between control engineers, fluid dynamicists, structural analysts, system operators, and industry.

6.4. FINAL REFLECTION

This dissertation set out with a vision inspired by nature: to explore whether wind turbines could, like birds in formation, operate not as isolated machines but as coordinated agents, dynamically responding to shared aerodynamic environments. The resulting frameworks for synchronized wake mixing control represent a step toward realizing that vision, demonstrating that turbines can estimate, align, and act in sync with upstream flow structures.

Throughout this work, several building blocks have been established: real-time phase estimation, decentralized feedback control, numerical and experimental validation, and physical insight into wake interactions. These components form a foundation on which more intelligent and cooperative wind farm systems can be built. The methods developed in this work rely only on local sensing, making them practical and implementable in real-world applications.

Regarding technological maturity, this work has advanced synchronized wake mixing from a conceptual idea to TRL 5. The developed frameworks, estimator-based and output-feedback-based synchronization, have been validated in both simulation and a controlled experimental environment. While further development and field testing are required to progress toward operational deployment (TRL 5–6), the concepts presented here go beyond proof of principle and have been demonstrated as a validated technology in a relevant and realistic context.

Yet, the broader value of synchronization in wind energy lies not only in its technical feasibility but also in its conceptual shift from optimizing individual performance to controlling farm-level performance. This research opened new possibilities for energy extraction, load balancing, and spatial efficiency across wind farms by exploiting flow structures and wake interactions.

As the wind energy sector continues to expand, with larger farms and greater demands, strategies that enable turbines to act in rhythm with the wind and with each other will become increasingly more relevant. The work presented in this dissertation provides a first step in that direction, laying the groundwork for a new field of coordinated control strategies that view the wind farm not as a set of competing units but as a dynamic, cooperative, and collective system.

BIBLIOGRAPHY

Abbas, N. J., Zalkind, D., Mudafort, R. M., Hylander, G., Mulders, S., Heff, D., and Bortolotti, P. (2022). *NREL/ROSCO: RAAW v1.2*. Version raaw1.2. DOI: 10.5281/zenodo.6543598.
https://doi.org/10.5281/zenodo.6543598.

Abbas, N. J., Zalkind, D. S., Pao, L., and Wright, A. (2022). "A Reference Open-Source Controller for Fixed and Floating Offshore Wind Turbines". In: *Wind Energy Science* 7.1, pp. 53–73. DOI: 10.5194/wes-7-53-2022.

Adaramola, M. S. and Krogstad, P.-Å. (2011). "Experimental investigation of wake effects on wind turbine performance". In: *Renewable Energy* 36.8, pp. 2078–2086. DOI: 10.1016/j.renene.2011.01.024.

Allaerts, D. and Meyers, J. (2015). "Large eddy simulation of a large wind-turbine array in a conventionally neutral atmospheric boundary layer". In: *Physics of Fluids* 27.6, p. 065108. DOI: 10.1063/1.4922339.

Annoni, J., Fleming, P. A., Scholbrock, A., Roadman, J., Dana, S., Adcock, C., Porté-Agel, F., Raach, S., Haizmann, F., and Schlipf, D. (2018). "Analysis of Control-Oriented Wake Modeling Tools Using Lidar Field Results". In: *Wind Energy Science* 3.2, pp. 819–831. DOI: 10.5194/wes-3-819-2018.

Annoni, J., Gebraad, P. M. O., Scholbrock, A. K., Fleming, P. A., and van Wingerden, J. W. (2016). "Analysis of axial-induction-based wind plant control using an engineering and a high-order wind plant model". In: *Wind Energy* 19.6, pp. 1135–1150. DOI: 10.1002/we.1891.

Ashuri, T., Zaaijer, M., and van Bussel, G. (2014). "Multidisciplinary design optimization of large wind turbines—Technical, economic, and design challenges". In: *Renewable Energy* 65, pp. 468–476. DOI: 10.1016/j.renene.2013.09.030.

Baricchio, M., Gebraad, P. M. O., and van Wingerden, J. W. (2024). "Evaluating the potential of a wake steering co-design for wind farm layout optimization through a tailored genetic algorithm". In: *Wind Energy Science* 9.11, pp. 2113–2132. DOI: 10.5194/wes-9-2113-2024.

Barthelmie, R. J., Hansen, K., Frandsen, S. T., Rathmann, O., Schepers, J. G., Schlez, W., Phillips, J., Rados, K., Zervos, A., Politis, E. S., and Chaviaropoulos, P. K. (2009). "Modelling and measuring flow and wind turbine wakes in large wind farms offshore". In: *Wind Energy* 12.5, pp. 431–444. DOI: 10.1002/we.348.

Bastankhah, M. and Porté-Agel, F. (2016). "Experimental and theoretical study of wind turbine wakes in yawed conditions". In: *Journal of Fluid Mechanics* 806, pp. 506–541. DOI: 10.1017/jfm.2016.595.

Bir, G. (2008). "Multi-Blade Coordinate Transformation and Its Application to Wind Turbine Analysis". In: *46th AIAA Aerospace Sciences Meeting and Exhibit*, p. 1300. DOI: 10.2514/6.2008-1300.

Bossanyi, E. A. (2003). "Individual blade pitch control for load reduction". In: *Wind Energy: An International Journal for Progress and Applications in Wind Power Conversion Technology* 6.2, pp. 119–128. DOI: 10.1002/we.76.

Brazell, M., Ananthan, S., Vijayakumar, G., Cheung, L., Sprague, M., Team, E. E. C. P., and Team, H. F. M. P. (2021). "AMR-Wind: Adaptive mesh-refinement for atmospheric-boundary-layer wind energy simulations". In: *Abstracts of the 74th Annual Meeting of the APS Division of Fluid Dynamics*. Abstract T29.007 (APS DFD 2021). American Physical Society.
https://ui.adsabs.harvard.edu/abs/2021APS..DFDT29007B.

Burton, T., Jenkins, N., Sharpe, D., and Bossanyi, E. (2011). *Wind Energy Handbook*. 2nd. Chichester, UK: John Wiley & Sons, p. 784. ISBN: 978-0470699751.

Cheung, L., Brazell, M. J., Hsieh, A., Ananthan, S., Vijayakumar, G., and deVelder, N. (2021). "Computation and Comparison of the Stable Northeastern US Marine Boundary Layer". In: *AIAA Scitech 2021 Forum*, p. 0454. DOI: 10.2514/6.2021-0454.

Chiuso, A. (2007). "The role of vector autoregressive modeling in predictor-based subspace identification". In: *Automatica* 43.6, pp. 1034–1048. DOI: 10.1016/j.automatica.2006.12.009.

Chui, C. K. and Chen, G. (2017). *Kalman Filtering: With Real-Time Applications*. 5th. Cham, Switzerland: Springer, p. 247. ISBN: 978-3-319-47610-0. DOI: 10.1007/978-3-319-47612-4.

Coquelet, M., Gutknecht, J., van Wingerden, J. W., Duponcheel, M., and Chatelain, P. (2024). "Dynamic individual pitch control for wake mitigation: Why does the helix handedness in the wake matter?" In: vol. 2767. 9. IOP Publishing, p. 092084. DOI: 10.1088/1742-6596/2767/9/092084.

Coquelet, M., Lejeune, M., Bricteux, L., van Vondelen, A. A. W., van Wingerden, J. W., and Chatelain, P. (2024). "On the robustness of a blade-load-based wind speed estimator to dynamic pitch control strategies". In: *Wind Energy Science* 9.10, pp. 1923–1940. DOI: 10.5194/wes-9-1923-2024.

Coudou, N., Moens, M., Marichal, Y., Van Beeck, J., Bricteux, L., and Chatelain, P. (2018). "Development of wake meandering detection algorithms and their application to large eddy simulations of an isolated wind turbine and a wind farm". In: vol. 1037. 7. IOP Publishing, p. 072024. DOI: 10.1088/1742-6596/1037/7/072024.

Crosswind Hollandse Kust Noord (n.d.). https://www.crosswindhkn.nl/windfarm. Accessed: 2024-07-15.

Dahlberg, J.-Å. (2009). *Assessment of the Lillgrund Wind Farm: Power Performance and Wake Effects*. Technical Report ET 2009:44. Lillgrund Pilot Project. Eskilstuna, Sweden: Swedish Energy Agency.
https://energimyndigheten.a-w2m.se/Home.mvc?ResourceId=7891.

De Kraker, A. (2020). *Windmills in the Netherlands: A Historical Survey*. Amsterdam University Press.

Delft High Performance Computing Centre (2022). *DelftBlue Supercomputer (Phase 1)*. Accessed: 2024-04-23.
https://www.tudelft.nl/dhpc/ark:/44463/DelftBluePhase1.

Doekemeijer, B. M., Kern, S., Maturu, S., Kanev, S., Salbert, B., Schreiber, J., Campagnolo, F., Bottasso, C. L., Schuler, S., Wilts, F., Neumann, T., Potenza, G., Calabretta, F., Fioretti,

F., and van Wingerden, J.-W. (2021). “Field experiment for open-loop yaw-based wake steering at a commercial onshore wind farm in Italy”. In: *Wind Energy Science* 6.1, pp. 159–176. DOI: 10.5194/wes-6-159-2021.

Doekemeijer, B. M., Hoek, D. C. v. d., and Wingerden, J. W. v. (2019). “Model-based closed-loop wind farm control for power maximization using Bayesian optimization: a large eddy simulation study”. In: *2019 IEEE Conference on Control Technology and Applications (CCTA)*, pp. 284–289. DOI: 10.1109/CCTA.2019.8920587.

Durakovic, A. (2022). *First-Ever Subsidy-Free Offshore Wind Farm Halfway Done*. Accessed: 2025-05-13.
https://www.offshorewind.biz/2022/11/01/first-ever-subsidy-free-offshore-wind-farm-halfway-done/.

European Commission (2023). *EU Strategy for Offshore Renewable Energy*. Accessed: 2025-05-15.
https://www.europarl.europa.eu/legislative-train/theme-a-european-green-deal/file-offshore-wind.

Firestone, J., Kempton, W., and Krueger, A. (2012). “Public acceptance of offshore wind power: Does perceived fairness of process matter?” In: *Journal of Environmental Planning and Management* 55.10, pp. 1387–1402. DOI: 10.1080/09640568.2012.688658.

Fleming, P. A., King, J., Dykes, K., Simley, E., Roadman, J., Scholbrock, A., Murphy, P., Lundquist, J. K., Moriarty, P., Fleming, K., van Dam, J., Bay, C., Mudafort, R., Lopez, H., Skopek, J., Scott, M., Ryan, B., Guernsey, C., and Brake, D. (2019). “Initial results from a field campaign of wake steering applied at a commercial wind farm – Part 1”. In: *Wind Energy Science* 4.2, pp. 273–285. DOI: 10.5194/wes-4-273-2019.

Fleming, P. A., Gebraad, P. M. O., Lee, S., van Wingerden, J. W., Johnson, K., Churchfield, M., Michalakes, J., Spalart, P., and Moriarty, P. (2014). “Evaluating Techniques for Redirecting Turbine Wakes Using SOWFA”. In: *Renewable Energy* 70, pp. 211–218. DOI: 10.1016/j.renene.2014.02.015.

Frederik, J. A., Weber, R., Cacciola, S., Campagnolo, F., Croce, A., Bottasso, C., and van Wingerden, J. W. (2020). “Periodic dynamic induction control of wind farms: proving the potential in simulations and wind tunnel experiments”. In: *Wind Energy Science* 5.1, pp. 245–257. DOI: 10.5194/wes-5-245-2020.

Frederik, J. A., Doekemeijer, B. M., Mulders, S. P., and van Wingerden, J. W. (2020). “The helix approach: Using dynamic individual pitch control to enhance wake mixing in wind farms”. In: *Wind Energy* 23.8, pp. 1739–1751. DOI: https://doi.org/10.1002/we.2513.

Frederik, J. A. and van Wingerden, J. W. (2022). “On the load impact of dynamic wind farm wake mixing strategies”. In: *Renewable Energy* 194, pp. 582–595. DOI: https://doi.org/10.1016/j.renene.2022.05.110.

Friesland.nl (2025). *Houtzaagmolen De Rat*. Accessed: 2025-05-13.
https://www.friesland.nl/nl/locaties/450852228/houtzaagmolen-de-rat.

Gaertner, E., Rinker, J., Sethuraman, L., Zahle, F., Anderson, B., Barter, G. E., Abbas, N. J., Meng, F., Bortolotti, P., Skrzypinski, W., *et al.* (2020). *IEA Wind TCP Task 37: Definition of the IEA 15-Megawatt Offshore Reference Wind Turbine*. Tech. rep. National Renewable Energy Lab. (NREL), Golden, CO (United States). DOI: 10.2172/1603478.

Gebraad, P. M. O., Teeuwisse, F. W., van Wingerden, J. W., Fleming, P. A., Ruben, S. D., Marden, J. R., and Pao, L. Y. (2016). "Wind plant power optimization through yaw control using a parametric model for wake effects—a CFD simulation study". In: *Wind Energy* 19.1, pp. 95–114. DOI: https://doi.org/10.1002/we.1822. eprint: https://onlinelibrary.wiley.com/doi/pdf/10.1002/we.1822.

Gipe, P. (1995). *Wind Energy Comes of Age*. 1st. Wiley Series in Sustainable Design. New York, NY, USA: John Wiley & Sons, p. 560. ISBN: 978-0471109242.

Goit, J. P. and Meyers, J. (2015). "Optimal control of energy extraction in wind-farm boundary layers". In: *Journal of Fluid Mechanics* 768, pp. 5–50. DOI: 10.1017/jfm.2015.70.

González-Longatt, F., Wall, P., and Terzija, V. (2012). "Wake effect in wind farm performance: Steady-state and dynamic behavior". In: *Renewable Energy* 39.1, pp. 329–338. DOI: 10.1016/j.renene.2011.08.053.

GROW – Dynamic Wind Farm Flow Control (2025). *Research*. https://grow-flowcontrol.nl/research. Accessed: 2025-06-16.

Guezuraga, B., Zauner, R., and Pölz, W. (2012). "Life cycle assessment of two different 2 MW class wind turbines". In: *Renewable Energy* 37.1, pp. 37–44. DOI: 10.1016/j.renene.2011.03.035.

Gutknecht, J., Taschner, E., Coquelet, M., Viré, A., and van Wingerden, J. W. (2025). "The impact of coherent large-scale vortices generated by helix active wake control on the recovery process of wind turbine wakes". In: *Physics of Fluids*. Accepted for publication.

Hau, E. (2013). *Wind Turbines: Fundamentals, Technologies, Application, Economics*. 3rd. Springer. DOI: 10.1007/978-3-642-27151-9.

Hayman, G. J. (2012). *MLife theory manual for version 1.00*. Technical Report NREL/TP-52862. Golden, CO, USA: National Renewable Energy Laboratory. https://www.nrel.gov/docs/fy12osti/52862.pdf.

Heydari, S., Hang, H., and Kanso, E. (2022). "Mapping spatial patterns to energetic benefits in groups of flow-coupled swimmers". In: *Proceedings of the National Academy of Sciences* 119.25. DOI: 10.1073/pnas.2201011119.

Hintjens, P. (2013). *ZeroMQ: Messaging for Many Applications*. 1st. Sebastopol, CA: O'Reilly Media, Inc., p. 493. ISBN: 978-1-449-33406-2.

Howland, M. F., Lele, S. K., and Dabiri, J. O. (2022). "Collective wind farm operation based on a predictive model improves power capture". In: *Nature Energy* 7, pp. 574–582. DOI: 10.1038/s41560-022-00992-2.

Huang, L. J., Mulders, S. P., Taschner, E., and van Wingerden, J. W. (2023). "Enhancing Wake Mixing in Wind Farms by Multi-Sine Signals in the Helix Approach". In: *2023 American Control Conference (ACC)*. San Diego, CA, USA: IEEE, pp. 824–830. DOI: 10.23919/ACC55779.2023.10155870.

International Electrotechnical Commission (2019). *IEC 61400-3:2019 Wind energy generation systems – Part 1: Design requirements for offshore wind turbines*. Standard IEC 61400-3:2019. Geneva, Switzerland: International Electrotechnical Commission.

International Energy Agency (2023). *Offshore Wind*. Accessed: 2025-05-15. https://www.iea.org/energy-system/renewables/wind.

IPCC (2021). *Climate Change 2021: The Physical Science Basis*. Sixth Assessment Report, Working Group I.
https://www.ipcc.ch/report/ar6/wg1/.

Jiménez, Á., Crespo, A., and Migoya, E. (2010). "Application of a LES technique to characterize the wake deflection of a wind turbine in yaw". In: *Wind Energy* 13.6, pp. 559–572. DOI: https://doi.org/10.1002/we.380. eprint: https://onlinelibrary.wiley.com/doi/pdf/10.1002/we.380.

Jonkman, B., Mudafort, R. M., Platt, A., Branlard, E., Sprague, M., Jonkman, J., Ross, H., Hall, M., Vijayakumar, G., Buhl, M., Bortolotti, P., Ananthan, S., and Rood, J. (2023). *OpenFAST/Openfast: OpenFAST v3.4.0*. Zenodo. DOI: 10.5281/zenodo.7527379.

Jonkman, B., Platt, A., Mudafort, R. M., Branlard, E., Sprague, M., Ross, H., jjonkman, HaymanConsulting, Slaughter, D., Hall, M., Vijayakumar, G., Buhl, M., Russell9798, Bortolotti, P., reos-rcrozier, Ananthan, S., RyanDavies19, S., M., Rood, J., rdamiani, nrmendoza, sinolonghai, pschuenemann, ashesh2512, kshaler, Housner, S., psakievich, Wang, L., Bendl, K., and Carmo, L. (2024). *OpenFAST/openfast: v3.5.3*. Version v3.5.3. DOI: 10.5281/zenodo.10962897.

Jonkman, J. M. (2013). "The New Modularization Framework for the FAST Wind Turbine CAE Tool". In: *51st AIAA Aerospace Sciences Meeting including the New Horizons Forum and Aerospace Exposition*. Grapevine (Dallas area), TX, USA. DOI: 10.2514/6.2013-202.

Kerssemakers, D. R. H. (2022). "On the Load Impact of the Helix Approach on Offshore Wind Turbines: Quantifying and Analyzing the Fatigue Load Impact of the Helix Approach on Offshore Wind Turbine Components". MA thesis. Delft, The Netherlands: Delft University of Technology.
https://repository.tudelft.nl/record/8828b5b4-8077-4101-97e6-1b0b87a63fe6.

Knudsen, T., Bak, T., and Soltani, M. (2011). "Prediction models for wind speed at turbine locations in a wind farm". In: *Wind Energy* 14.7, pp. 877–894. DOI: 10.1002/we.491.

Knudsen, T., Bak, T., and Svenstrup, M. (2015). "Survey of wind farm control—Power and fatigue optimization". In: *Wind Energy* 18.8, pp. 1333–1351. DOI: 10.1002/we.1760.

Korb, H., Asmuth, H., and Ivanell, S. (2023). "The characteristics of helically deflected wind turbine wakes". In: *Journal of Fluid Mechanics* 965, A2. DOI: 10.1017/jfm.2023.390.

La Cour, P. (1900). *Experimental studies on windmills and wind power*. Original Danish work; recognized posthumously for foundational contributions to wind turbine research.

Lignarolo, L. E. M., Ragni, D., Scarano, F., Simão Ferreira, C. J., and van Bussel, G. J. W. (2015). "Tip-vortex instability and turbulent mixing in wind-turbine wakes". In: *Journal of Fluid Mechanics* 781, pp. 467–493. DOI: 10.1017/jfm.2015.470.

Mancini, M., Schreiber, J., and Bottasso, C. A. (2023). "Closed-loop wake redirection in wind tunnel experiments". In: *Wind Energy Science* 8.2, pp. 431–450. DOI: 10.5194/wes-8-431-2023.

Manwell, J. F., McGowan, J. G., and Rogers, A. L. (2010). *Wind Energy Explained: Theory, Design and Application*. 2nd ed. Chichester, West Sussex, U.K.: John Wiley & Sons. ISBN: 978-0-470-01500-1. DOI: 10.1002/9781119994367.

Marden, J. R., Ruben, S. D., and Pao, L. Y. (2013). "A Model-Free Approach to Wind Farm Control Using Game Theoretic Methods". In: *IEEE Transactions on Control Systems Technology* 21.4, pp. 1207–1214. DOI: 10.1109/TCST.2013.2257780.

McCroskey, W. J. (1982). *Unsteady Airfoils*. NASA Technical Memorandum NASA-TM-81182. Moffett Field, CA: NASA Ames Research Center.

McKinsey & Company (2024). *Offshore wind: Strategies for uncertain times*. Accessed: 2025-05-13.
https://www.mckinsey.com/industries/electric-power-and-natural-gas/our-insights/offshore-wind-strategies-for-uncertain-times.

Mehra, R. (1970). "On the identification of variances and adaptive Kalman filtering". In: *IEEE Transactions on Automatic Control* 15.2, pp. 175–184. DOI: 10.1109/TAC.1970.1099422.

Meyers, J., Bottasso, C., Dykes, K., Fleming, P. A., Gebraad, P. M. O., Giebel, G., Göçmen, T., and van Wingerden, J. W. (2022). "Wind farm flow control: prospects and challenges". In: *Wind Energy Science* 7.6, pp. 2271–2306. DOI: 10.5194/wes-7-2271-2022.

Meyers, J. and Meneveau, C. (2012). "Optimal turbine spacing in fully developed wind farm boundary layers". In: *Wind Energy* 15.2, pp. 305–317. DOI: 10.1002/we.469.

Ministerie van Algemene Zaken (2021). *Offshore wind energy*.
https://www.government.nl/topics/renewable-energy/offshore-wind-energy.

– (2022). *Kabinet Verdubbelt Productie windenergie op zee*.
https://www.rijksoverheid.nl/actueel/nieuws/2022/03/18/kabinet-verdubbelt-productie-windenergie-op-zee.

Ministerie van Economische Zaken en Klimaat (2023). *Einde gaswinning in Groningen definitief vastgesteld*. Accessed: 2025-05-13.
https://www.rijksoverheid.nl/documenten/publicaties/2023/09/22/einde-gaswinning-groningen.

Moens, M., Coquelet, M., Trigaux, F., and Chatelain, P. (2022). "Handling Individual Pitch Control within an Actuator Disk framework: verification against the Actuator Line method and application to wake interaction problems". In: *Journal of Physics: Conference Series* 2265.2, p. 022053. DOI: 10.1088/1742-6596/2265/2/022053.

Mulders, S. P., Pamososuryo, A. K., Disario, G. E., and van Wingerden, J. W. (2019). "Analysis and Optimal Individual Pitch Control Decoupling by Inclusion of an Azimuth Offset in the Multiblade Coordinate Transformation". In: *Wind Energy* 22.3, pp. 341–359. DOI: 10.1002/we.2289.

Munters, W. and Meyers, J. (2018a). "Dynamic induction control of wind farms and its potential to reduce structural loads". In: *Wind Energy Science* 3.1, pp. 409–425. DOI: 10.5194/wes-3-409-2018.

– (2018b). "Towards practical dynamic induction control of wind farms: analysis of optimally controlled wind-farm boundary layers and sinusoidal induction control of first-row turbines". In: *Wind Energy Science* 3.1, pp. 409–425. DOI: 10.5194/wes-3-409-2018.

Muscari, C., Schito, P., Viré, A., Zasso, A., van der Hoek, D. C., and van Wingerden, J. W. (2022). "Physics informed DMD for periodic Dynamic Induction Control of Wind

Farms". In: *Journal of Physics: Conference Series*. Vol. 2265. 2. IOP Publishing, p. 022057. DOI: 10.1088/1742-6596/2265/2/022057.

NedZero (2024). *The North Seas Standard: enable growth with wind turbine standardization*. Online. Published by NedZero; accessed June 10, 2025. https://www.nedzero.nl/en/news/the-north-seas-standard-enable-growth-with-wind-turbine-standardization.

O'Rourke, C. J., Qasim, M. M., Overlin, M. R., and Kirtley, J. L. (2019). "A Geometric Interpretation of Reference Frames and Transformations: dq0, Clarke, and Park". In: *IEEE Transactions on Energy Conversion* 34.4, pp. 2070–2083. DOI: 10.1109/TEC.2019.2941175.

Oppenheim, A. V., Willsky, A. S., and Nawab, S. H. (1997). *Signals and Systems*. 2nd. Prentice-Hall Signal Processing Series. Upper Saddle River, NJ, USA: Prentice Hall, p. 957. ISBN: 978-0138147570.

Pamososuryo, A. K., Mulders, S. P., Ferrari, R., and van Wingerden, J. W. (2024). "On the Analysis and Synthesis of Wind Turbine Side–Side Tower Load Control via Demodulation". In: *IEEE Transactions on Control Systems Technology* 32.5, pp. 1865–1880. DOI: 10.1109/TCST.2024.3377508.

Portugal, S. J., Hubel, T. Y., Fritz, J., Heese, S., Trobe, D., Voelkl, B., Hailes, S., Wilson, R. P., and Usherwood, J. R. (2014). "Upwash exploitation and downwash avoidance by flap phasing in ibis formation flight". In: *Nature* 505, pp. 399–402. DOI: 10.1038/nature12939.

Rasmussen, C. E. (2004). "Gaussian Processes in Machine Learning". In: *Advanced Lectures on Machine Learning: ML Summer Schools 2003, Canberra, Australia, February 2–14, 2003, Tübingen, Germany, August 4–16, 2003, Revised Lectures*. Ed. by O. Bousquet, U. von Luxburg, and G. Rätsch. Berlin, Heidelberg: Springer Berlin Heidelberg, pp. 63–71. ISBN: 978-3-540-28650-9. DOI: 10.1007/978-3-540-28650-9_4.

Rasmussen, C. E. and Nickisch, H. (2010). "Gaussian Processes for Machine Learning (GPML) Toolbox". In: *Journal of Machine Learning Research* 11, pp. 3011–3015. http://www.jmlr.org/papers/v11/rasmussen10a.html.

Rasmussen, C. E. and Williams, C. K. I. (2006). *Gaussian Processes for Machine Learning*. Cambridge, MA: MIT Press. ISBN: 9780262182539. http://www.gaussianprocess.org/gpml/.

Regulatory Assistance Project (2024). *Gridlock in the Netherlands: Addressing Congestion in a Renewable Future*. Accessed: 2025-05-13. https://www.raponline.org/wp-content/uploads/2024/01/RAP-Pato-Netherlands-gridlock-2024.pdf.

REN21 (2023). *Renewables 2023 Global Status Report*. Accessed: 2025-05-13. https://www.ren21.net/reports/global-status-report/.

Reuters (2025a). *Dutch grid group TenneT plans to invest €216 billion by end of 2034*. Accessed: 2025-05-13. https://www.reuters.com/business/energy/dutch-grid-group-tennet-plans-invest-216-billion-by-end-2034-2025-03-06/.

– (2025b). *Orsted cancels major UK wind project as economics worsen*. Accessed: 2025-05-13.

https://www.reuters.com/sustainability/climate-energy/offshore-wind-developer-orsted-q1-beats-forecasts-2025-05-07/.

Reuters (2025c). *Spain investigates cyber weaknesses at small power plants after blackout*. Accessed: 2025-05-13. https://www.reuters.com/business/energy/spain-investigates-cyber-weaknesses-small-power-plants-after-blackout-ft-reports-2025-05-13/.

Rijksdienst voor Ondernemend Nederland (RVO) (2022). *Technology Readiness Levels (TRL)*. https://www.rvo.nl/onderwerpen/trl. Laatst gecontroleerd op 16 april 2025.

Rijksoverheid (2022). *Offshore Wind Energy Roadmap 2030*. Accessed: 2025-05-13. https://www.rijksoverheid.nl/onderwerpen/windenergie-op-zee/aanpak-windenergie-op-zee.

Rystad Energy (2023). *Offshore wind developers, service groups under growing financial strain, report finds*. Accessed: 2025-05-13. https://www.offshore-mag.com/renewable-energy/article/14299335/rystad-energy-offshore-wind-developers-service-groups-under-growing-financial-strain-report-finds.

Schottler, J., Hölling, A., Peinke, J., and Hölling, M. (2016). "Design and implementation of a controllable model wind turbine for experimental studies". In: *Journal of Physics: Conference Series*. Vol. 753. 7. IOP Publishing, p. 072030. DOI: 10.1088/1742-6596/753/7/072030.

Schreiber, J. and Bottasso, C. A. (2022). "Experimental validation of wind farm wake steering strategies". In: *Renewable Energy* 195, pp. 319–331. DOI: 10.1016/j.renene.2022.05.111.

Selvam, K., Kanev, S., van Wingerden, J. W., van Engelen, T., and Verhaegen, M. (2009). "Feedback–feedforward individual pitch control for wind turbine load reduction". In: *International Journal of Robust and Nonlinear Control* 19.1, pp. 72–91. DOI: 10.1002/rnc.1324.

Siemens Gamesa (2019). *Siemens Gamesa Now Able to Actively Dictate Wind Flow at Offshore Wind Locations*. https://www.siemensgamesa.com/en-int/newsroom/2019/11/191126-siemens-gamesa-wake-adapt-en.

Simley, E. and Pao, L. Y. (2016). "Evaluation of a wind speed estimator for effective hub-height and shear components". In: *Wind Energy* 19.1, pp. 167–184. DOI: 10.1002/we.1817.

Skogestad, S. and Postlethwaite, I. (2005). *Multivariable Feedback Control: Analysis and Design*. 2nd. Hoboken, NJ, USA: Wiley-Interscience, p. 592. ISBN: 978-0470011683.

Snel, H. and Schepers, J. G. (1995). *Joint Investigation of Dynamic Inflow Effects and Implementation of an Engineering Method*. Technical Report ECN-C-94-107. Petten, Netherlands: Netherlands Energy Research Foundation (ECN), p. 326. https://publications.ecn.nl/E/1995/ECN-C--94-107.

Sørensen, J. N. and Shen, W. Z. (2002). "Numerical Modeling of Wind Turbine Wakes". In: *Journal of Fluids Engineering* 124.2, pp. 393–399. DOI: 10.1115/1.1471361.

Staff, R. (2024). “Wind turbine makers halt race for size to focus on cost, delivery”. In: *Reuters*. Accessed: 2025-05-16. https://www.reuters.com/business/energy/wind-turbine-makers-halt-race-size-focus-cost-delivery-2024-05-17/.

Stammler, M., Reuter, A., and Poll, G. (2018). “Cycle counting of roller bearing oscillations – case study of wind turbine individual pitching system”. In: *Renewable Energy Focus* 25, pp. 40–47. DOI: 10.1016/j.ref.2018.02.004.

Stanley, A. P. J., Bay, C. J., and Fleming, P. A. (2023). “Enabling control co-design of the next generation of wind power plants”. In: *Wind Energy Science* 8.8, pp. 1341–1350. DOI: 10.5194/wes-8-1341-2023.

Stevens, R. J. A. M., Gayme, D. F., and Meneveau, C. (2015). “Coupled wake boundary layer model of wind-farms”. In: *Journal of Renewable and Sustainable Energy* 7.2, p. 023115. DOI: 10.1063/1.4915287. eprint: https://pubs.aip.org/aip/jrse/article-pdf/doi/10.1063/1.4915287/15791249/023115_1_online.pdf.

Stevens, R. J. and Meneveau, C. (2017). “Flow structure and turbulence in wind farms”. In: *Annual Review of Fluid Mechanics* 49, pp. 311–339. DOI: 10.1146/annurev-fluid-010816-060206.

Stiesdal, H. (2020). *Personal history and overview of modern wind turbine development*. Accessed: 2025-05-13. https://www.windpower.org/download/647/stiesdal_history.pdf.

SURF (2024). *Snellius hardware and file systems*. [Online; accessed 30-August-2024]. https://servicedesk.surf.nl/wiki/display/WIKI/Snellius+hardware.

Taschner, E., Becker, M., Verzijlbergh, R., and Van Wingerden, J. (2024). “Comparison of helix and wake steering control for varying turbine spacing and wind direction”. In: *Journal of Physics: Conference Series* 2767.3, p. 032023. DOI: 10.1088/1742-6596/2767/3/032023.

Taschner, E., van Vondelen, A. A. W., Verzijlbergh, R., and van Wingerden, J. W. (2023). “On the performance of the helix wind farm control approach in the conventionally neutral atmospheric boundary layer”. In: vol. 2505. 1. IOP Publishing, p. 012006. DOI: 10.1088/1742-6596/2505/1/012006.

Taylor, P. K. and Yelland, M. J. (2001). “The Dependence of Sea Surface Roughness on the Height and Steepness of the Waves”. In: *Journal of Physical Oceanography* 31.2, pp. 572–590. DOI: 10.1175/1520-0485(2001)031<0572:TDOSSR>2.0.CO;2.

Thomsen, K. and Sørensen, P. (1999). “Fatigue loads for wind turbines operating in wakes”. In: *Journal of Wind Engineering and Industrial Aerodynamics* 80.1-2, pp. 121–136.

UNFCCC (2015). *The Paris Agreement*. Accessed: 2025-05-13. https://unfccc.int/process-and-meetings/the-paris-agreement.

Van Solingen, E. and van Wingerden, J. W. (2015). “Linear individual pitch control design for two-bladed wind turbines”. In: *Wind Energy* 18.4, pp. 677–697. DOI: 10.1002/we.1720.

Van Vondelen, A. A. W., Coquelet, M., Navalkar, S. T., and van Wingerden, J.-W. (2025). “Synchronized Helix wake mixing control”. In: *Wind Energy Science* 10.10, pp. 2411–2433. DOI: 10.5194/wes-10-2411-2025.

Van Vondelen, A. A. W., Navalkar, S. T., Iliopoulos, A., van der Hoek, D. C., and van Wingerden, J. W. (2022). "Damping identification of offshore wind turbines using operational modal analysis: a review". In: *Wind Energy Science* 7.1, pp. 161–184. DOI: 10.5194/wes-7-161-2022.

Van Vondelen, A. A. W., Pamososuryo, A. K., Navalkar, S. T., and van Wingerden, J. W. (2024). "On the Optimal Azimuth Offset for Individual Pitch Control in Aeroelastic Code Coupled with a High-Fidelity Flow Solver". In: *2024 European Control Conference (ECC)*, pp. 2411–2416. DOI: 10.23919/ECC64448.2024.10590980.

Van Vondelen, A. A. W., van der Hoek, D. C., Navalkar, S. T., and van Wingerden, J. W. (2024). "Synchronized Dynamic Induction Control: An Experimental Investigation". In: *Journal of Physics: Conference Series*. Vol. 2767. 3. IOP Publishing, p. 032027. DOI: 10.1088/1742-6596/2767/3/032027.

Van Vondelen, A. A. W., Navalkar, S. T., Kerssemakers, D. R. H., and Van Wingerden, J. W. (2023). "Enhanced wake mixing in wind farms using the Helix approach: A loads sensitivity study". In: *2023 American Control Conference (ACC)*, pp. 831–836. DOI: 10.23919/ACC55779.2023.10155965.

Van Vondelen, A. A. W., Ottenheym, J., Kalogera, M., and van Wingerden, J. W. (Jan. 9, 2025). "Enhanced Wind Turbine Wake Mixing". Patent NL2035238B1. Issued: January 9, 2025; Filed: June 30, 2023. https://patents.google.com/patent/NL2035238B1.

Van Vondelen, A. A. W., Ottenheym, J., Pamososuryo, A. K., Navalkar, S. T., and van Wingerden, J. W. (2023). "Phase Synchronization for Helix Enhanced Wake Mixing in Downstream Wind Turbines". In: *IFAC-PapersOnLine* 56.2. 22nd IFAC World Congress, pp. 8426–8431. DOI: 10.1016/j.ifacol.2023.10.1039.

Van Vondelen, A. A. W., Pamososuryo, A. K., Navalkar, S. T., and van Wingerden, J. W. (2025). "Control of Periodically Waked Wind Turbines". In: *IEEE Transactions on Control Systems Technology* 33.2, pp. 700–713. DOI: 10.1109/TCST.2024.3508577.

Van Wingerden, J. W., Fleming, P. A., Göçmen, T., Eguinoa, I., Doekemeijer, B. M., Dykes, K., Lawson, M., Simley, E., King, J., Astrain, D., and et al. (2020). "Expert Elicitation on Wind Farm Control". In: *Journal of Physics: Conference Series* 1618.2, p. 022025. DOI: 10.1088/1742-6596/1618/2/022025.

Van der Veen, G., van Wingerden, J. W., Bergamasco, M., Lovera, M., and Verhaegen, M. (2013). "Closed-loop subspace identification methods: an overview". In: *IET Control Theory & Applications* 7.10, pp. 1339–1358.

Van der Hoek, D. C., Frederik, J. A., Huang, M., Scarano, F., Simao Ferreira, C., and van Wingerden, J. W. (2022). "Experimental analysis of the effect of dynamic induction control on a wind turbine wake". In: *Wind Energy Science* 7.3, pp. 1305–1320. DOI: 10.5194/wes-7-1305-2022.

Van der Hoek, D. C., Kanev, S., Allin, J., Bieniek, D., and Mittelmeier, N. (2019). "Effects of axial induction control on wind farm energy production—A field test". In: *Renewable Energy* 140, pp. 994–1003. DOI: 10.1016/j.renene.2019.03.117.

Van der Hoek, D. C., Van den Abbeele, B. H. L., Ferreira, C. S., and van Wingerden, J. W. (2024). "Maximizing Wind Farm Power Output with the Helix Approach: Experimental Validation and Wake Analysis Using Tomographic PIV". In: *Wind Energy* 27.7. DOI: 10.1002/we.2896.

van Vondelen, A. A. W., van der Hoek, D. C., Navalkar, S. T., and van Wingerden, J. W. (2025). "Experimental validation of synchronized Helix wake mixing control". In: *Renewable Energy*, p. 124768. ISSN: 0960-1481. DOI: https://doi.org/10.1016/j.renene.2025.124768.

Veers, P., Dykes, K., Lantz, E., Barth, S., Bottasso, C. L., Carlson, O., Clifton, A., Green, J., Green, P., Holttinen, H., and et al. (2019). "Grand challenges in the science of wind energy". In: *Science* 366.6464, eaau2027. DOI: 10.1126/science.aau2027.

Verhaegen, M. and Verdult, V. (2007). *Filtering and System Identification: A Least Squares Approach*. 1st. Cambridge, UK: Cambridge University Press, p. 422. ISBN: 978-0521875127.

Wagenaar, J. W., Machielse, L. A. H., and Schepers, J. G. (2012). "Controlling Wind in ECN's Scaled Wind Farm". In: *Proceedings of Europe Premier Wind Energy Event*. ECN Conference. Copenhagen, Denmark, pp. 685–694. https://publications.ecn.nl/E/2012/ECN-M--12-007.

WindpowerNL (2023). *SUDOCO project works on wind farm control room of the future*. https://windpowernl.com/2023/10/17/sudoco-project-works-on-wind-farm-control-room-of-the-future/. Accessed: 2025-06-16.

Wurps, H., Steinfeld, G., and Heinz, S. (2020). "Grid-Resolution Requirements for Large-Eddy Simulations of the Atmospheric Boundary Layer". In: *Boundary-Layer Meteorology* 175.2, pp. 179–201. DOI: 10.1007/s10546-020-00504-1.

Yang, K., Kwak, G., Cho, K., and Huh, J. (2019). "Wind farm layout optimization for wake effect uniformity". In: *Energy* 183, pp. 983–995. DOI: 10.1016/j.energy.2019.07.019.

Zilitinkevich, S., Esau, I., and Baklanov, A. (2007). "Further comments on the equilibrium height of neutral and stable planetary boundary layers". In: *Quarterly Journal of the Royal Meteorological Society* 133.622, pp. 265–271. DOI: 10.1002/qj.27.

CURRICULUM VITÆ

Aemilius Adrianus Wilhelmus VAN VONDELEN

1997	Born in Zeist on the 15th of January, the Netherlands.
2008–2014	Tweetalig Gymnasium Christelijk Lyceum Zeist, the Netherlands
2014–2017	Bachelor of Science in Werktuigbouwkunde Technische Universiteit Delft, the Netherlands
2018–2021	Master of Science in Systems & Control Technische Universiteit Delft, the Netherlands *Thesis:* Damping Identification of Operational Offshore Wind Turbines *Supervisors:* prof. dr. ir. J.W. van Wingerden, dr. ir. S.T. Navalkar, dr. ir. A. Iliopoulos, dr. ir. D.C. van der Hoek
2021 - 2025	Doctor of Philosophy in Systems & Control Technische Universiteit Delft, the Netherlands *Thesis:* In Rhythm with the Wind: Synchronized Wake Mixing in Wind Farms *Promotor:* prof. dr. ir. J.W. van Wingerden *Supervisor:* dr. ir. S.T. Navalkar

LIST OF PUBLICATIONS

JOURNAL ARTICLES

7. **van Vondelen, A. A. W.**, van der Hoek, D. C., Navalkar, S. T., and van Wingerden, J. W. (2026). *Experimental validation of synchronized Helix wake mixing control.* Renewable Energy, 257, pp. 124768.

6. **van Vondelen, A. A. W.**, Coquelet, M., Navalkar, S. T., and van Wingerden, J. W. (2025). *Synchronized Helix Wake Mixing Control.* Wind Energy Science, 10(10), pp. 2411–2433.

5. Gutierrez Santiago, U., **van Vondelen, A. A. W.**, Fernández Sisón, A., Polinder, H., and van Wingerden, J. W. (2025). *Identification of operational deflection shapes of a wind turbine gearbox using fiber-optic strain sensors on a serial production end-of-line test bench.* Wind Energy Science, 10(1), pp. 207–225.

4. **van Vondelen, A. A. W.**, Pamososuryo, A. K., Navalkar, S. T., and van Wingerden, J. W. (2025). *Control of periodically waked wind turbines.* IEEE Transactions on Control Systems Technology, 33(2), pp. 700–713.

3. Coquelet, M., Lejeune, M., Bricteux, L., **van Vondelen, A. A. W.**, van Wingerden, J. W., and Chatelain, P. (2024). *On the robustness of a blade-load-based wind speed estimator to dynamic pitch control strategies.* Wind Energy Science, 9(10), pp. 1923–1940.

2. **van Vondelen, A. A. W.**, Iliopoulos, A., Navalkar, S. T., van der Hoek, D. C., and van Wingerden, J. W. (2023). *Modal analysis of an operational offshore wind turbine using enhanced Kalman filter-based subspace identification.* Wind Energy, 26(9), pp. 923–945.

1. **van Vondelen, A. A. W.**, Navalkar, S. T., Iliopoulos, A., van der Hoek, D. C., and van Wingerden, J. W. (2022). *Damping identification of offshore wind turbines using operational modal analysis: a review.* Wind Energy Science, 7(1), pp. 161–184.

PATENT

1. **van Vondelen, A. A. W.**, Ottenheym, J., Kalogera, M., and van Wingerden, J. W. (2025). *Enhanced wind turbine wake mixing.* Dutch Patent NL2035238B1, issued January 9, 2025.

Included in this dissertation.

CONFERENCE PAPERS

All papers were presented orally by the first author.

5. **van Vondelen, A. A. W.**, van der Hoek, D. C., Navalkar, S. T., and van Wingerden, J. W. (2024). *Synchronized dynamic induction control: an experimental investigation*. Journal of Physics: Conference Series, 2767(3), p. 032027. Proceedings of Torque 2024, Florence, Italy.

4. **van Vondelen, A. A. W.**, Pamososuryo, A. K., Navalkar, S. T., and van Wingerden, J. W. (2024). *On the optimal azimuth offset for individual pitch control in aeroelastic code coupled with a high-fidelity flow solver*. Proceedings of the European Control Conference (ECC), Stockholm, Sweden, pp. 2411–2416.

3. Taschner, E., **van Vondelen, A. A. W.**, Verzijlbergh, R., and van Wingerden, J. W. (2023). *On the performance of the helix wind farm control approach in the conventionally neutral atmospheric boundary layer*. Journal of Physics: Conference Series, 2505(1), p. 012006. Proceedings of Wake Conference 2023, Visby, Sweden.

2. **van Vondelen, A. A. W.**, Ottenheym, J., Pamososuryo, A. K., Navalkar, S. T., and van Wingerden, J. W. (2023). *Phase synchronization for Helix enhanced wake mixing in downstream wind turbines*. IFAC-PapersOnLine, 56(2), pp. 8426–8431. Proceedings of the IFAC World Congress, Yokohama, Japan.

1. **van Vondelen, A. A. W.**, Navalkar, S. T., Kerssemakers, D. R. H., and van Wingerden, J. W. (2023). *Enhanced wake mixing in wind farms using the Helix approach: a loads sensitivity study*. Proceedings of the American Control Conference (ACC), San Diego, CA, USA, pp. 831–836.

PRESENTATIONS

4. **van Vondelen, A. A. W.** (2025). *Synchronized Helix Wake Mixing*. Oral presentation at Wind Energy Science Conference (WESC) 2025, Nantes, France. Co-authors: M. Coquelet, S. T. Navalkar, J. W. van Wingerden.

3. **van Vondelen, A. A. W.** (2025). *Optimizing Wind Farm Efficiency through Synchronized Helix Wake Mixing Using Wind Speed Estimation*. Oral presentation at WindEurope Annual Event 2025, Copenhagen, Denmark. Co-authors: M. Coquelet, S. T. Navalkar, J. W. van Wingerden.

2. **van Vondelen, A. A. W.** (2024). *Periodic Wake Estimation for Synchronized Wake Mixing Control*. Poster presentation at NAWEA/WindTech 2024 Conference, New Brunswick, NJ, USA. Co-authors: M. Coquelet, S. T. Navalkar, J. W. van Wingerden.

1. **van Vondelen, A. A. W.** (2023). *Combined Helix and Individual Pitch Control for Wake Mixing and Load Reduction in Wind Farms*. Oral presentation at Wind Energy Science Conference (WESC) 2023, Glasgow, UK. Co-authors: S. T. Navalkar, J. W. van Wingerden.

Included in this dissertation.

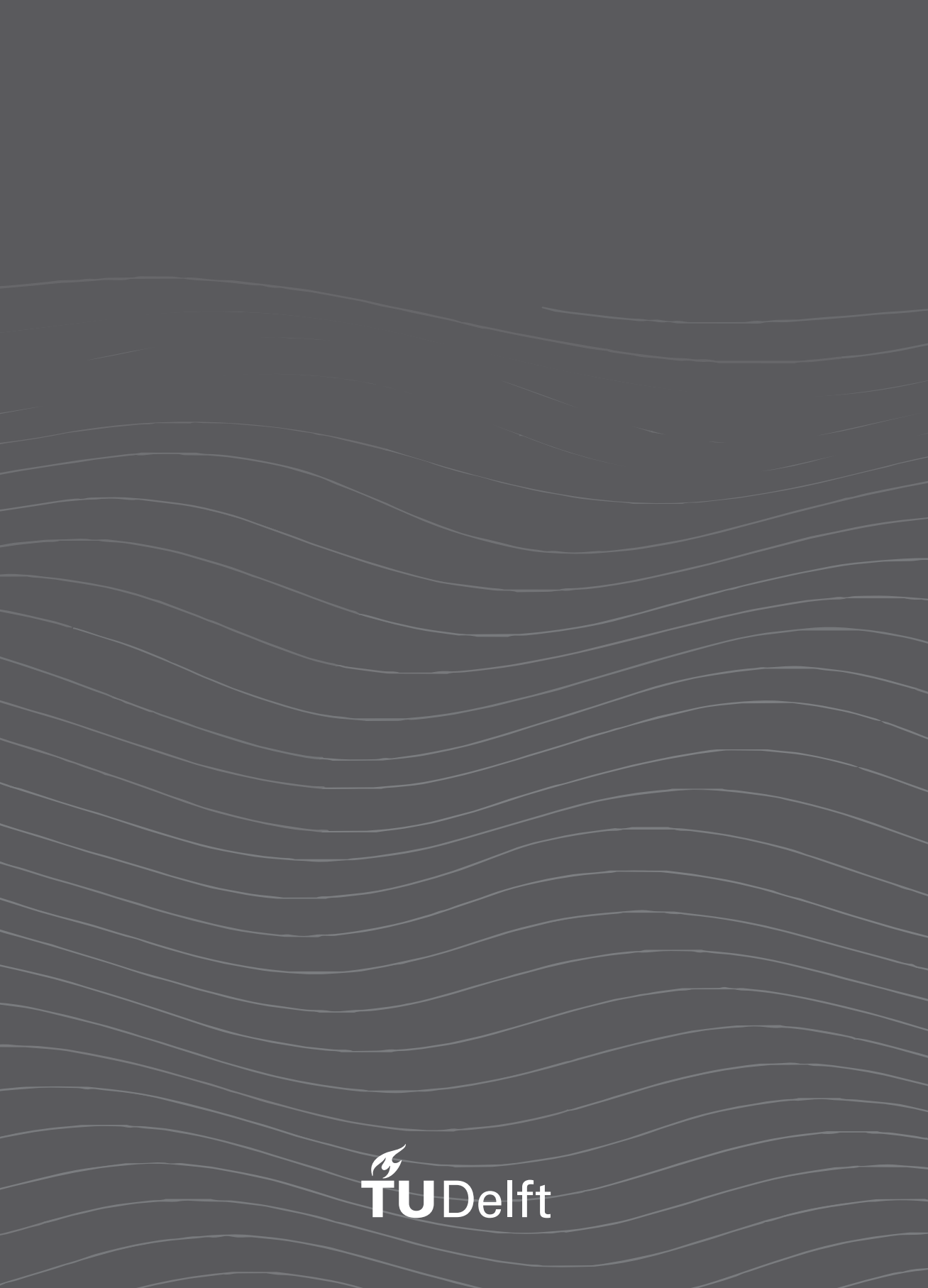
TUDelft